Annu. Rev. Mater. Res. 2005. 35:239–314
doi: 10.1146/annurev.matsci.35.102303.091623

First published online as a Review in Advance on March 17, 2005

ANALYTICAL TRANSMISSION ELECTRON MICROSCOPY

Wilfried Sigle
Max-Planck-Institut für Metallforschung, D-70569 Stuttgart; email: sigle@mf.mpg.de

Key Words electron spectroscopy, EELS, EDXS, energy-filtered TEM, electron scattering

■ **Abstract** Chemical analysis at high spatial resolution is the domain of analytical transmission electron microscopy. Owing to rapid instrumental developments during the past decade, electron energy-loss spectroscopy offers now a spatial resolution close to 0.1 nm and an energy resolution close to 0.1 eV. This development has been accompanied by the introduction of numerous new techniques and methods for data acquisition and analysis, which are outlined in the present article. Recent results for a wide range of material systems are addressed. These comprise first-principles calculations, which have contributed to enormous progress in the calculation of near-edge fine structures, and fingerprinting methods, which are still important for the interpretation of experimental data.

INTRODUCTION

In ancient times the development of new materials took place on a time-scale of thousands of years. This long time-scale was not only related to the lack of appropriate processing techniques (e.g., high temperatures) but also to the ignorance of the nature of materials. The discovery of the light microscope in the late sixteenth century by the Dutch optician Zacharias Janssen offered the possibility to study the outer shape of small pieces of materials. However, it was not before the late nineteenth century that the microscope was used to study the polycrystalline microstructure of metals (1). Although the majority of the elements of the periodic table were already known at this time, the internal structure of materials was unknown. Suitable experimental techniques were invented some decades later [X-ray diffraction (2) and electron diffraction (3)] that made structural analysis of the interior of materials possible. Shortly after, the electron microscope was developed (4), which soon offered a spatial resolution superior to optical microscopes. Another 15 years passed until it was possible to prepare sections from materials thin enough for the transmission of fast electrons (5, 6). This was the advent of spatially resolved characterization of materials. The ongoing technical improvement of transmission electron microscopes (TEMs) has nowadays reached the level of atomic resolution.

Electrons can not be used only for imaging. Along their path through the specimen, many electrons undergo inelastic scattering processes which result in an energy loss. Relaxation processes can lead to the emission of characteristic X-ray quanta, Auger electrons, or light. It is these inelastic processes that make chemical analysis of materials possible in the TEM. These electron spectroscopic methods are the main scope of this article. However, numerous other techniques make use of the *Z*-dependence of elastic scattering (*Z* contrast), of phase shifts of electrons passing the specimen (electron holography), of chemically sensitive Bragg reflections (high-resolution TEM), or of the intensity of atom columns in high-resolution TEM micrographs. All these methods therefore contain chemical information, although less direct than found in spectroscopic measurements, but in some cases with a spatial resolution that is difficult to achieve by spectroscopy. Therefore, the potentials of these methods are also shortly addressed.

THE ELECTRON MICROSCOPE

The Electron Source

Apart from a long lifetime, the main requirements of the electron source are high brightness (electron current density per solid angle) and small spread of the kinetic electron energy. This requires materials with a small work function. Modern TEMs are equipped with either LaB_6 or field emission guns (FEGs) (Table 1). LaB_6 filaments offer a high current, but the brightness is by three orders of magnitude lower than that of FEGs. Whereas the high current is well suited for energy-filtering TEM (EFTEM), the low brightness leads to impractically small currents if a small electron probe of nanometer size is formed. This is the domain of field-emission sources, which consist of pointed tungsten wires exposed to a high electric field. In the case of heated FEGs (Schottky emitters), the tip of the wire is coated with ZrO_2. Cold FEGs have the main advantage of a small energy spread and a very long lifetime, but the total current is small and the long-term current stability is poor.

TABLE 1 Parameters of different electron emitters

		Field emission source (W)	
	LaB_6	**Schottky type**	**Cold**
Brightness (Acm^{-2} sr^{-1}) (at 100 kV)	10^6	10^8–10^9	10^7–10^9
Energy spread (eV)	0.7–0.9	0.7–0.9	0.3–0.5
Total current (nA)	500	300	3
Current density (Acm^{-2})	10	10^5	10^4–10^5

In order to improve the energy spread of the source, monochromators have recently been introduced. There are two basic approaches: the Wien filter with crossed electric and magnetic fields and the electrostatic Omega filter. Both types improve the energy width to about 0.2 eV at a yet acceptable beam current of several 100 pA. The single Wien filter limits the probe size to about 2 nm, whereas there is no such limitation in the case of the Omega filter. This spatial aberration of the Wien filter can be improved by using double Wien filters (7).

Electron Lenses

Owing to their electric charge, electrons can be deflected by electric or magnetic fields. Modern electron microscopes are equipped with round magnetic lenses. The magnetic flux (typically of the order of 1 T) is concentrated in a narrow circular gap between two pole pieces. Because the focal length of such lenses is of the order of millimeters, the specimen is immersed in the magnetic field. This is done by using a long specimen rod that is inserted either into the pole piece gap (side-entry lens) or from the top of the lens (top-entry lens). The former offers more flexibility for in situ experiments (heating, cooling, straining, etc.), the latter is less influenced by external influences such as variation of room temperature and air pressure, or noise.

Round magnetic lenses suffer from severe aberrations, which are the resolution-limiting factor in TEMs as long as other instabilities are small (e.g., those of lens currents, high voltage, external vibrations, or AC electric and magnetic fields). Because the strongest aberration is the spherical aberration (aberration coefficient C_s), a longstanding dream of TEM was the implementation of C_s correctors. Owing to the need for high mechanical precision and lens current stability, as well as for computer control, this was achieved in only the past decade (8, 9), mostly on the basis of suggestions by Rose (10, 11). In scanning TEM, the resolution-limiting factor is the size of the focused electron probe. With use of C_s correctors, probes below 0.1 nm can be achieved (12–14), and values below 0.1 nm were recently demonstrated (15). An important advantage of C_s correctors is that larger acceptance angles can be used that increase the probe current considerably. In the TEM, C_s correctors allow for a much more straightforward interpretation of high-resolution images. Recent examples (16) demonstrate how the application of a negative C_s value simplifies the detection of light atoms.

Illumination Modes

In conventional TEMs the specimen is illuminated by an almost parallel electron beam. The objective lens is used to form a magnified (intermediate) image of the illuminated area, which is further magnified by postspecimen lenses onto the image detector. Modern FEG-TEMs are often equipped with scanning coils that allow the microscopes to be used in a second imaging mode, the scanning mode. In this case the electron beam is focused on the specimen by the condenser lenses and the objective-lens prefield. The small probe is scanned across the area of interest in the

specimen plane. The image is obtained either (*a*) from electrons that have not been scattered or are only under small angles or (*b*) from electrons that have undergone large-angle scattering events. The first mode gives a bright-field image, the second one an annular-dark-field image. If electrons are detected that were scattered under angles above about 70–100 mrad, the second mode is called high-angle annular-dark-field (HAADF) mode. Microscopes operating only in the scanning mode are called scanning TEMs (STEMs). Some STEMs (e.g., the VG HB501) have no lenses behind the specimen, which makes their design rather intuitive (Figure 1).

Important quantities for spectroscopy are the convergence angle, β, and the collection angle, α, because they enter into the formulae for the partial inelastic scattering cross-sections (see below). The convergence angle is defined as the half angle of the cone illuminating the specimen. The collection angle is the maximal scattering angle that is accepted by the spectrometer. In a dedicated STEM, β is determined by the size of the objective aperture, whereas α is determined by the size of the collection aperture. In TEMs and in STEMs with postspecimen lenses the situation is more complicated because the postspecimen lenses have the

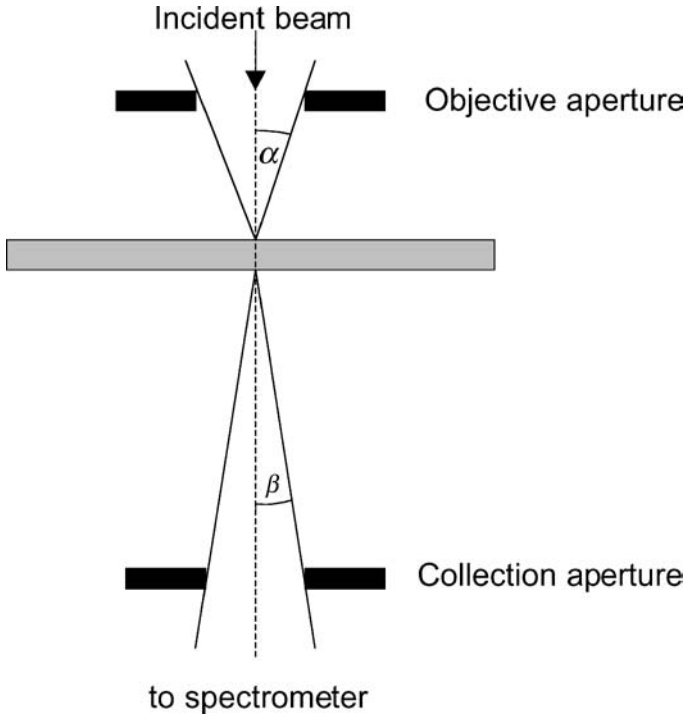

Figure 1 Electron beam path in a dedicated STEM. The objective aperture determines the angular range of illumination of the specimen, whereas the collection aperture is used to limit the angle of the scattered electrons entering the spectrometer.

TABLE 2 How apertures determine the collection and convergence angles in EELS in the case of a dedicated STEM and a TEM

	STEM (with no lenses after the specimen)	TEM	
		Image mode	Diffraction mode
Convergence angle α	OA	Condenser aperture	Condenser aperture
Collection angle β	CA	OA	The smaller of SEA and OA (for SEA: β depends on camera length)
Selected area	Probe size	Size of image on SEA, but affected by chromatic aberration	SAD aperture or probe size if beam is focused

OA, objective aperture; CA, collection aperture; SEA, spectrometer entrance aperture; SAD, selected area aperture.

property of changing beam angles. In TEMs, one has further to distinguish between image mode (image on fluorescent screen) and diffraction mode (diffraction pattern on fluorescent screen). Table 2 shows how the apertures in the STEM and TEM determine α and β. Note that for $\alpha > \beta$, the geometrically given collection angle should be replaced by an effective one (17) (see below).

Electron Spectrometers

Electron spectroscopy in the STEM was pioneered by Crewe et al. (18, 19). The basic electron spectrometer type is the prism spectrometer (Figure 2). Electrons are deflected by about 90° in a perpendicular static magnetic field. According to the Lorentz force, the deflection angle depends on the electron velocity. Using quadrupole lenses the electrons are focused in the energy-dispersive plane of the spectrometer where a position-sensitive detector is located. This detector can be an array of photodiodes or a charge-couple device (CCD), in both cases combined with a suitable combination of a scintillator and a light-guide. The CCD has the advantage of a better (electron-to-counts) conversion efficiency, better spatial resolution (narrower point-spread function), and often a higher dynamic range (16 bit). High conversion efficiency is important if the signal of interest is low. The spatial resolution is directly linked with the energy resolution. A high dynamic range is essential for the detection of the low-energy part of the energy-loss spectrum.

Energy Filters

The purpose of the energy filter is to form images from electrons that have suffered a specific energy loss [energy-filtered TEM (EFTEM) or electron spectroscopic imaging (ESI)] (20). An energy filter consists of an electron spectrometer with a mechanical slit in the energy-dispersive plane that is used for

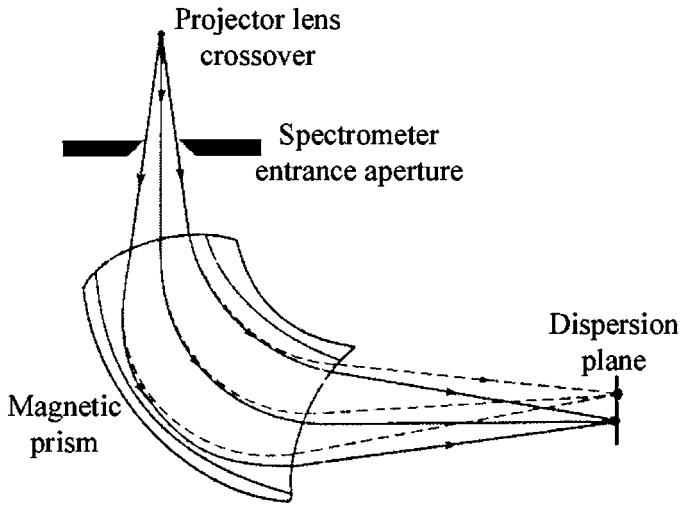

Figure 2 Design of a magnetic prism electron spectrometer. Electrons of various kinetic energies (depending on the energy losses they suffered within the specimen) enter the spectrometer. Because the magnetic force acting on the electrons depends on their velocity, an energy-loss spectrum is formed in the energy-dispersive plane. The spectrum is recorded by a CCD array located in this plane.

the selection of the energy loss of interest (Figure 3). Behind the slit either an energy-filtered image (or diffraction pattern) or an image of the energy-dispersive plane [the electron energy-loss (EEL) spectrum] is formed by additional electron lenses. These lenses can be considered as a second projector lens system of the microscope.

There are basically two types of energy filters: the in-column filter and the post-column filter. The in-column filter is a symmetric filter incorporated in the microscope column below the usual projector lenses (Figure 3). Owing to the symmetry, a number of aberrations vanish for this type of filter. The pre- and post-filter electron trajectories are parallel, which makes the in-column filter design an obvious choice. However, a drawback is that an in-column filter cannot be attached to an existing TEM column. This is possible with the postcolumn filter (21) which has a 90° design and thus lacks the symmetry of the in-column filter. The corresponding higher number of aberrations is corrected by additional multipole lenses behind the filter.

An energy filter can be characterized by its transmissivity, which is a measure of the volume in phase-space that can be transferred (22, 23). A filter with a high transmissivity accepts electrons with large angles with respect to the optical axis, and it gives a large field of view even if narrow energy-selecting slits are used. Unfortunately no round-robin tests have been performed yet in order to compare the different filter designs.

Energy-Dispersive X-Ray Detector

For the detection of characteristic X-rays, energy-dispersive semiconductor detectors are used. Although they have a rather poor energy resolution, their detection efficiency is far superior to wavelength-dispersive detectors, which is an important requirement in the TEM owing to the low count rate. At present, mainly Li-drifted silicon detectors are used. They have an energy resolution of about 140 eV at 5.9 keV. Using digital pulse-processors, count rates of 10,000 counts $\cdot s^{-1}$ can be handled. Despite the poor energy resolution, energy-dispersive X-ray spectroscopy (EDXS) is often used because quantification is more straightforward than in electron energy-loss spectroscopy (EELS) and the detection of high-Z elements is often easier. However, the detection of low-energy quanta is considerably affected by absorption effects in the specimen and in the detector window. Therefore, elements of low atomic number should be more easily detected by EELS. A further disadvantage of EDXS spectrometers is the small collection solid angle (at most a few tenths of a steradian). This is limited by the size of the detector crystal, as well as by the specimen–detector distance.

Recently, microcalorimeters have been employed for the energy-dispersive detection of X-rays. They measure the heat generated by the X-rays in a superconducting material (24, 25). The energy resolution is below 10 eV and thus comparable to wavelength-dispersive spectrometers. However, the maximal count rate is lower by a factor of 10 compared with that found with conventional EDXS detectors. Furthermore, such detectors are at present extremely expensive. Figure 4 shows

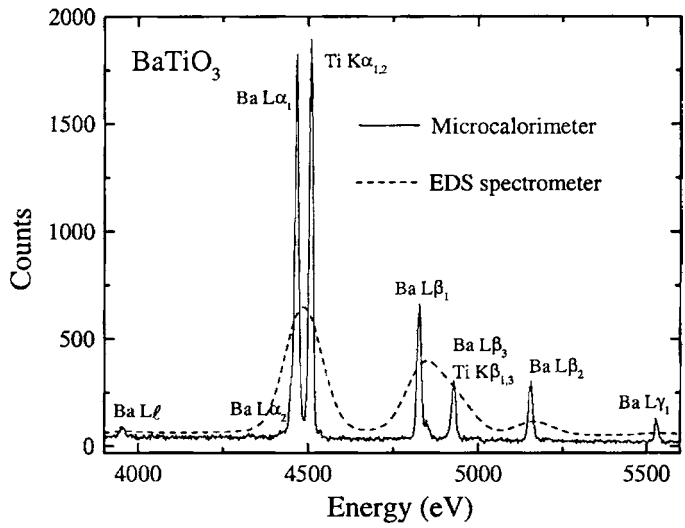

Figure 4 Comparison of EDXS spectra of $BaTiO_3$ obtained by a conventional semiconductor detector (*broken line*) and a microcalorimeter detector (*solid line*). Reprinted from Wollmann et al. (24).

the richness of information obtained with such detectors in comparison to that obtained with semiconductor detectors (dashed line) (24).

Whereas calorimeters have the advantage of high-energy resolution, silicon drift detectors offer a factor of 10 increase of count rate compared with that of Si(Li) detectors (26). This makes very fast EDXS mapping possible if the count rate is high enough. Furthermore, such detectors can be made with larger areas, which increases the collection solid angles, probably by a factor of 2 or 3. The space required for these large detectors becomes available in C_s corrected microscopes with large pole-piece gaps. For reviews on EDXS analysis the reader is referred to (27, 28).

ELECTRON-SPECIMEN INTERACTION

The interaction of electrons with matter is much stronger than that of X-rays with matter. This is a natural consequence of the electrical charge, and it is this strong interaction that makes the study of small volumes of material possible and thus is the basis for high spatial resolution. On the other hand, multiple scattering effects often complicate quantitative analysis.

Electron Scattering

Although the total potential of an atom (generated by the charged nucleus and the electron cloud) is responsible for the scattering process, one can distinguish limiting cases (see Table 3) where the scattering center can be ascribed to a single nucleus or an electron, or to a multiple of both. Because of the same mass, electron–electron scattering leads to significant energy losses that makes this type of scattering the most significant for analytical TEM. Because the electron–nucleus interaction depends on the atomic number Z, it can also be used for chemical analysis. However, quantification is complicated in this case (see below).

TABLE 3 Interactions of electrons in a solid

	Interaction of electron with		**Interaction of electron with**		
	1 electron	**Many electrons**	**1 nucleus**	**Many nuclei**	
Type of scattering	Inelastic	Inelastic	(Quasi) elastic	Elastic	Inelastic
Scattering effect	Electron Compton effect, electron excitation	Plasmon excitation, Cerenkov effect	Rutherford scattering, phonon scattering	Bragg scattering	Bremsstrahlung

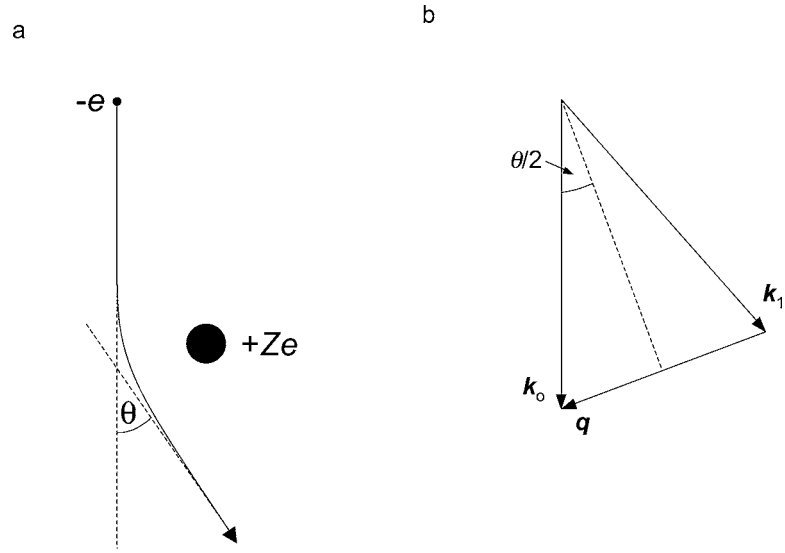

Figure 5 (*a*) Scattering of an electron at a nucleus. (*b*) Initial ($\boldsymbol{k}_0$) and final ($\boldsymbol{k}_1$) wave vector of an elastically scattered electron and momentum transfer $\boldsymbol{q}$.

ELASTIC SCATTERING Let us assume an electron with kinetic energy E and velocity v undergoing a scattering event with an atom of atomic number Z and atom mass A (see Figure 5). The potential of the atom nucleus is screened by the surrounding electrons. Therefore only approximate analytical expressions of the potential are available. In the simple case of a Wentzel potential, which uses an exponential decay of the potential with a decay length r_0 ($\approx a_0 Z^{-1/3}$), the differential scattering cross-section is given by

$$\frac{\mathrm{d}\sigma}{\mathrm{d}\Omega} \approx \frac{4\gamma^2 Z^2}{a_0^2 k_0^4} \frac{1}{\left(\theta^2 + \theta_0^2\right)^2}. \qquad 1.$$

Here, a_0 is the Bohr radius (0.0529 nm), $\gamma = (1 - v^2/c^2)^{-1/2}$, with c the speed of light, and θ the electron scattering angle. k_0 is the modulus of the wave vector of the incident electron. $\theta_0 = (k_0 r_0)^{-1}$ is the characteristic angle for elastic scattering.

In the limit of small impact parameter we obtain the expression for Rutherford scattering. In this case, the scattering angle is large and in the extreme case the electron is back scattered. The energy transfer to the atom can be of the order of 10s or 100s of eV, which may be sufficient for a displacement of the atom and thus to radiation damage (see below). This type of a scattering event can no more be considered elastic. It is often neglected in TEM because of the small scattering cross-section compared with that of other inelastic scattering events.

In crystalline materials elastic scattering can lead to the formation of strong Bragg reflections, described as originating from the constructive interference of spherical secondary electron waves emanating from the crystal atoms. An alternative approach is to solve the Schrödinger equation. The solution of the equation in a periodic potential of a crystal is characterized by Bloch functions, which are usually called Bloch waves in the case of fast incident electrons. Following the solution for an atom potential, the Bloch waves are denoted as s-, p-type etc., depending on their symmetry. Whenever lattice planes are close to the Bragg orientation certain Bloch waves are strongly excited, e.g., if $\boldsymbol{k}_0$ of the incident electron wave is parallel to a row of atoms (zone axis orientation), electrons are concentrated ("channelled") in the vicinity of this atom row of positive ions. This corresponds to an s-type Bloch wave. The strong excitation of certain Bloch waves is correlated with an inhomogeneous electron distribution within the unit cell of the crystal. Such conditions should be avoided for quantitative chemical analysis unless it is done intentionally as in the ALCHEMI method (29, 30). In the case of simultaneous *Z*-contrast imaging (see below) and EELS analysis along a zone axis, one should be aware of artifacts that may arise owing to the channelling effect.

INELASTIC SCATTERING A typical spectrum of energy losses suffered by an electron penetrating through a thin slice of a material is shown in Figure 6. The zero-loss peak includes all elastically scattered electrons, but also electrons with energy losses less than the energy resolution of the TEM (mostly phonon scattering). The energy-loss range up to about 100 eV is dominated by collective electron excitations (plasmons), but it also contains interband transitions from the valence to the conduction band (Figure 7). This regime includes the optical transitions and can therefore be used for the determination of optical properties (17). At higher energy

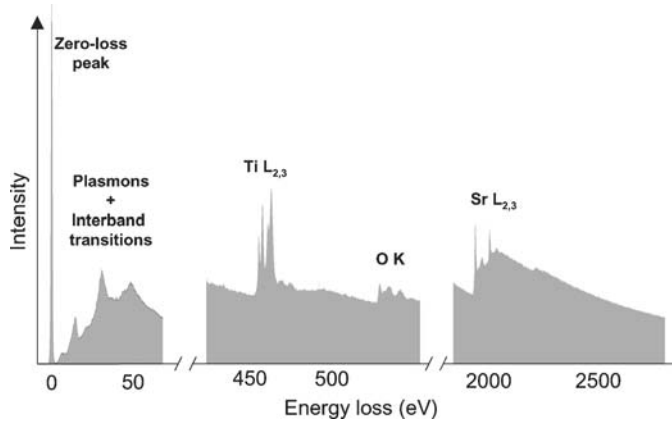

Figure 6 Electron energy-loss spectrum of $SrTiO_3$. The middle and right parts of the spectrum are strongly magnified compared with those in the low-loss spectrum.

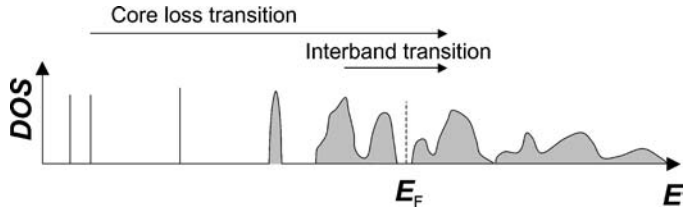

Figure 7 Electron transitions in a solid material. Core levels can be considered as atomic-like levels, whereas the levels are band-like near and above the Fermi level E_F.

losses excitations from core levels to unoccupied states above the Fermi level are found (Figure 7), which are superimposed on a background signal stemming from the low-loss events. These core-level excitations lead to edge-like features with an onset energy corresponding to the lowest unoccupied state. They are classified according to the initial state of the excited electron (Figure 8). Because the initial

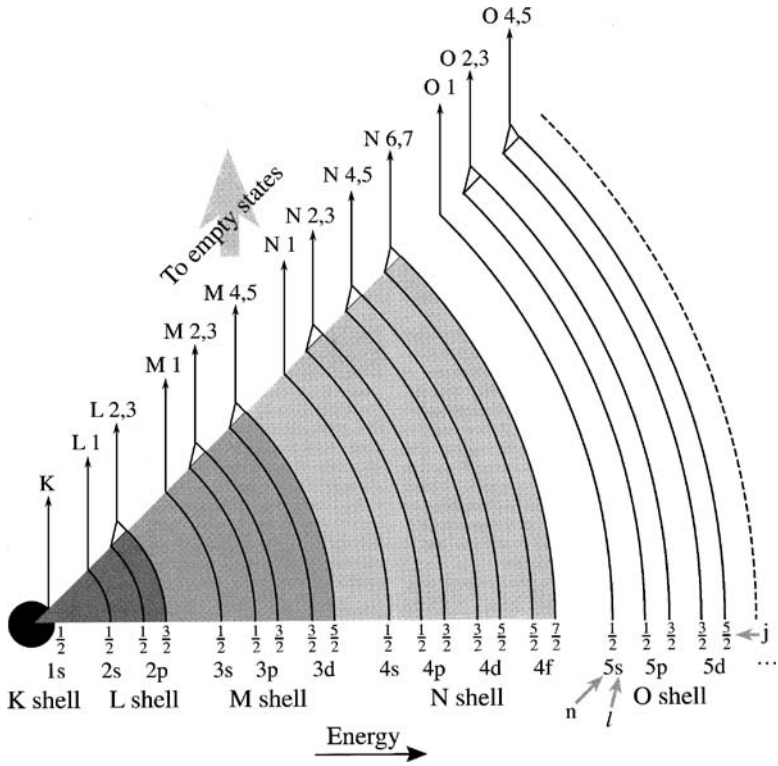

Figure 8 Classification of core transitions in EELS. Reprinted with permission from Williams & Carter (97).

states are hardly modified from atomic levels even in a solid, the shape of the absorption edge is mainly determined by the density of unoccupied states (see below) and thus includes information about the bonding state. Elemental concentrations can be extracted from the area underneath the absorption edge.

According to Lenz (31) the differential inelastic cross-section for electron–electron scattering can be written as (17)

$$\frac{\mathrm{d}\sigma_i}{\mathrm{d}\Omega} \approx \frac{4\gamma^2 Z}{a_0^2 q^4} \left\{ 1 - \frac{1}{\left[1 + (qr_0)^2\right]^2} \right\}, \qquad 2.$$

with the scattering vector $q^2 = k_0^2(\theta^2 + \bar{\theta}_E^2)$ (Figure 5). $\bar{\theta}_E = \bar{E}/(\gamma m_0 v^2)$ is a scattering angle corresponding to a mean energy loss $\bar{E}$ and is usually denoted as the characteristic angle for inelastic scattering. Because the majority of energy losses is well below 100 eV, the characteristic angle is of the order of a few tenths of a milliradian, which is much smaller than typical Bragg angles. This means that the Lorentzian distribution of inelastic scattering is much more forward-directed than elastic scattering. Note, however, that for high-energy losses the characteristic scattering angle can be quite appreciable (e.g., 2.5 mrad at $\Delta E = 1000$ eV for 200 keV electrons). In the limit of "ballistic electron–electron collisions" (or electron Compton scattering (32, 33), a broad energy-loss peak occurs at high-energy losses (Figure 9). Because such electrons are deflected under relatively large

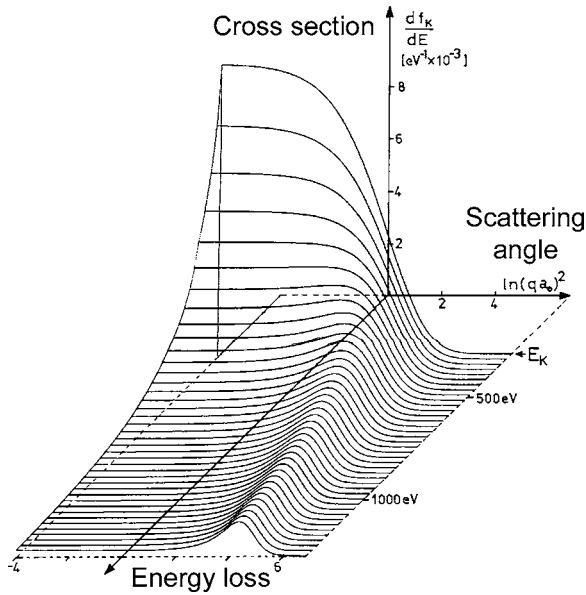

Figure 9 Electron scattering intensity as a function of energy loss and scattering angle. At large scattering angles, the Bethe ridge occurs. Reprinted with permission from Egerton (17).

angles (known as the Bethe ridge) (17), they are often not observed when low-angle scattering is studied.

As can be seen from Equations 1 and 2, inelastic electron–electron scattering shows a weaker dependence on the atomic number than does elastic scattering. Therefore, the ratio of inelastic to elastic scattering is particularly strong for light atoms and vice versa. In addition to electron–electron scattering, electron–phonon interaction is an important contribution to inelastic scattering, especially at high scattering angles. This contribution is particularly strong for heavy elements, whereas for light elements electron–electron scattering dominates at high angles (34).

Equation 2 describes the inelastic electron–electron scattering process as a Rutherford-type scattering, which is modified for small scattering angles by the second term in the bracket. In Equation 2 this factor is approximated by an empirical expression. In a concise quantum-mechanical treatment (35, 36) this term contains the probability that a crystal electron can be excited from an initial eigenstate ψ_i to a final eigenstate ψ_f, i.e., the transition-matrix element. Taking this into account, Equation 2 can be rewritten as

$$\frac{d\sigma_i}{d\Omega} \approx \frac{4\gamma^2}{a_0^2 q^4} \left| \left\langle \psi_f \left| \sum_j \exp(i\boldsymbol{q} \cdot \boldsymbol{r}_j) \right| \psi_i \right\rangle \right|^2, \qquad 3.$$

where $\boldsymbol{r}_j$ are the electron coordinates. The atomic number Z is now implicitly included in the sum. In a solid, the unoccupied final states are not discrete energy levels but can be described as energy bands with energy-dependent densities of states (DOS). Hence, the DOS enters into Equation 3 as an energy-dependent weighting factor. Because the initial states have discrete energies, the shape of absorption edges in EELS is determined by the product of the transition-matrix element and the density of unoccupied states. Schattschneider et al. (37) pointed out that Equation 3 is valid only under kinematic scattering conditions. In the case of strong excitations of Bloch waves, the expression has to be modified to the so-called mixed dynamic form factor (38).

The sharpness of the features observed in EEL spectra is limited by three effects: (*a*) Although the core level energy is discrete, the energy-loss spectrum will be broadened by the limited lifetime τ_i of the initial state. In other words, the core hole left behind by the excited electron is filled by other electrons from higher energy levels, either directly or via emission of Auger electrons. According to the uncertainty principle, the limited lifetime corresponds to a finite width of the measured energy level. The core hole lifetime limitation has long been known and was reported by Krause & Oliver and others (39–41) (Figure 10). The lifetime broadening owing to the core hole becomes stronger as Z increases and the angular momentum decreases. (*b*) Second, further broadening occurs by the limited mean free path (typically a few nanometers) (see Figure 11) of the excited electron, mainly by inelastic scattering events. This leads to a limited lifetime of the excited electron and thus again to an energy broadening. This effect is zero

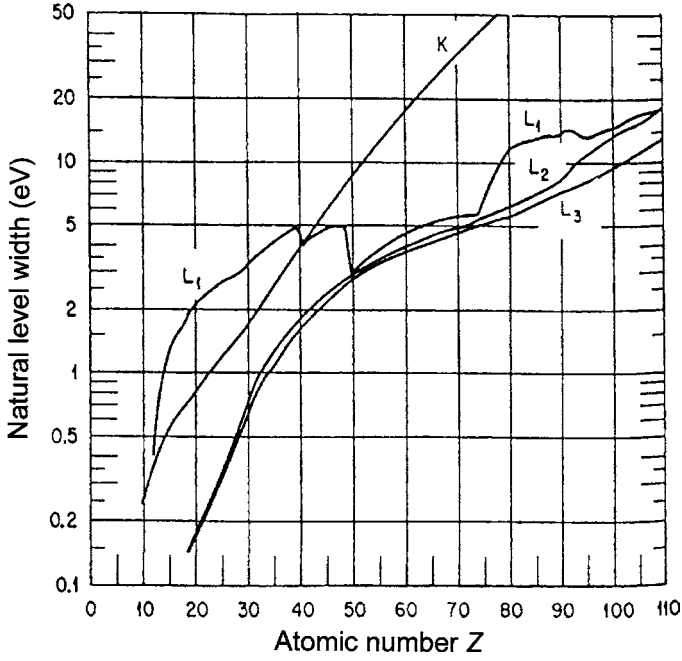

Figure 10 Line widths of electron transitions due to the limited lifetime of the core hole. Reprinted with permission from Krause & Oliver (39).

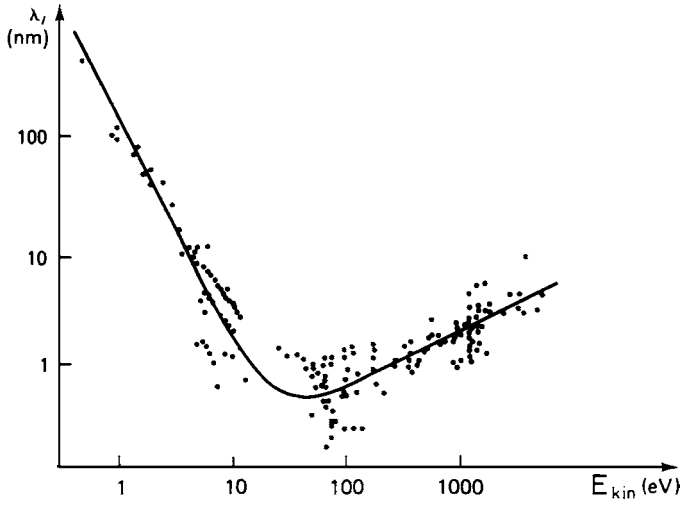

Figure 11 Inelastic mean free path of electrons as a function of their kinetic energy. Reprinted with permission from Egerton (17).

for electrons excited just to the edge onset energy and increases with energy loss (17). Well above the edge onset this effect dominates over the core-hole effect and leads to the broad wiggles in the extended region of the absorption edge (extended energy-loss fine structure, EXELFS) (42). (*c*) Finally, the instrumentation for the detection of the absorption edge can introduce a limitation to the energy resolution.

For $q \cdot r_j \ll 1$, i.e., if the length of the scattering vector is small compared with the average radius of the initial orbital, the exponential function in Equation 3 can be approximated by $(1 + i\boldsymbol{q} \cdot \boldsymbol{r}_j)$, and higher-order terms can be neglected (Dipole regime). The unity term cancels because the initial and final state wave functions are orthogonal. The vector product is non-zero only if the symmetry (angular momentum ℓ) of initial and final states is different.[1] In the case of dipole transitions ($\Delta\ell = \pm 1$), transitions from s- to p-states (e.g., K edges) or from p- to d-states (e.g., $L_{2,3}$-edges) are allowed. Therefore an absorption edge in EELS can be described by a site- and angular-momentum-projected density of states. The dipole selection rule may be violated if the DOS of dipole-forbidden transitions is much higher than the dipole-allowed states (44–46). Essex et al. (46) recommend not using the dipole approximation for energy losses below 50 eV. For low-energy losses the use of a small collection aperture (objective aperture in the TEM) ensures that non-dipole transitions are excluded from the EEL spectrum.

An alternative interpretation of the energy-loss spectrum is to consider it as the dielectric response of the material to the impact of the incident electron. The incident electron polarizes the material thus creating an electric field that acts back on the electron. In this formulation, the differential inelastic cross-section is given as (17)

$$\frac{\mathrm{d}\sigma_i}{\mathrm{d}E} = \frac{2\,\mathrm{Im}(-1/\varepsilon(E))}{\pi a_0 m_0 v^2 n_a} \ln\left[1 + \left(\frac{\beta}{\theta_E}\right)^2\right], \qquad 4.$$

where $\varepsilon(E)$ is the complex energy-dependent dielectric function, m_0 the rest mass of the electron, and n_a the atom density of the material. For a comparison with the experiment, the measured EEL spectrum is deconvoluted to obtain the single-scattering energy-loss function, *ELF*. This function compares with Equation 4 by $ELF = I_0 n_a t(\mathrm{d}\sigma_i/\mathrm{d}E)$, where I_0 is the intensity of the zero-loss peak and t is the specimen thickness. Because t can be calculated from the ratio of the total intensity of the spectrum and the zero-loss intensity, the dielectric function $\varepsilon(E)$ can be obtained from the EEL spectrum. The real and imaginary parts of the dielectric function $\varepsilon(E) = \varepsilon_1(E) + i\varepsilon_2(E)$ can be obtained by a Kramers–Kronig analysis. The real part is a measure of the polarizability of the material. The imaginary part

[1] A concise treatment of allowed and forbidden transitions, including the local symmetry around the excited atom, is given by Nufer et al. (43).

of $\varepsilon(E)$ describes absorption effects and is directly related with the joint density of states (JDOS) by

$$\varepsilon_2 E \propto JDOS \cdot \sum_i |\langle \psi_f | \nu_i | \psi_i \rangle|, \qquad 5.$$

where the sum describes the matrix element. This means that for low-energy losses, electron transitions from the valence to the conduction band are involved, i.e., the DOS of both bands is important.

Each inelastic scattering process is not only related to an energy loss but also to a change of the momentum of the scattered electron (Figure 12). This can be an additional source of information about the material. However, in most EELS experiments this dependence is not examined, and only electrons with scattering angles ranging from zero to β are selected by the collection aperture. Experimentally, larger scattering angles can be inspected by tilting the incident beam. From Figure 12 it is easy to show that for small scattering angles θ

$$q_{II} = k_0 \frac{\Delta E}{2E_0} \quad \text{and} \quad q_\perp \cong k_0 \theta. \qquad 6.$$

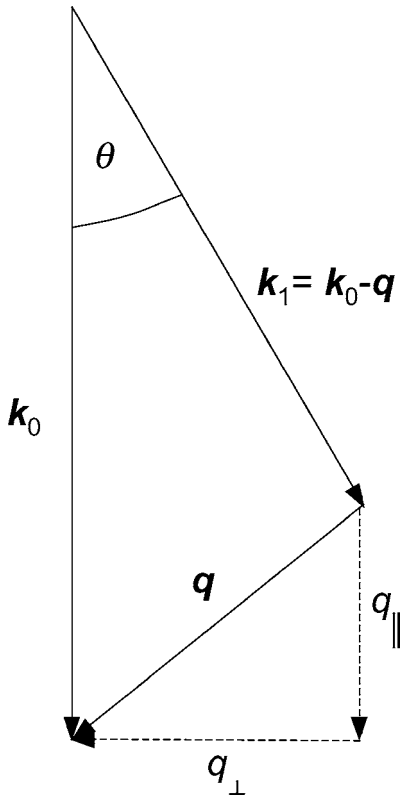

Figure 12 Electron wave vectors $\boldsymbol{k}_0$ and $\boldsymbol{k}_1$ and transferred momentum $\boldsymbol{q}$ in an inelastic electron scattering event. The momentum transfer can be decomposed into components parallel and perpendicular to the incident electron.

This means that for low-energy losses the momentum transfer is mainly perpendicular to the incident electron momentum, whereas for high-energy losses the parallel contribution can be quite appreciable.

Due to the scattering geometry and the limited size of the collection aperture (STEM) or objective aperture (TEM), only a certain angular range of scattering vectors enters the spectrometer, which can be used to obtain angle-resolved EEL spectra. Leapman et al. (47) proposed a method that was subsequently called the 45° method (48). The collection aperture is placed remote from the incident beam direction such that the magnitude of the perpendicular ($q_\perp$) and parallel ($q_\parallel$) components of the scattering vector $\boldsymbol{q}$ are equal (Figure 13). According to the above equations this position depends on the studied energy loss. In addition, the specimen is tilted so that a certain crystallographic direction $\boldsymbol{c}$ makes an angle of 45° with the incident electron beam. This means that the direction of the scattering vector $\boldsymbol{q}$ is then parallel to this crystallographic direction. By displacing the aperture to the opposite side of the incident beam, a spectrum with $\boldsymbol{q}$ perpendicular to this direction is obtained. In an alternative technique proposed by Browning et al. (49), EEL spectra are obtained with different collection angles. From these the parallel and perpendicular components are extracted.

A method to increase the angular resolution was presented by Midgley (50). After focusing the electron beam onto the specimen, the specimen is raised above the original position thereby resulting in a diffraction pattern with very high magnification (or angular resolution). Using a slit, a certain fraction of this pattern

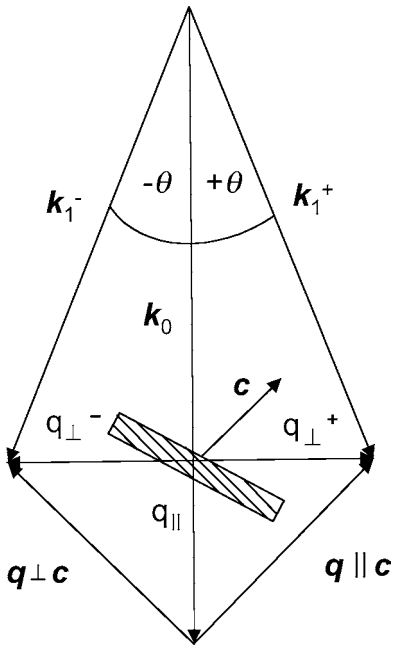

Figure 13 Scattering geometry used in the 45° method in order to obtain momentum-resolved EEL spectra (for details see text).

(corresponding to a certain range of scattering vectors) is allowed to enter the electron spectrometer. This permits direct imaging of the dispersion of features in the low-loss regime of the EEL spectrum, which helps to disentangle the physical origin of these features.

DATA ACQUISITION AND ANALYSIS IN EDXS AND EELS

The Signals Obtained by EDXS

The main advantage of EDXS over EELS is based on the fact that EDXS spectra are composed of peaks on a relatively low background originating mainly from bremsstrahlung. The removal of this rather smooth background is straightforward either by applying the second derivative of the spectrum or by fitting an analytical function to the background. Subsequently, peak intensities are determined by a fit of either a Gaussian function or peaks obtained from library standards, which are stored in a reference library in the computer. Although this library is often supplied by the manufacturer, it may be advisable to use one's own standards in order to optimize the quantification results.

Other minor contributions to the background are more difficult to separate from the real spectrum, such as

1. X-rays from areas not illuminated by the incident electron beam (e.g., from the pole piece of the microscope lens or, if the specimen is placed on a grid, from the grid material). These spurious X-rays can be excited by (back-) scattered electrons or by X-ray fluorescence. This signal is minimized but not eliminated by manufacturing the specimen stage from low-Z materials such as Be. It is partly possible to extract the remaining background signal by acquiring a hole spectrum where the incident electrons pass through the TEM specimen hole.
2. Similar to the above, secondary X-rays, which can be excited within the specimen itself.
3. Coherent bremsstrahlung, which can produce peaks in the bremsstrahlung background with shapes similar to X-ray peaks but with energy positions dependent on the energy of the incident electrons and the periodicity of the crystal lattice along the path of the incident electrons (51). Coherent bremsstrahlung is particularly strong if the crystalline material is oriented close to zone axes. These peaks cannot occur in amorphous materials, but they do occur in quasi-crystals (52).

Among the three contributions, X-ray fluorescence is probably the strongest effect. However, the prerequisite of strong X-ray fluorescence is that the energies of the original and fluorescing X-rays are close and that the original energy is the higher one. An example would be a steel specimen containing Cr and Fe, where Fe-K radiation can strongly excite Cr-K electrons. Clearly this effect changes the

relative intensities of X-ray peaks in the spectrum and thus leads to wrong quantitative results, especially when quantifying Cr composition in dilute Fe-Cr steels. It is not trivial to consider this effect in quantification procedures because it depends on the specimen geometry (also called geometric factor) (53). As mentioned above, X-ray absorption within the specimen can be a major problem if low-energy X-rays (<3 keV in typical TEM specimens) are used for quantification. Because this effect depends on the specimen geometry, it is very difficult to correct for it by means of spectrum-processing software. Despite this problem, methods have been developed to consider the absorption effects in the analysis (e.g., 54, 55). Apart from the low X-ray yield in low-Z materials, it is mainly this absorption effect that makes EELS the preferred method in light-element analysis. Watanabe (56) proposed a new quantification procedure (the ζ-factor method) in which absorption and fluorescence effects are incorporated. It might replace the traditional Cliff–Lorimer method (57).

Signal Processing in EFTEM

Three images are sufficient to obtain a distribution map of a certain element: two from the pre-edge energy-loss range and one image from the edge area (58, 59). The pre-edge images are used for background subtraction (Figure 14). When crystalline materials are studied, a frequent problem is the preservation of diffraction contrast in inelastic images (60–65, 67). If only the amplitudes of diffracted beams are considered, this effect occurs when an area of the specimen is under strong

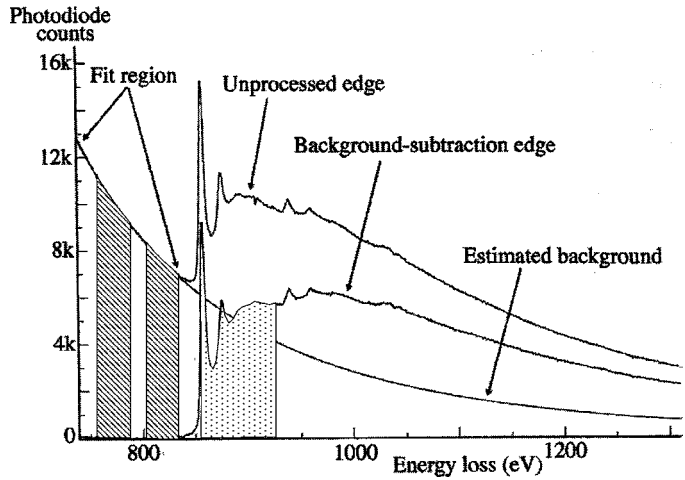

Figure 14 Three-window method used in EFTEM in order to obtain elemental distribution maps. Images using energy losses from the hatched areas are used for background subtraction. The signal is obtained from the third window above the edge onset.

diffraction conditions and most of the electrons are scattered under angles that are beyond the allowed range determined by the objective aperture. There are methods such as beam rocking (68) that reduce the effect; however, this is at the expense of lower intensity and thus a lower signal-to-noise ratio (SNR). The preservation of diffraction contrast is particularly pronounced under conditions used for atom-resolved imaging, i.e., zone-axis orientations of the crystal. Under such conditions, Bragg diffraction is strongly pronounced and can be described by strongly excited Bloch waves (see above). The spatial information contained in these Bloch states is partly preserved even after an inelastic scattering process (69). Navidi-Kasmai & Kohl (70) showed that the thicker the specimen the stronger the effect and that even for thin specimens this effect cannot be prevented, which means that interpretation of atomically resolved EFTEM images (71) is always difficult (see also below).

In order to reduce diffraction contrast in energy-filtered images the jump-ratio method (58, 72, 73) can be used instead of the three-window method. In the jump-ratio method only two images are acquired: those from energy losses below and above the edge onset (Figure 15). In the ratio image, diffraction effects are eliminated because the elastic diffraction effect included in the two energy-loss windows is almost the same due to their close proximity. Moore et al. (74) showed that the elimination of diffraction contrast is not complete, particularly at low-energy losses. In order to improve this, Crozier (59) suggested dividing ratio images by an image taken at very low-energy loss. Unfortunately, ratio images give only qualitative information about the chemical composition of the specimen, i.e., they cannot be used for quantification.

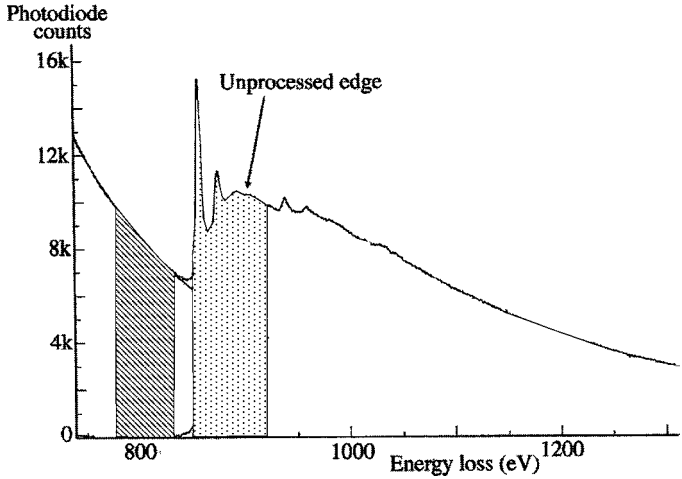

Figure 15 Energy-loss windows used in the jump-ratio method. The final image is obtained by a division of the dotted and hatched windows. Background subtraction is not done in this case.

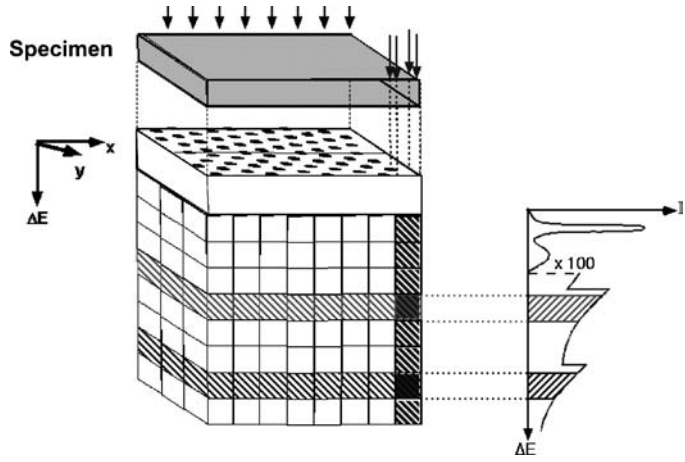

Figure 16 Data cube used to illustrate the collected data in a three-dimensional way. In a STEM, a full EEL spectrum is obtained from the illuminated area. In EFTEM, a full image is obtained from electrons that have suffered certain energy losses. This requires an energy filter as shown in Figure 2.

Acquisition of Data Series by EELS and EFTEM

The information content available from EELS or EFTEM can be represented through use of the data cube (75) (Figure 16). The x- and y-axes determine the lateral position of the investigated area and the z-axis is the energy-loss axis. In a normal elemental map obtained by EFTEM, slices parallel to the x/y-plane are obtained with thicknesses given by the width of the mechanical slit behind the energy filter. An EEL spectrum obtained from a selected position on the specimen corresponds to a line parallel to the z-axis. The entire data cube can be filled with data in two ways (Figure 16).

STEM SPECTRUM IMAGING Subsequent EEL spectra are recorded in the STEM from individual positions by scanning the focused electron beam (76–79). Each EEL spectrum has the full energy resolution determined by the spectrometer and the electron source. The acquisition time can be long. Owing to specimen drift, image distortions can be introduced that are almost impossible to correct after the data acquisition. The individual spectra can be analyzed after the acquisition using standard EELS analysis software.

EFTEM IMAGE SPECTROSCOPY Images are recorded from electrons of subsequent energy loss ranges. In this mode, each image contains the full image information; however, this occurs at the expense of lower energy resolution in contrast to that of the STEM approach (80–89). Post-acquisition specimen drift compensation is

possible in this case, although it is complicated if strong contrast variations are present in the images. Then image processing such as the application of Laplacian filters may simplify the drift-compensation process (86). Using a combination of energy-filtered series of the low-loss region and of the core-loss region, Mayer et al. (85) were able to obtain quantitative results by EFTEM image spectroscopy. This method was further developed by Thomas & Midgley (89) who acquired an EFTEM series across a continuous energy range including the zero-loss peak. This method makes full data analysis possible, including plural-scattering deconvolution.

In order to compare the two approaches let us assume a data cube of dimension $N^2 \times M$, i.e., the area of interest is divided into $N \times N$ pixels and the energy loss range contains M elements. The acquisition time for each pixel in STEM is τ_S, the acquisition time of each energy-filtered image in EFTEM image spectroscopy is τ_E. The total beam currents are I_S and I_E, respectively. If we want to have the same statistics within each pixel (i.e., $\tau_S I_S = \tau_E I_E / N^2$), we need an M times higher total current in EFTEM image spectroscopy than in EELS spectrum imaging. If we assume a typical total current of 200 pA in EELS spectrum imaging and of 1 μA in EFTEM image spectroscopy, an area of 100 $\times$ 100 pixels would therefore give a data cube with comparable statistics. The total acquisition time in EELS spectrum imaging would be $T_S = N^2 \cdot \tau_S = (I_E/I_S) \cdot \tau_E \approx 10{,}000\ \tau_E$ and in EFTEM image spectroscopy $T_E = M \cdot \tau_E$. Because typical values of M are well below 10,000, EFTEM image spectroscopy is the faster approach. This example shows that EFTEM image spectroscopy is superior if large areas with many pixels are recorded, whereas EELS spectrum imaging has advantages for small pixel numbers because the energy resolution does not depend on N. The total current per pixel is $\tau_S \cdot I_S$ ($= \tau_E \cdot I_E / N^2$ in the case of the same statistics as in EFTEM image spectroscopy) in EELS spectrum imaging and $M \cdot \tau_E \cdot I_E / N^2$ in EFTEM image spectroscopy. Therefore, the total electron dose is larger by a factor of M in EFTEM image spectroscopy. In the case of radiation-sensitive materials, M should be small in EFTEM image spectroscopy.

A special technique to obtain a continuous series of EEL spectra along a line was demonstrated by Reimer et al. (90) and was applied later on by several groups (91–96). This so-called spectral profile technique makes use of a slit above the energy filter oriented perpendicular to the energy-dispersive direction of the filter. In the energy-dispersive plane of the filter an EEL spectrum is visible for each position along the slit. The advantage of this technique is the simultaneous acquisition of all data. Thus specimen drift or energy instabilities are almost negligible. Walther (96) reported that for a TEM with high-energy stability and a high stability of the spectrometer currents, chemical shifts of 0.01 eV should be detectable. An interesting application of the method is the study of interfaces and grain boundaries by placing the slit perpendicular to the interface. A rotation specimen holder is advantageous in order to orient the interface exactly with respect to the fixed slit orientation.

Quantification

The intensity of a peak in an energy-dispersive X-ray (EDX) spectrum or under an absorption edge in EELS can be written as

$$I_X \propto I_0 \cdot \sigma_X \cdot t \cdot C_X \cdot n, \qquad 7.$$

where I_0 is the intensity of the incident electron beam, t is the specimen thickness, σ_X the cross-section for inelastic electron scattering of the element X under study, C_X is the concentration of element X in the illuminated volume, and n is the atom density. I_0, t, and n can be eliminated by using ratios of peak or edge intensities (e.g., of elements A and B):

$$\frac{I_\mathrm{A}}{I_\mathrm{B}} \propto \frac{\sigma_\mathrm{A} \cdot C_\mathrm{A}}{\sigma_\mathrm{B} \cdot C_\mathrm{B}}. \qquad 8.$$

This is the standard technique in EDXS. Together with the knowledge of $C_\mathrm{A} + C_\mathrm{B} = 1$ (in a binary system) the concentrations of elements A and B can be calculated. The proportionality factor between intensities and concentrations is called Cliff–Lorimer factor (57). For details the reader is refered to Reference 97.

In EELS, I_0 can be directly measured from the low-loss part of the EEL spectrum. This also allows quantification of single edges (in units of atoms per unit area) by dividing the core-loss signal by ($\sigma_\mathrm{X} \cdot I_0$). The inelastic cross-sections for K edges can be calculated using the SigmaK program of Egerton (17, 98), which gives a typical accuracy of about 10% [see also Hofer (99)]. The accuracy for L edges (and even more so for M edges, etc.) is lower, typically 10–20%. A source of error in EELS quantification of elemental concentrations is multiple inelastic scattering, which becomes important at specimen thicknesses above about 0.3 inelastic mean free paths. Multiple scattering basically leads to a convolution of the absorption edge with the low-loss part of the EEL spectrum. Deconvolution algorithms can be used to obtain the single-scattering intensity (17). Quantification errors introduced by the background subtraction are discussed below.

It has been shown by Knippelmeyer et al. (100) that relativistic effects become important at kinetic energies of the incident electrons, E_0, above 200 kV and that these should be considered in the quantification process. In the case of K edges, they found deviations between 5 and 20% at $E_0 = 400$ keV and between 10 and 70% at $E_0 = 1200$ keV.

Spatial Resolution

If a focused electron probe is used (e.g., in the STEM), spatial resolution is primarily determined by the size of the electron probe. As shown above, the probe size is typically a few Ångstrøm for field-emission TEMs and close or below 1 Å if a C_s corrector for the illumination system is used. Nowadays it is possible

to focus the electron probe onto a single atom column in a zone-axis orientation of a crystalline material. As mentioned previously, under such conditions a strong 1s-type Bloch wave is excited that is concentrated close to the nuclei of the atom column (axial channeling) (101–103). This strong localization of the electron intensity allows one to obtain an EELS signal largely originating from a single atom column. Lupini & Pennycook (104) showed that large collection apertures are necessary to achieve atomically resolved EELS. This will increase the fraction of nondipole transitions.

It has been argued that even a small shift of the electron probe away from the very column position leads to considerable loss of intensity to the neighboring atom columns (105). Furthermore, the electron intensity spreads with increasing specimen thickness away from the central atom column (dechanneling) (101, 106). In C_s-corrected TEMs, one must further consider that the convergence angle is much higher than that in uncorrected instruments. This large convergence leads to an increased dechanneling of the electrons away from the central atom column. Dwyer & Etheridge (107) calculated the EELS signal for different probe sizes and crystal orientations and found that atomically resolved EELS is possible for small specimen thicknesses and small probes. However, the strong variation of the electron intensity through the crystal by dynamic scattering can lead to misinterpretations in cases where atoms are not distributed homogeneously along the electron trajectory. On the other hand, this effect might be used to detect the z-location of a dopant atom within an atom column (106).

Under arbitrary specimen orientations and in thicker specimen regions (typically >30–70 nm depending on Z), the beam broadening owing to elastic scattering within the specimen (54, 108–112) becomes the resolution-limiting factor. Alber et al. (112) have shown that high-resolution chemical information can still be obtained if this broadening is quantitatively taken into account. Unlike in EDXS, in EELS the whole broadening is not relevant because the limited collection aperture β cuts off the tails of the broadened electron probe. On the basis of purely geometric arguments Egerton (17) showed that the broadening in EELS can be approximated by $2r \approx \beta t$.

Several authors have described spatial resolution in inelastic scattering by the convolution of the electron probe function with the so-called inelastic object function (113, 114). The latter is equal to the inelastic response of an atom for a perfectly localized electron beam.

At low-energy losses, the spatial resolution, d, is limited by the delocalization of inelastic scattering (115–118). This effect has its origin in the small characteristic inelastic scattering angle θ_E at low-energy loss (see above), which, according to the Rayleigh criterion $d \approx 0.6\,{}^{\lambda}/_{\theta_E}$, limits the spatial resolution. However, as Muller & Rose (119) point out, about 50% of the electrons is scattered at angles larger than θ_E, which diminishes the delocalization effect. This is supported by results of van Benthem et al. (120) who found that the effect of delocalization at energy losses below 20 eV is less severe than those predicted by the models of Pennycook & Narayan (116) and Muller & Silcox (118).

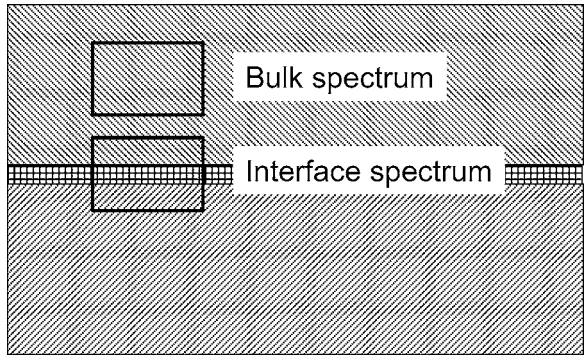

Figure 17 Illustration of the spatial difference technique. By comparing two spectra obtained in the bulk or on the interface, an interface-specific spectrum can be obtained.

In order to detect the interface-specific energy-loss near-edge structure (ELNES) or segregation at interfaces, the so-called spatial difference (SD) method has been applied in many studies (121, 122). With this technique spatial resolution is obtained by subtracting a spectrum from an area (usually rectangular) containing the interface, I_{IF}, from a bulk spectrum, I_{bulk}: $I_{SD} = I_{IF} - \xi I_{bulk}$ (Figure 17). The method is based on the assumption that the signals stemming from the bulk and the interface region overlap incoherently. Because no focused probe is used, the spatial resolution of this technique is not limited by the probe size. A main advantage of this technique compared with that of spot measurements is that the position of the beam can be monitored during the EELS or EDXS data acquisition, i.e., specimen drift can actively be compensated for. Furthermore, beam damage can be reduced if dose rate is a problem for the material investigated. The weighting factor ξ corresponds to the fraction of bulk-like information contained in the interface spectrum. This factor is often determined empirically during the subtraction procedure. Nufer (123) determined ξ by calculating the ELNES for atoms at different distances from the interface. Using this "interfacial width" he found excellent agreement between experiment and theory demonstrating the validity of the spatial difference approach. This validity was also demonstrated by Scheu et al. (124, 125) who measured the difference signal for different positions of the interface within the rectangular area. The same results were obtained in all cases. The SD method has been criticized by Muller (126), who pointed out that subtraction of spectra with small energy shifts with respect to one another (e.g., due to chemical shifts or energy instabilities) can give completely artificial results in the difference spectrum. Although this poses a problem for the technique, careful data acquisition and analysis can minimize such artifacts.

In another approach, the interface-specific EEL or EDX spectra are obtained by multivariate statistics (127, 128, 128a) by sorting spectra from a line scan or a two-dimensional map of the interface region according to their similarity

(129–131). The N spectra, each with M energy channels, are treated as an $N \times M$ matrix and the eigenvectors of this matrix constitute the axes of an N-dimensional space. Within this space the position of all N spectra are displayed. This method is able to find weak differences of spectra in the large data sets. Furthermore, it is objective because it basically relies on a statistical evaluation. It should be mentioned that there are other statistical approaches such as the use of neural networks (132).

In EFTEM, chromatic aberration is usually the limiting factor for spatial resolution because of the wide range of energy losses allowed by the selecting slit. For a slit width δ the chromatic broadening is given by $C_c \cdot \beta \cdot \delta/E$. In principle this effect can be reduced by using a small objective aperture, but this can introduce a blurring by diffraction ($= 0.61\ \lambda/\beta$ with the electron wavelength λ). The final resolution in EFTEM is thus determined by these contributions added in quadrature (133). Figure 18 shows the individual contributions and the total EFTEM resolution as a function of the objective aperture size for a 200 keV TEM with $C_c =$ 2 mm and $C_s = 2$ mm. This example shows that there is an optimal size of the diffraction aperture. However, in practice it may happen that larger apertures have to be used in order to increase the SNR. In Figure 19 the energy-loss dependence of the resolution-limiting factors is shown. In fact, only the delocalization of inelastic scattering is energy-loss dependent. In the case of best resolution at high-energy

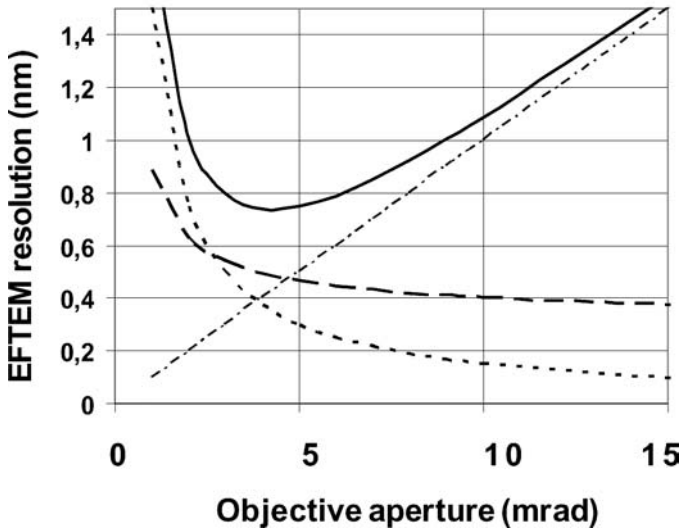

Figure 18 Spatial resolution in EFTEM as a function of the objective aperture size (which limits the collection angle) in a TEM. Limitations result from diffraction ($\cdots$), delocalization ($- - -$), and chromatic aberration ($- \cdot - \cdot$). These can be summed in quadrature to obtain the total resolution limit (—). Parameters: electron energy 200 keV, $C_s = C_c = 2$ mm, 10 eV width of the energy-selecting slit, energy loss 285 eV.

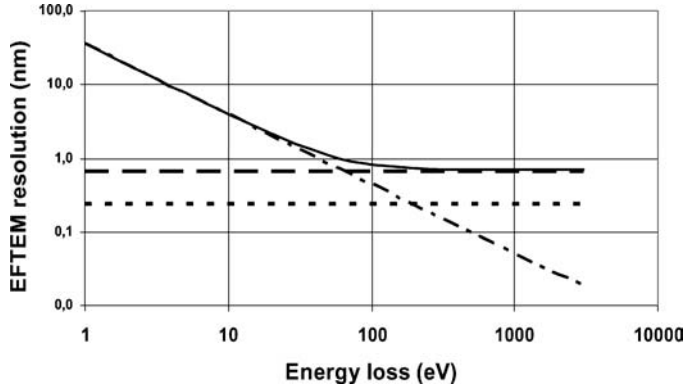

Figure 19 Spatial resolution in EFTEM as a function of the energy loss. Limitations are due to chromatic aberration (– – –), delocalization (– · – ·), and diffraction (· · ·). These are summed in quadrature to obtain the total resolution limit (—). Parameters: objective aperture 6.5 mrad, $C_c = 2$ mm, electron kinetic energy 200 keV, width of the energy-selecting slit 10 eV.

losses, the horizontal lines for chromatic aberration and diffraction limit overlap. Delocalization is important only for energy losses below 100 eV; in the case of large slit widths (≥20 eV) only below 20 eV. A way to reduce the effect of chromatic aberration in EFTEM is to use a series of energy-filtered images across the energy range of interest using a narrow energy-selecting slit.

In a number of articles the possibility of atom-column resolution in EFTEM has been addressed. Lattice images can be formed from inelastically scattered electrons, e.g., by using electrons which have undergone a plasmon loss (69, 134–140). The resolution is affected by the width of the energy-selecting slit due to chromatic aberration. Unfortunately it is usually not possible to directly interpret such images as atomically resolved elemental maps. This is due to the preservation of contrast from elastic scattering (141), i.e., the elastic part of the image contrast cannot simply be subtracted from the image. Notwithstanding this problem, there are examples which are likely to show atomic resolution in EFTEM images (71, 96). Kimoto et al. (142, 143) showed how the contrast of lattice fringes changes with energy loss because the energy loss leads to an effective defocus change.

Egerton (34) discussed spatial resolution in EELS and EFTEM taking into account both elastic and inelastic scattering.

Signal-to-Noise Ratio and Detection Limits

Characteristic X-ray peaks as well as absorption edges in EELS are always superimposed on a background signal. Furthermore, experimental data always suffer from statistical noise. Both effects lead to a lower limit of detectability. Generally, the presence of a peak or an edge can be regarded with 98% certainty if the peak

(edge) intensity exceeds three times the standard deviation of the background signal. Often the Rose criterion (144) is used, which states that a factor of five instead of three should be used.

In EDXS, the typical detection limit in terms of a concentration (minimum mass fraction, MMF) is in the range 0.1 to 1 at%. However, because small volumes are probed, this can correspond to the detection of a small number of atoms (minimum detectable number of atoms, MDN). Watanabe & Williams (145) demonstrated a MDN of two atoms for the detection of Mn in a Cu matrix using EDXS. They state that this can be achieved only in thin specimens in order to minimize beam spreading and thus to keep the probed volume small. One should keep in mind that the best experimental conditions for small MMF and small MDN are not the same. For small MMF, high beam current is mandatory, which may be advisable to illuminate across a large area to prevent specimen damage. For small MDN, a small probe is important, which poses a limit to the total current.

The problem of SNR in EELS was discussed (among others) by Egerton (17), Berger & Kohl (146), and Overwijk & Reefman (147). The main difference between EELS and EDXS in SNR is that it is much more difficult to remove the background signal in EELS than in EDXS. Due to the better signal collection in EELS, MMF can be in the range of some 10 ppm in favorable cases. Near-single atom detection was reported by Mory & Colliex (148) and Krivanek et al. (149). Suenaga et al. (150) demonstrated single-atom detection by EELS spectrum imaging. Leapman (151) studied biological specimens and found that the four Fe atoms in a hemoglobin molecule are detectable, and in the case of calcium, even single-atom detection was found to be possible, both cases having a SNR of 5. These results were made possible by the use of a modern CCD exhibiting high detection quantum efficiency. Feng et al. (152) proposed using ratios of differences of three EEL spectra, which were taken in a series. These ratios are independent of gain variations of the detector and thus improve detection of trace elements.

Recently Menon & Krivanek (153) presented a software package to model entire EEL spectra. This can be used to find detection limits and to optimize the experimental conditions.

Noise is a frequent problem in EFTEM images (58) because the number of electrons within the selected energy-loss range is small (mainly at high energy losses) and because the total intensity is distributed over N by N image pixels. In principle, the SNR can be improved by increasing the exposure time, but this can introduce artifacts from specimen drift or radiation damage. This problem was treated by Berger et al. (154) and Kohl & Berger (155). Berger et al. state that the SNR can be improved by placing one pre-edge window close to the edge onset, with the second window shifted as much as possible to lower energies, taking into account that the parameters A and r are only constant in a limited energy-loss range. This was stated more precisely by Hofer et al. (58) and Kothleitner & Hofer (156): For saw-tooth-like edges (like many K edges) and L edges with white lines, the window close to the edge should be 20–30 eV wide. For delayed edges, the post-edge window should be positioned at the maximum of the edge and should

be wide (e.g., 120 eV for the Si-L edge). Though this choice gives best SNR, the spatial resolution could suffer owing to chromatic aberration.

Energy Resolution

In EELS the energy resolution is primarily determined by the energy width of the incident electron beam (see Table 1). The energy width can be improved by the use of electron monochromators. At 190 nm spatial resolution, Terauchi et al. (157) obtained an energy resolution better than 0.1 eV. Using a special design, Fink (158) obtained spectra with 80 meV resolution, however, at a spatial resolution of only about 1 mm. The need for high-energy resolution combined with high spatial resolution was discussed by Batson (159) using the example of Si-based semiconductor devices. First results at spatial resolution in the nanometer range obtained with a Wien-filter monochromator were shown by Mitterbauer et al. (160) and Lazar et al. (161) using TEM and using a STEM. Mitterbauer et al. studied O-K edges and transition metal-L edges in transition metal oxides. They found that for most L edges a marked gain of fine structure was found. However, the O-K edges did not improve compared with spectra without monochromator. This was ascribed to solid-state effects, in particular the limited lifetime of the excited electron and the core hole (see above). This issue was also discussed by Brydson et al. (162) who came to similar conclusions.

The energy resolution can be further affected by the detector and lens aberrations in the spectrometer. Limitations by the spectrometer detector can be from its point-spread function (strongly pronounced in photodiode arrays) or simply from the use of very small dispersions such that the energy range per detector element exceeds the energy width of the emitter. The chromatic aberration of the lenses used in the spectrometer leads to an energy-loss dependence of the energy resolution, i.e., after optimizing the energy resolution at the zero-loss peak (which is usually done because of the strong signal), the energy resolution is worse at higher energy losses. This effect can be avoided by increasing the high voltage by the same amount as the energy loss of interest. This is done in modern TEMs.

If the exact shape of the zero-loss peak is known, EELS data can be deconvoluted with this peak thus removing all instrumental broadening effects (163). However, one has to be aware of possible artifacts. For example, Fourier deconvolution techniques increase noise, which can lead to artificial peaks in the ELNES. Using the Richardson–Lucy deconvolution algorithm, Gloter et al. showed EEL spectra with 0.2–0.3 eV resolution (163). Overwijk et al. (147, 164) used the maximum entropy method for deconvolution. This technique leads to a noise optimization in the deconvoluted spectrum.

In EFTEM the energy resolution is usually determined by the width of the energy-selecting slit. This is typically of the order of a few eV which, in EFTEM image spectroscopy, corresponds to a rather poor sampling of the energy space. In order to apply multiple scattering deconvolution procedures to spectra extracted from such EFTEM, image series data are frequently interpolated, e.g., using fast

Fourier transform (FFT) methods (165). Future energy filters with a very high dispersion and transmissivity, such as the MANDOLINE filter, allow use of very narrow slits. In this case the energy resolution may be determined by the energy width of the emitter, just as in EELS.

Background Subtraction

Absorption edges are superimposed on a background originating from excitations of electrons to high vacant energy levels or (in thicker specimens) from multiple energy losses including plasmon losses. For quantification, this background has to be removed, which requires the knowledge of the shape of the background function. If energy losses above ~100 eV and thin specimens are used, the inverse power-law function $A \cdot \Delta E^{-r}$ usually gives satisfactory results (17). Alternatively polynomials, exponential or log-polynomial functions, or multivariate statistics approaches (127) can be used. If the shape of the background (before and after the edge) is known from a standard material not containing the element of interest, a polynomial fitted to this shape may be a promising approach (166).

In normal EEL spectra, the function is fitted to a certain energy range in front of the edge and then extrapolated to energy losses after the edge (17). Clearly, the wider the energy range of interest, the larger are the extrapolation errors. In the case of EFTEM, the simplest approach is the use of two pre-edge energy-loss windows. The parameters A and r are calculated from the two intensity values. The accuracy can be improved if energy-filtered series are used with images having reasonably good statistics. Alternative approaches are discussed by Egerton & Malac (167). At low-energy losses the inverse power-law function is not appropriate.

Overlapping Peaks/Edges

Overlapping peaks in EDXS can be isolated by standard deconvolution. However, owing to the poor energy resolution there are combinations of materials for which such procedures do not work. In EELS such simple procedures are not applicable because the shapes of the various edges are not simple and depend on the element as well as on the environment of the excited atom. Furthermore, absorption edges cover wide energy ranges so that overlap is much more likely than in EDXS. Several procedures have been proposed to overcome this problem:

1. The intensity of the low-energy edge underneath the high-energy edge can be estimated by calculating the partial inelastic cross-section within the high-energy region. This was done by Chan & Williams (168) in the case of an Al-Li alloy.
2. Approximate edge shapes can be obtained from standard specimens and a synthetic spectrum can be calculated, including the inverse power-law (or any other) background. By a least-squares fit to the experimental spectrum, the edge intensities are calculated (169–172). This was recently further developed (173–175).

More Sophisticated Analysis of EFTEM Series and STEM Spectrum Images

Unfortunately, an automized analysis of EEL spectra is at present not available. This would be particularly useful for the analysis of a large number of spectra as in energy-filtered series or in STEM spectrum images. However, Kundmann & Krivanek (175) have described a way for automatic detection of edges in an EEL spectrum. It is based on the derivative of spectra that is sensitive to the sharp onset of absorption edges. This is followed by a selection of those peaks having intensities that are statistically significant above the noise level. Using this approach, elemental occurrence maps can be extracted from the original data cube (176). For quantification, correction for multiple scattering is necessary in thicker specimen areas. Clearly this also requires data from the low-loss region including the zero-loss peak. Once the elements are detected, their concentration can be determined by the usual approach mentioned above. Because the edge positions of the elements are known, the window widths for background subtraction and signal integration can be determined automatically. However, this fails if edges are too close. In this case the spectra can be synthesized using reference spectra as shown above.

By comparing different elemental maps, phases can be identified in a material. A simple method is to use colors for the different elemental maps and to overlap them, which results in a certain color value for each phase. In another approach a scatter diagram is used in which the axes correspond to the intensities of the maps. Suppose there are two elemental maps (e.g., from C and N) with $N \times N$ pixels. The intensity pairs of each N^2 pixels are transferred into the scatter diagram. All pixels of a certain phase will have a similar combination of intensity values in the two images and will therefore be located in the same area of the scatter diagram. By selecting areas with high pixel density in the scatter diagram and back tracing them into the elemental maps, the location of the phases can be determined (58). To circumvent diffraction effects, such phase maps are better performed from jump-ratio maps (see above).

Radiation Damage

During electron exposure the studied material may undergo a change in its atomic structure. This can be from (*a*) the direct knock-on process between electron and nucleus or (*b*) inelastic excitation (electron–electron scattering). In the first case the hit atom directly receives momentum from the electron (which is back scattered). It is the dominant damage process in metals and probably in semiconductors and ceramics. The knock-on damage has a lower threshold, i.e., it can be avoided by using sufficiently low electron energies. In the case of inelastic electron–electron scattering, atom displacement occurs during the relaxation process of the excited atom. The emission of secondary and Auger electrons leads to a positive charge. Because of the small illuminated region, a high-electric field strength develops that can expel positive ions (177). It is most pronounced in biological specimens and

polymers but also in inorganic materials such as ceramics. This type of damage cannot be prevented by lowering the electron energy because the inelastic cross-section would also increase. An improvement could be obtained by cooling the specimen or by coating it with a conducting film.

Depending on the material, the amount of damage may depend not only on the dose but also on the dose rate. In this case the size of the illuminated area should be increased in order to reduce the damage. In the study of interfaces, a strongly astigmatic beam aligned parallel to the interface can be used to probe a larger volume; in the STEM, a narrow rectangular area can be illuminated. In any case, it is advisable to acquire spectra at different doses and dose rates in order to determine whether damage actually occurs before starting with the real experiments.

An example of radiation damage in α-Al_2O_3 is shown in Figure 20. Electron irradiation of this material can lead to the formation of metallic Al and molecular oxygen (178). In Figure 20 sharp peaks at 531 eV and 15.3 eV appear after irradiation, corresponding to molecular oxygen and metallic aluminum (123). This damage occurs only with specimens that have been Ar ion–thinned at ion energies above about 3 keV. The ion bombardment introduces point defects that act as nucleation centers for the formation of oxygen bubbles during the electron irradiation in the TEM. The damage can be minimized by using lower ion energies or by heating the specimen after ion milling to anneal the point defects.

Radiation damage also occurs during the specimen preparation by ion sputtering. Apart from the atoms that are removed from the surface, atoms in the near-surface regions can be displaced from their regular lattice sites. The structural disordering can lead to an amorphization. Even worse for quantification in analytical TEM, different atoms in multi-element specimens are displaced with different cross-sections leading to a nonstoichiometry of the near-surface regions. This can be improved (but not avoided) by using low-energy ions and small inclination angles of the ion beam (179). Such surface nonstoichiometry can be checked by comparing the specimen composition at different specimen thicknesses.

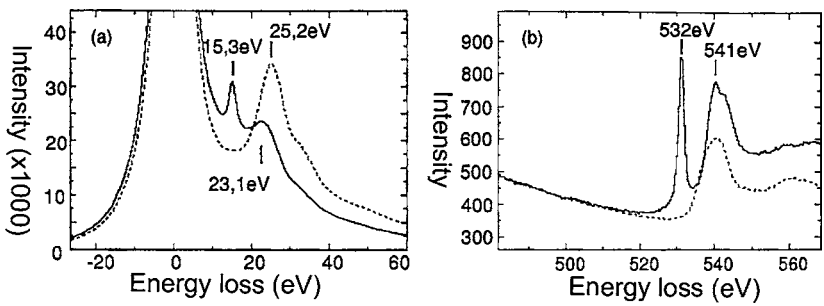

Figure 20 Low-loss and O-K spectra of Al_2O_3 before (· · ·) and after (—) electron irradiation. Reprinted with permission from Nufer (123).

For a recent review about irradiation-induced effects, including heating, charging, and contamination, the reader is referred to Reference 180.

CALCULATION OF THE ELNES

There are a number of approaches to calculate the fine structure of absorption edges based on first principles (181–187). The main purpose of such calculations is to obtain a relationship between the ELNES and structural properties in materials. This is not easily derived directly from EEL spectra. Due to the complexity of the problem, fingerprinting methods are frequently applied for the interpretation of EELS data. These methods rely on the comparison of the data with spectra obtained from known materials. Despite the strength of the fingerprinting approach there is always room for misinterpretations. Therefore reliable ab initio calculations will be of utmost importance in the future.

The theoretical methods can roughly be divided into real-space and reciprocal-space methods. Both should give the same results if properly performed. In real space the excited electron is treated as a spherical wave emanating from the atom. For excitation energies up to ~10 eV above the Fermi level, the inelastic mean free path of the excited electron is larger than the next-nearest neighbor distance (188) (Figure 11). Therefore, the electron wave is scattered at the potentials of several surrounding atoms. The interference of all waves leads to the fine structure of the absorption edge, which thus contains information about the type and position of surrounding atoms. The advantage of this multiple scattering approach is that the ELNES can be calculated for small clusters of atoms, i.e., no long-range periodicity is required as in the $\boldsymbol{k}$-space methods. The origin of ELNES features can be ascribed readily to different atom shells around the excited atom. In reciprocal space the eigenvalues of the system are calculated at several positions in the Brillouin zone. From the calculated band structure the density of occupied and unoccupied states is calculated, which directly reflects the ELNES. Apart from the information about the DOS, in this approach a (most probable) relaxed structure of minimum total energy can be determined. In the multiple-scattering approach, this is not possible. Note that, according to Equation 3, the transition matrix elements must also be considered for a quantitative comparison with EEL spectra; however, their energy dependence is usually rather smooth compared with the variations of the DOS.

The ELNES calculations are significantly complicated by two effects: (*a*) Calculations within the density-functional approximation give the ground-state electronic structure. In reality the excited electron and the core hole interact with each other and with all other electrons leading to changes in the band structure (final state effects) (189). In fact, the partial unscreening of the nucleus by the missing core electron leads to a contraction of the upper bands. This can be particularly strong in ionic solids, often leading to sharp features at the edge onset. In extreme cases excitonic states can appear near the edge onset, i.e., the excited electron and

the core hole can be treated as an electron–hole pair. There are methods to take final-state effects into account; for example, the Z + 1 approach (190–193), which treats the excited atom as an atom with increased nuclear charge (e.g., replacing an O atom by a F atom). Alternatively suitable pseudopotentials can be employed (frozen core hole) (181, 183, 193, 194). The core hole often leads to a localization of the wave functions in real space. The treatment of the core hole makes ***k***-space first-principles calculations time-consuming because large supercells have to be employed in order to prevent interaction of the core hole atoms (periodic boundary conditions!). Paxton et al. describe the use of Slaters' transition state theory to include final-state effects (195). (*b*) Most first-principles methods assume that the exchange energy density is locally the same as in a homogeneous gas of the same density (local density approximation). However, this can fail in systems with strong exchange and correlation effects, such as in magnetic materials or generally in materials with highly localized electron states (e.g., d- and f-orbitals in transition metals and rare-earth elements).

Köstlmeier (196) showed that the onset energy of K (ground state 1s) and L_1 edges (ground state 2s) can be calculated reliably only up to about $Z = 15$ (phosphorous). Elsässer & Köstlmeier (197) showed that the $Z + 1$ approximation accounts well for the final-state effects if the total-energy difference between two neighboring elements in the periodic table is similar to the excitation energy of the process under study.

ADDITIONAL METHODS

In this section, several TEM techniques are addressed that do not directly make use of spectral information such as EELS or EDXS, but still allow the retrieval of chemical information.

Z Contrast

Equation 1 shows that the differential cross section for elastic scattering is proportional to the square of the atomic number. This is true only for large scattering angles, typically well above 100 mrad for electron energies normally used in TEM. Therefore, by scanning the electron beam across the region of interest and using a HAADF detector, the resulting image contains chemical information. If the illuminating beam is small and oriented parallel to a zone axis of a crystalline material, the electron intensity can be confined almost to a single-atom column, which gives atomically resolved *Z*-contrast images (102, 103). For quantitative chemical analysis, comparison with image simulations is indispensable. The reader is referred to References 198–201 for some examples of this technique.

Z-contrast images can also be obtained by hollow-cone illumination and detection of electrons scattered to the proximity of the optical axis (202). However, the technique suffers from very low intensity because only a small fraction of

the scattered electrons is detected, whereas HAADF detectors detect all electrons scattered within a certain angular range.

ALCHEMI

It was shown above that the electron intensity varies within the unit cell of a crystal if Bragg reflections are excited. By intentionally varying the Bragg conditions by carefully tilting the specimen and using a simultaneous detection of EELS or EDXS signals, the occupancies of particular sites within the unit cell by specific elements can be determined. Spence & Taftø (29) introduced the acronym ALCHEMI (atom location by channeling-induced enhanced microanalysis) for this technique. The importance of delocalization of the inelastic scattering process for ALCHEMI was shown by Pennycook (117), Nüchter & Sigle (203), and Horita et al. (204). Oxley & Allen (205) show that the approximate expression given by Pennycook has to be modified. Important developments were made by Rossouw's group on the basis of their initial work (206) using a multivariate statistical approach.

Chemical Information from Elastic HRTEM Images

The contrast in high-resolution transmission electron microscopy (HRTEM) images is usually not directly interpretable in terms of chemical contrast, although there are exceptions. Ourmazd et al. (207) showed that by extracting the contrast originating from chemically sensitive reflections, one can determine the composition of each single unit cell. The method relies on pattern recognition and has been further developed (208–212).

Fresnel Contrast

Fresnel contrast occurs at edges where the average inner potential of the specimen changes. This can be applied to the study of thin films at grain boundaries that exhibit compositions different from the surrounding bulk material. By varying the defocus of the objective lens, one observes bright or dark contrast along the boundary. A comparison with calculation allows determination of the shape and magnitude of the potential across the boundary (213).

Tomography

In order to obtain three-dimensional information of an object shape, taking a series of images from various directions is a prerequisite. Several papers have demonstrated that this can also be performed by the use of EFTEM or STEM images (214, 215). Using this approach it is possible to get an element-specific three-dimensional image with a spatial resolution of a few nanometers. The available resolution and field of view is compared with other tomography techniques in Figure 21.

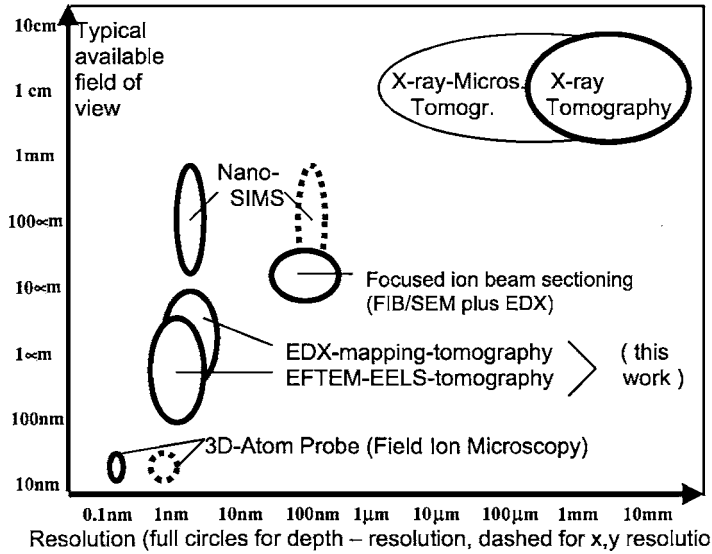

Figure 21 Comparison of different tomography approaches in terms of field of view and depth or lateral resolution. Reprinted with permission from G. Möbus et al. (214).

APPLICATIONS OF EELS AND EFTEM

The second part of this review concentrates on applications of analytical TEM, with the intention of giving the reader an idea of the type of information that can be extracted for particular material systems. The given references usually contain citations for further reading, and may thus be helpful as a starting point. An attempt to review the whole literature on this subject is simply not possible. We begin with some general remarks on low-loss EELS and anisotropic materials. This is followed by a discussion of core-loss studies of particular material systems, generally in the order of atomic number. Finally, special studies on interfaces, grain boundaries, and dislocations are addressed.

Low-Loss EELS

It was shown in Equation 4 that the EEL spectra contain the entire dielectric information $\varepsilon(E)$ necessary to calculate optical properties. The data analysis starts with a deconvolution algorithm [typically a Fourier-log deconvolution (17)] in order to obtain the single-scattering intensity. This is followed by several simple mathematical operations. Finally a Kramers–Kronig analysis separates real and imaginary parts of the dielectric function. Some examples have been given by Wang (216), Dorneich et al. (217), Müllejans & French (218), French et al. (219, 220), Ryen et al. (221), Rafferty & Brown (222), and van Benthem et al. (223).

In the formalism of dielectric theory the energy loss of the impinging electron polarizes the dielectric medium. The electric field connected with this polarization exerts a force on the electron that, integrated over the path of the electron, results in a certain energy loss. A general introduction to plasmons in solids can be found in Reference 224. Theoretical and experimental studies of the low-energy-loss region for special specimen geometries and crystal symmetries have been done by several groups. von Festenberg (225) calculated plasmon losses in systems containing thin films. Ferrell & Echenique (226) used classical dielectric theory to describe the dielectric loss for specimens of arbitrary geometry.

Ritchie (227) and Otto (228) pointed out that the free surfaces of a thin foil may lead to a reduced polarization and thus to a lower energy loss than in the bulk. Using the Maxwell equations, Economou (229) took account of the retardation effects that have a significant influence on the plasmon modes. A classical treatment of surface excitations was performed by Howie (230). This was extended to relativistic electrons moving parallel to the interface of two media with different dielectric functions by Garcia-Molina et al. (231). Howie (232, 233) points out that the sensitivity to the interface-specific dielectric function can be increased by using electrons scattered to higher angles. The energy loss function of an electron passing a multilayer material (both perpendicular and parallel to the layers) was studied by Bolton & Chen (234), who found interface plasmons in addition to bulk plasmons. The interface plasmons are weak for boundaries between two similar materials, for example, between two semiconductors. These interface features are more pronounced in the case of parallel incidence. Another study of dielectric losses in multilayers can be found in Reference 235.

Batson (236) studied the energy loss of an electron passing an Al sphere covered with alumina. He found a coupling between two close spheres that resulted in a loss peak at 3.2 eV, which is well below the surface plasmon peak at 6.7 eV. The effects of the dielectric coupling of small spheres to a substrate were theoretically treated by Ouyang & Isaacson (237). They found a reduced surface plasmon intensity. The same authors (238) extended the theory to arbitrary particle shapes. Echenique et al. (239) applied the theory of Ferrell & Echenique (226) to oxide-coated and uncoated spheres. Ugarte et al. (240) used EELS and EFTEM to study plasmon excitation in small Si spheres coated with SiO_2. A surface mode was found at an energy loss of 3–4 eV and this was imaged by energy-filtered imaging in the STEM (241, 242).

Chu et al. (243) performed a non-relativistic study of the energy loss of electrons passing a hollow cylinder parallel to the cylinder axis. For narrow cylinders, mainly bulk plasmons are excited, whereas the plasmon peak shifts to lower energies toward the surface plasmon peak with increasing cylinder radius. This was extended to the relativistic case by De Zutter & De Vleeschauwer (244) (see also 245, 246).

The energy loss close to the edge of a wedge (which is a typical geometry found in TEM specimens) is discussed in References 247, 248.

The work mentioned above assumed bulk-like dielectric functions. This assumption may not be applicable in structures of atomic dimensions. Ekardt (249) calculated the dielectric response of small metal particles in the time-dependent

local density approximation and found that bulk plasmon excitation disappears below a critical cluster size. The bulk plasmon energy increases with decreasing cluster size owing to the quantization of electronic states, whereas the surface plasmon energy decreases because of an increasingly diffuse surface. Mitome et al. (250) found a d^{-2} dependence of the volume plasmon energy in small Si clusters (d, cluster diameter), which is opposite to the case of metal clusters. They argue that the effect results from the d dependence of the energy gap.

The change of the optical properties across an Al–SiO_2–Si field emitter structure was performed by Turowski & Kelly (251, 252). Recently, a similar approach was used for the study of a grain boundary in $SrTiO_3$ (120, 253). From local changes of the electronic structure dispersion forces can be quantified from the low-loss EEL spectrum. van Benthem et al. found a reduction in the number of transitions in the grain boundary region. From this finding a reduced atomic density and thus a reduced valence electron density in this region was deduced. With the assignment of the spectral features to specific transitions, it was concluded that the lower density was mainly from a loss of oxygen atoms. This is consistent with results by Browning and coworkers (254). It is argued that the London dispersion makes an important contribution to the grain boundary energy. The role of the Landau dispersion for the stability of intergranular films in silicon nitride is discussed by French et al. (220). It was found that the film thickness scales inversely with the Hamaker constant. Lo et al. (255) used EFTEM image spectroscopy in the low-loss region to obtain two-dimensional information about optical properties in a SiO_2-based low-k material. Because the sampling of the energy scale was too rough in EFTEM, they applied a FFT interpolation algorithm. This was followed by the normal Fourier-log deconvolution and Kramers–Kronig analysis.

A critical step in the low-loss data analysis is the subtraction of the zero-loss peak because there is no simple mathematical function that would fit to the whole tail of the peak. Therefore, an analytical function is fitted to only a certain range of the tail. Alternatively, Fourier-ratio deconvolution can be applied (256). Also non-Fourier space methods were reported (257, 258) that use the zero-loss peak recorded without the specimen as a reference function. Bangert et al. (259) found that the noise introduced by deconvolution procedures does not allow unraveling the information on band gaps in semiconductors. They recommended the use of an analytical function derived from the natural energy spread of the field-emission tip (260) convoluted by a Gaussian function, and the point-spread function of the detector.

In materials with a band gap above the valence band, the zero-loss peak is followed by a narrow range with zero intensity (assuming that no states are present in the gap region). Unfortunately this range is often not visible due to the width of the zero-loss peak or the poor point spread function of the EELS detector. Despite this difficulty, several groups have attempted to analyze the band-gap region (222, 256, 259). Recent technological developments, including electron monochromators, will facilitate the study of the band-gap region considerably,

even with narrow-gap semiconductors. In Equation 5 the JDOS is proportional to $(E\text{-}E_g)^{0.5}$, where E_g is the band gap. The matrix element is constant for direct band gaps and proportional to $(E\text{-}E_g)$ for indirect band gaps. Therefore, the imaginary part of the energy-loss function is proportional to $(E\text{-}E_g)^n$ with $n = 0.5$ in the case of direct band gaps and $n = 1.5$ for indirect band gaps (222). Thus, using EELS, the nature of the band gap can be determined. This was done in (222) for MgO, diamond, h-BN, c-BN, GaAs, and ZnO, and by Alexandrou et al. (261) for carbon (amorphous, tetrahedral amorphous, and C_{60}).

In Equation 4 it was shown that the energy-loss spectrum can be described by $\mathrm{Im}\{-1/\varepsilon E\}$. This expression, which can also be written as $\varepsilon_2/({\varepsilon_1}^2 + {\varepsilon_2}^2)$, has maxima if $\varepsilon_1 = 0$ and ε_2 is small. These maxima correspond to plasmons, which are collective oscillations of free electrons in a metal or bound valence electrons, e.g., in semiconductors. The plasmon energy E_p is a material property (for a compilation, see 17). In the case of free electron oscillations, ${E_p}^2 = (\hbar^2 ne^2/4\pi^2 m)$, where n is the free electron density. A shift of the plasmon energy appears if bound electron oscillations are relevant (262) or if there are absorption edges by interband transitions close to the plasmon peak (158, 263). Recently it was demonstrated that by acquiring energy-filtered series across the plasmon peak, the peak position can be determined for each pixel image with an accuracy of 0.05 eV (264) at a spatial resolution of about 2 nm. This is shown for a Si-B-C-N ceramic material in Figure 22 where Si_3N_4 grains, SiC grains, and the surrounding matrix can be clearly distinguished by their color-coded plasmon peak energies.

Edge Loss

ANISOTROPIC MATERIALS As mentioned previously, the inelastic electron scattering process does not probe the whole solid angle but is concentrated to a certain angular range of the scattering vector q, which depends on energy loss. Hence, it is possible to obtain EEL spectra with different directions of momentum transfer. This is of particular interest for the study of materials with anisotropic electronic structure. According to Equation 3 the scattering vector enters into the ELNES as a scalar product with the electron coordinate r_j. Thus the ELNES is the projection of the matrix element onto the scattering vector and therefore the material anisotropy is also reflected in the ELNES. This effect is particularly pronounced in graphite (47, 48, 265) or BN (45, 266), which leads to a dependence of the π^* and σ^* peak intensities, e.g., of the C-K edge, on the size of the collection and convergence apertures (Figure 23). The relative intensities of these two peaks is of interest because it allows the determination of the amount of sp^3 bonding in a material. In a number of articles conditions were discussed under which the mentioned dependencies vanish. Berger et al. (271) obtained an sp^2 reference spectrum from polycrystalline graphite by illuminating a large area in order to average out the orientation effect. Browning et al. (267) calculated this averaging effect and suggested using these values because this would not require the illumination of large areas,

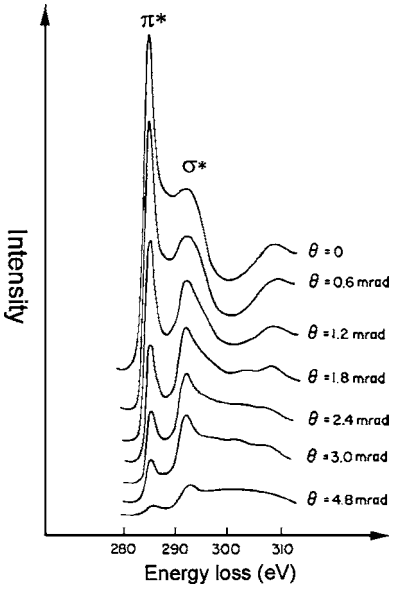

Figure 23 Carbon K edge for different scattering angles of the incident electrons. The relative intensities of the π^* and σ^* peaks change owing to the anisotropic electronic structure of graphite. Reprinted with permission from Leapman et al. (47).

thus making high spatial resolution studies possible. Some authors (268, 269) reported the so-called "magic angle" for the convergence and collector angles, for which the dependence of relative peak heights with specimen orientation vanishes. Values of two and four times the characteristic angle for inelastic scattering, $\bar{\theta}_E$, were proposed. Recently Hébert et al. (270) pointed out that $2\bar{\theta}_E$ is correct and that the apparent discrepancy was due to the fact that inelastic cross sections were not calculated relativistically. Further studies on the determination of the π^*/σ^* ratio can be found in References 271–278. Mapping of the π^*/σ^* ratio was done by both STEM techniques (279) and EFTEM (165, 280).

BORON The detection limit of B in a carbon matrix was shown to be 0.2 at% (281). Experimental studies of BN were performed by Schmid using EELS (282) and Moscovici et al. using X-ray absorption near edge structure (XANES) (283). The B-K edge of hexagonal BN (h-BN) is dominated by a strong π^* peak at 190 eV energy loss. This peak disappears if the momentum transfer $\boldsymbol{q}$ to the excited electron is perpendicular to the *c*-axis, showing that it is entirely due to $2p_z$-type orbitals. The σ^* peak at 198 eV is mostly due to 2s and $2p_{x,y}$ orbitals. Although a dipole transition into s states is forbidden for the B-K edge, such transitions contribute to the edge intensity due to strong 2s–2p hybridization. Further smaller peaks at higher energy losses can be correlated with transitions into 3s and 3p orbitals (284). The core hole effect strongly influences peak intensities. The N-K edge also shows two main peaks at 400 and 408 eV, which are similarly related to N $2p_z$ and $2p_{x,y}$ orbitals, as in the case of the B-K edge. The peaks are broader, which has not been explained yet. The B-K ELNES of cubic BN (c-BN) and wurtzite

BN (w-BN) shows a broad peak centered around 196 eV, which results from σ^* interactions. This peak is followed by small features at about 204 and 213 eV, the latter originating from B-3s and -3p contributions (284). Schmid (282) pointed out that the only difference between c-BN and w-BN is the presence of a low-energy shoulder at the 213 eV peak in the case of w-BN. Terauchi et al. (285) compared low-loss spectra of h-BN with those of BN nanotubes. They found distinct differences in the energy of interband transitions and plasmons.

CARBON The C-K edge in materials formed from elemental C shows several features (Figure 24). The π^* peak at 284.5 eV is due to transitions from the 1s to the antibonding $2p\pi^*$ state. This peak occurs only if unsaturated π bonds are present in the material, as e.g., in graphite and amorphous carbon. At 290 eV, transitions to the antibonding σ^* state form a small peak. A peak appearing between π^* and σ^* was found by Fischer et al. (286) and assigned to interlayer electronic states.

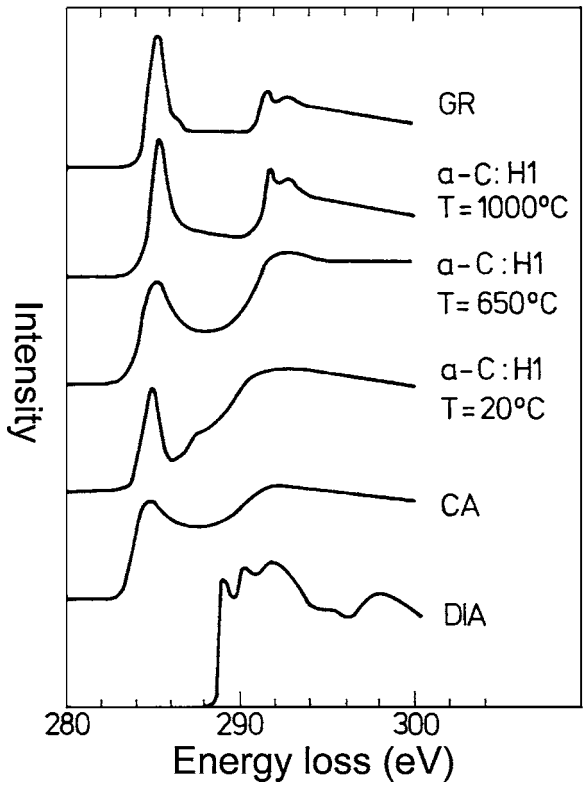

Figure 24 Carbon K edge of graphite (GR), evaporated amorphous carbon before (CA) and after (a-C) heat treatments, and diamond (DIA). Reprinted with permission from Fink et al. (287).

Fink et al. (287) assign a similar peak in this region to the presence of hydrogen, thus forming C:H bonds. In diamond, no π^* peak is present because all C atoms are tetrahedrally coordinated. The absorption starts at 289.1 eV with a sharp 1s core excitonic peak.

In the low-loss regime, the oscillations of π electrons occur at a plasmon energy of 5–6 eV, whereas a combined oscillation of π and σ electrons occurs at about 23 eV. From the $(\pi + \sigma)$ plasmon energy, the valence electron density and thus the atomic density can be determined, but the anisotropy of the material, which can also shift plasmon peaks, should be considered (288).

There are several features in EEL spectra of carbon nanotubes that differ from those of bulk carbon materials. Menon & Yuan (289) found that the π^* peak is more pronounced if the electron beam passes the tube near the surface instead of near the center, which can be understood from the anisotropy of the material (see above). The σ^* peak disappears with increasing curvature of graphene planes (290). In multiwalled nanotubes the $(\pi + \sigma)$ plasmon energy is similar to that in graphite, whereas it is considerably lower in single-walled nanotubes (291–293). In contrast to graphite, C nanotubes exhibit π-to-π^* interband transitions between 1 and 3 eV (294–297). Kociak et al. (298) reported on surface plasmon modes in carbon nanotubes, excited with the electron beam remote from the tube surface. They found two modes at 12–13 eV and 17–18 eV energy loss, and assigned these losses to in-plane and out-of-plane components of the dielectric tensor. Suenaga et al. (299) found that in nanotubes composed of B, C, and N, the individual layers are composed of either C or BN, with C forming the outermost and innermost layers.

Elementary excitations in C_{60} molecules studied by high-resolution EELS are discussed by Lucas et al. (300). Both in the low-loss regime and between the π^* and the σ^* peaks in the C-K edge, C_{60} molecules show distinct peaks not observed in graphite. For larger sphere diameters, as in "carbon onions," the electronic structure resembles that of graphite (301).

In thin films of diamond-like carbon, Yan et al. (165) showed that the near-surface regions exhibited a higher sp^2 bonding than the film interior.

POLYMERS AND BIOLOGICAL MATERIALS Apart from C, these materials also contain other elements, e.g., H and O. The bonding of C with these elements leads to additional features in the ELNES. C–H bonds and C=O bonds (299 eV) lead to peaks close to the π^* peak (287). A mapping of C–C- and C–O-bonds by energy-filtered series was shown by Martin et al. (302).

A main issue in the study of polymers is radiation damage induced by the incident electrons. In the case of PET (polyethylene terephthalate), a critical dose of 10^3 cm^{-2} was found (303, 304), which is at the lower limit for the study of the ELNES of core-loss edges. A factor of about 10 can be gained by cooling the specimen to liquid nitrogen temperature (305).

In polymers the O-K edge displays peaks at 531.5 eV (π^* transition), 534.6 eV, and 541.6 eV (σ^* transitions), all originating from O=C bonds (304).

MAGNESIUM OXIDE Lindner et al. (306) compared experimental Mg-L and O-K spectra with multiple-scattering calculations and concluded that the inclusion of the core hole effect is particularly important for the K edge. Using first-principles molecular orbital calculations for Mg-K, Mg-L, and O-K edges, Mizoguchi et al. (183) found a good correspondence with experimental ELNES studies only after taking into account the effect of the core hole. They assigned spectral features in the Mg spectra to Mg^*-Mg interactions, those in the O-K edge to Mg-Mg and Mg-O^* interactions (Mg^* and O^* denote the excited atoms with core holes). Using the mixed-basis pseudopotential approach, Elsässer & Köstlmeier (197) found a good validity of the $Z + 1$ approximation for the O-K and Mg-L_1 edges, whereas for the Mg-$L_{2,3}$ edge the correlation with experimental data is less satisfactory. According to Köstlmeier & Elsässer (193) the peaks in the O-K ELNES can be understood simply by the presence of the strongly scattering oxygen ions. Therefore, the O-K ELNES can generally be used as a fingerprint for the structure of the anion sublattice in metal oxides. The influence of the cation sublattice is comparatively weak.

ALUMINUM AND ITS COMPOUNDS Figure 25 shows the Al-$L_{2,3}$ edge for different Al compounds. Bouchet & Colliex (307) identified 10 peaks a–j between 77 and 86 eV. Peaks at higher energy losses are from the transitions to 3d states, between 85 and 95 eV to 3p states (dipole-forbidden) (308), and the peaks near threshold are transitions to 3s states (193), which are related to the formation of core excitons induced by the core hole (194). Owing to the screening of a core hole, no such sharp features are observed in metallic Al near threshold. According to Bouchet & Colliex (307) peaks g–j are related with the medium-range order around the Al atoms. The positions of peaks a–d can be used for an identification of Al compounds. Nufer et al. (43) pointed out that under channeling conditions (i.e., in a zone axis orientation) dipole-forbidden, but symmetry-allowed, transitions can occur. Nufer et al. (309) also reported on calculations of core-loss edges in α-Al_2O_3 for the Al-K and -L_1 edges. For both edges, transitions to the 2p states occur, implying that they have a similar shape. However, this is not the case because of different core holes (1s for the K edge, 2s for the L edge). The authors (309) find a good match with experimental data in the $Z + 1$ approximation for the Al-K edge, whereas for the Al-L_1 edge better results are obtained without this approximation. It is argued that the core hole effect is stronger the more localized is the core hole (i.e., for the 1s core hole) because in such cases, the perturbation of the system is particularly strong.

A simple way to distinguish metallic Al from Al compounds is the sharp plasmon peak of metallic Al at 15 eV. Figure 26 shows an energy-filtered plasmon image of an α-Al_2O_3 specimen after electron irradiation at high temperatures. Bright circular areas clearly display the metallic regions.

SILICON In a number of articles Batson (e.g., 310, 311) used spatially resolved EELS to measure the electronic structure of the band gap in Si-based semiconductor

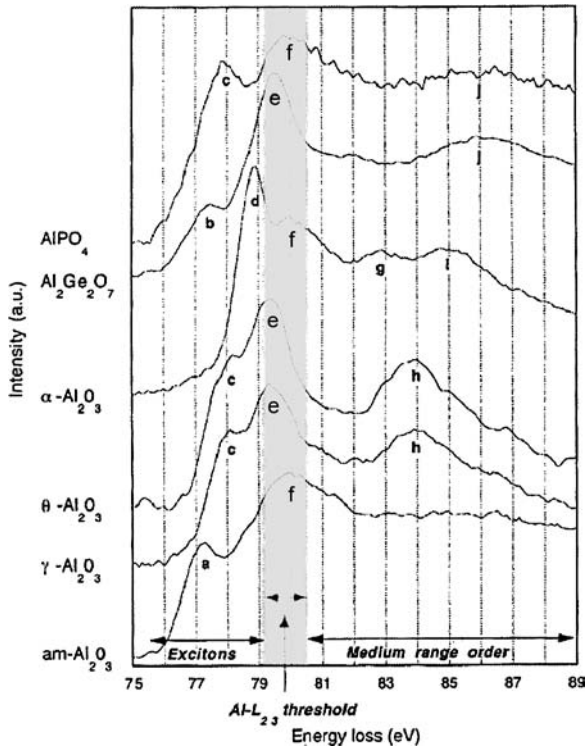

Figure 25 Al-L edge in different Al compounds. The peaks a–j are discussed in the text. Reprinted with permission from Bouchet et al. (307).

devices. After deconvolution with the low-loss signal and subtraction of transitions from the $2p_{1/2}$ ground state (the L_2 edge), the remaining Si-L_3 edge is fitted to the band structure. In SiGe alloys Batson was able to correlate strain with a change of the shape of the Si-L edge. In a dissociated 60° dislocation in SiGe he found distinct differences between the Si-L ELNES in the partial dislocation cores and the intrinsic stacking fault in between the cores (312). He ascribed these differences to optically active electronic states in the band gap in the partial dislocation cores.

Duscher et al. (313) show that the Si-L edge is influenced by the core hole effect not only in oxides but also in pure Si.

TRANSITION METALS Transition metals with unoccupied d-states show two sharp peaks (white lines) in the $L_{2,3}$ absorption edge originating from transitions from $2p_{1/2}$ and $2p_{3/2}$ initial states. These two states have different energies because of the coupling between the spin and angular magnetic moments of the 2p core hole. With increasing Z, this energy difference becomes larger. The width of the white

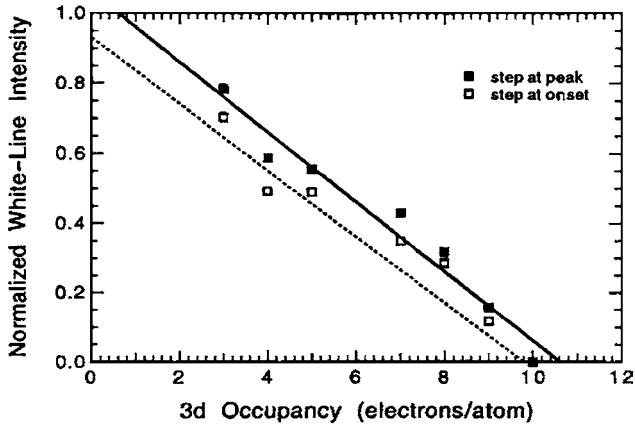

Figure 27 White line intensity for transition metals with different occupancy of 3d states. Reprinted with permission from Pearson et al. (315).

lines decreases with Z owing to the steady filling of the 3d band, and it is narrower for oxides than it is for the metal. For most of the transition metals (except Cu) the edge onset is shifted toward higher energy by oxidation. The total intensity of the white lines compared with the continuum following the edge is directly related to the d-band occupancy (314, 316) (Figure 27). The intensity ratio of the white lines is not equal to the simple statistical ratio of 2:1 expected from the $2j + 1$ degeneracy ($j = \ell + s$ with spin s and orbital momentum ℓ) of the two initial states (317, 318). Rather, it is a function of the d-band occupancy and thus of the local magnetic moment and the oxidation state of the atom (318–320). An improved analysis of L_2/L_3 ratios was shown by Pease et al. (321). Murakami et al. (322) detected a change of the d-band occupancy in a TiNiFe alloy after the martensitic transformation.

In transition metal (TM) oxides the oxygen 2p states hybridize with the TM s-, p-, and, in particular, d-states. For this reason the ELNES of the O-K edges show features that resemble the $L_{2,3}$ edges of the TMs, as e.g., peaks from the t_{2g}- and e_g-orbitals (323–326).

The sharp white lines make the detection of transition metals relatively easy. It was shown that 100 ppm can be detected (327).

The magnetic-dichroic effect can be used to characterize magnetic anisotropy and is normally performed using X-ray absorption spectroscopy (328, 329). The circular magnetic dichroism (difference in absorption of right- and left-circularly polarized photons) has been demonstrated until now by using X-rays, which allows determination of the magnitude and direction of spin and orbital magnetic moments. See Reference 330 for a discussion of possible EELS experiments. Schattschneider et al. (331) point out that it is the chirality of the $\Delta m = \pm 1$ transition that is measured in EELS because circular polarization is not possible

for electrons. Linear magnetic dichroism (difference in absorption for momentum transfer parallel and perpendicular to the magnetization) also can be detected by EELS (49, 289, 332, 333). It basically leads to a variation of the $L_{2,3}$ intensities by changing the orientation of the specimen with respect to the electron beam. Owing to the hybridization of O and TM orbitals, the magnetic-dichroic effect is even visible in the O-K edge (333). The linear dichroism measures the charge anisotropy of the valence states.

Murakami et al. (334) have reported a broad peak about 30–40 eV above the O-K edge of transition metal oxides and perovskites and ascribe it to a resonance effect of the ejected core electrons. They found a linear dependence of the energy position above the edge onset and $1/R^2$, where R denotes the distance to the next O atom. Thus the energy position of this peak allows a simple measure of the O–O separation.

Titanium oxides The shape of the Ti-$L_{2,3}$ edge is dominated by four peaks a–d (Figure 28). These arise from the dipole-allowed excitation of electrons from the inner $2p_{3/2}$ (L_3 edge, peaks a and b) and $2p_{1/2}$ (L_2 edge, peaks c and d) to the narrow unoccupied 3d band, resulting in two white lines. Both white lines are doubled by the action of the Coulomb field imposed by the surrounding O atoms (ligand-field splitting). A perfect octahedral ligand field causes the five degenerate

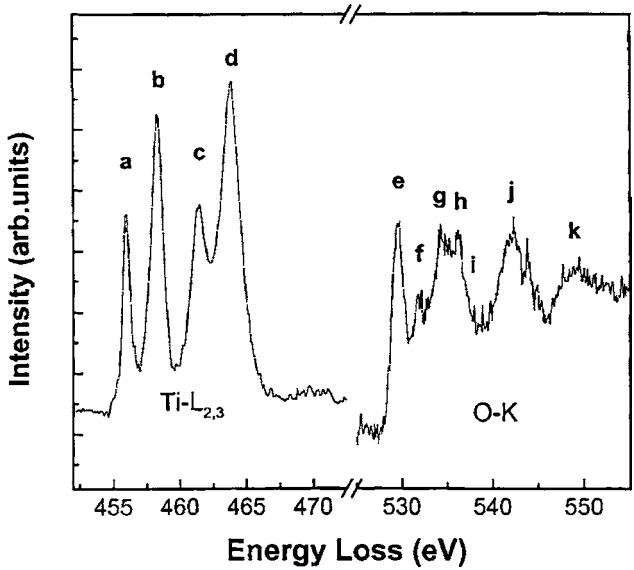

Figure 28 Ti-L and O-K edges in $SrTiO_3$. The peaks a–k are discussed in the text. Reprinted figure with permission from Zhang et al. (379).

d-states in the conduction band to split into twofold e_g orbitals that are directed at the ligands (corresponding to peaks b and d), and the threefold t_{2g} orbitals that are directed between the ligands (corresponding to peaks a and c) (335). Whereas a deviation from the octahedral symmetry will create new states in the conduction band, a change of the magnitude of the crystal field affects the energetic position and relative intensities of the transitions (336). However, these changes are generally weak and are often not observable as additional peaks. Rather, a broadening of the white lines or a change of the peak separations is detected. The e_g:t_{2g} intensity ratio increases and their separation decreases by a reduction of the crystal field (337). A chemical shift of 1.4 eV toward lower energies is observed in the Ti metal compared with that in TiO_2 (317). The same authors report a L_3/L_2 ratio of 0.8 for both Ti and TiO_2. The deviation from the statistical ratio of 2:1 (obtained from the $2j + 1$ degeneracy of the initial states) is mainly due to the excitation process, which leaves a core hole in one of the 2p states and an excited electron in the 3d band (319). Taking this into account, Ogasawara et al. (338) recently succeeded in approximately reproducing the experimental ratio by nonempirical ab initio cluster calculations. By ab initio calculations, van Benthem (339) has shown that due to the influence of the core hole, the measured white line separations deviate from the values in the electronic ground state.

The O-K edge originates from transitions from the O 1s-shell to unoccupied 2p states and would thus not be visible in a purely ionic compound where all 2p states are filled. In transition metal (TM) oxide compounds, the density of unoccupied oxygen 2p states is significantly modified by the strong hybridization with metal 3d states. The O-K edge in bulk $SrTiO_3$ is shown in Figure 28. Seven peaks labeled e–k are visible. It is generally accepted that peaks e and f are correlated with the interaction of the oxygen atom with the two nearest-neighbor Ti atoms; e can be correlated with the Ti t_{2g} orbital and f with the Ti e_g orbital. Brydson et al. (340) made the point that a large e/f intensity ratio is typical for a linear chain of Ti-O–Ti tight bonds, as is true for $SrTiO_3$. Any distortion of this linearity increases the intensity of f. For tetrahedral coordination, both peaks have similar intensities (340, 341). By comparing different TM oxides, de Groot et al. (325) concluded that the total intensity of e and f is inversely proportional to the d-band filling and thus to the covalency of the Ti–O bonding. The weakness of peak f has also been attributed to its broadening by the strong e_g-e_g interaction (341, 342). It is argued that this interaction even leads to a splitting of the e_g band leading to the separate peak g. From this, Tanaka et al. (342) conclude that the e_g intensity and the separation of f and g should sensitively depend on the Ti–O bonding angle. Peaks h and i most probably are related to the Sr–O bonding (340–342). There is no unambiguous assignment of peak j to structural features. Whereas de Groot et al. (341) assumes this peak to originate from the Sr 4p band, Tanaka assigns it to the Ti 4s band. Finally, peak k is generally assumed to be related to the Ti 4p band. Wallis & Browning (343) and Browning et al. (344) performed multiple scattering calculations using clusters extracted from the perovskite structure. By removing atoms from the cluster they assigned spectral features to structural features. Apart

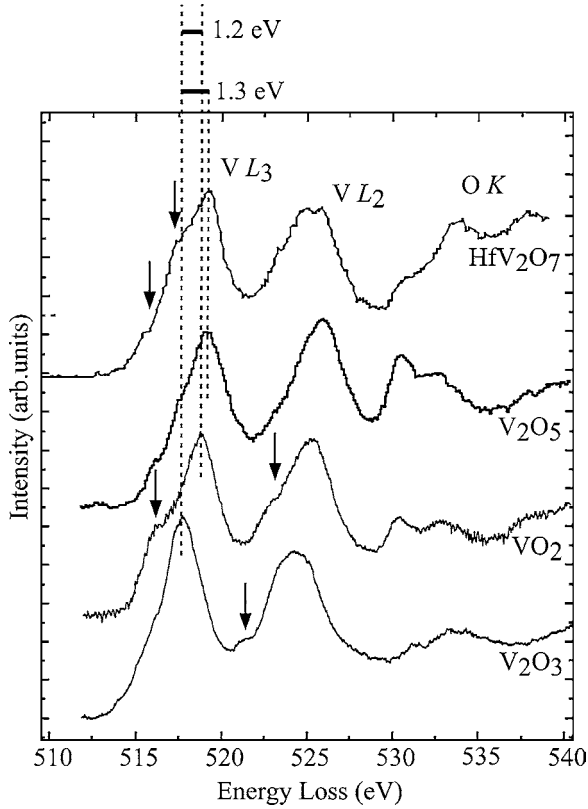

Figure 29 V-L edge in various vanadium oxides. Reprinted with permission from Gloter et al. (346).

from peaks e and f, they assigned the other peaks mainly to the scattering from the surrounding oxygen atoms.

Vanadium In Figure 29 the V-$L_{2,3}$ edge is shown for different vanadium oxides (345, 346). There is a gradual decrease of the L_3/L_2 white line ratio with increasing oxidation state. This is accompanied by an increase of the oxygen-K edge intensity at the onset of the edge (530 eV).

Manganese The Mn-$L_{2,3}$ and O-K ELNES were measured by Kurata & Colliex (347) for oxides with five different nominal oxidation states of the Mn ions. The results are shown in Figure 30. The O-K edge is composed of features a–d. Peak a is attributed to transitions to O 2p states hybridized with Mn 3p states. The structure of this peak varies significantly in the different oxides. The Mn-L edge shows two prominent white lines. With increasing oxidation state the L_3 peak shifts toward higher energy and the L_2/L_3 intensity ratio increases.

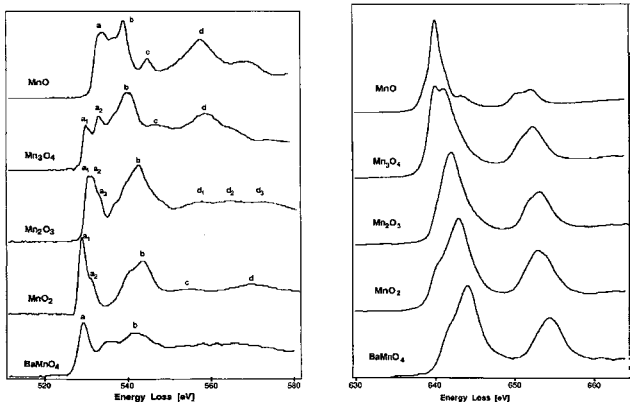

Figure 30 O-K and Mn-L edges in different manganese oxides. Reprinted with permission from Colliex (347).

Iron The structure of the O-K and Fe-$L_{2,3}$ edges of various Fe oxides was discussed by Colliex et al. (348). Similar to other transition metal oxides, it was found that the oxygen-K edge is sensitive to the local bonding and coordination, and the Fe-L edge is strongly influenced by electron Coulomb and exchange interactions between the 2p core hole and 3d electrons. The latter was confirmed by Kurata et al. (349) using ab initio cluster calculations. In addition, a high-spin state of α-Fe_2O_3 (parallel spins of the 5d electrons, $S = 5/2$) had to be assumed. The crystal field from the oxygen ligands causes a shoulder at the onset of the L_3 white line. The L_3/L_2 ratio increases with decreasing crystal field owing to a transition from a high-spin to a low-spin state (Figure 31) (319, 320, 347, 350). An overview of Fe $L_{2,3}$ edge shapes in many Fe-containing minerals is shown by van Aken & Liebscher (351). From a detailed analysis they determined the relative content of Fe^{3+} ions with an absolute error of ± 0.02. This is possible because the L_3 white line of Fe^{2+} is located at 707.8 eV, whereas it is shifted to 709.5 eV in the case of Fe^{3+}.

Copper Owing to the filled d-states, metallic copper does not show white lines in the $L_{2,3}$ edge. However, in the presence of oxidizing elements, charge can be removed from the Cu atoms, which makes the white lines appear. White line intensity can be used to determine the oxidation state (314, 315, 317). Cu oxide spectra of different compounds (different oxidation states) are shown in Figure 32.

Zinc From the shape of the Zn-L edge, Mizoguchi et al. (354) were able to distinguish different oxygen coordination numbers of Zn atoms.

Intermetallic alloys Muller & Silcox (352) studied the Ni-L and the Al-L edges in $Ni_{1-x}Al_x$, both experimentally and by theory. For the Ni-L edge they found a

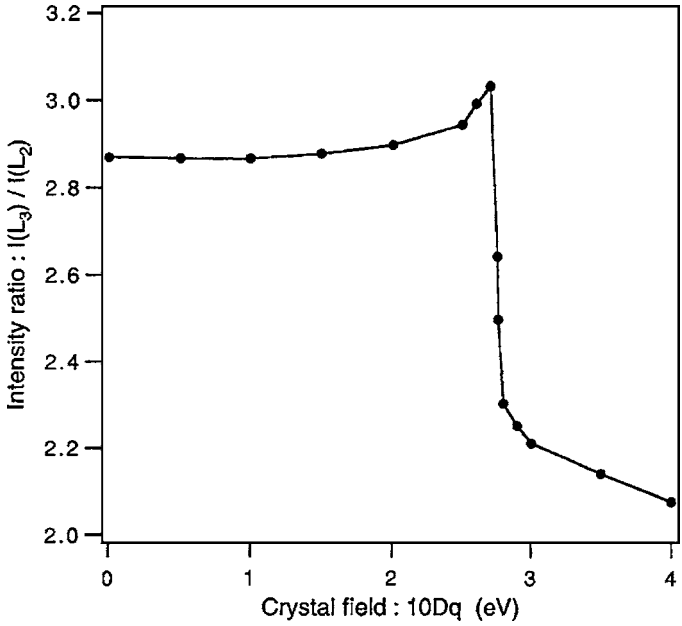

Figure 31 Intensity ratio of Fe L_3 and L_2 white lines as a function of the magnitude of the crystal field acting on the Fe atom by surrounding oxygen ions. Reprinted with permission from Kurata et al. (349).

steady decrease of the L_3 white line with increasing Al content (Figure 33) because of hybridization of Al 2s with Ni 3d orbitals. The intensity close to the onset of the Al-L edge was found to decrease with increasing Ni content. This was attributed to a pseudogap, also originating from s–d hybridization. Changes of the Ni-$L_{2,3}$ edge by the formation of Ni-based intermetallic compounds were measured by Potapov et al. (353).

GALLIUM NITRIDE The N-K edge shows several well pronounced peaks (Figure 34) (161). Their positions are almost the same in c-GaN and h-GaN because in both systems the N coordination is tetrahedral. Lazar et al. (161) also studied the low-loss regime of GaN and detected the band gap, as well as several interband transitions. They were able to fit the intensity above the band gap to that expected from a direct semiconductor.

The variation of the N-K and Al-K edges with N content in $Al_xGa_{1-x}N$ is shown in Figure 35 (355). The strong variation of the N-K edge is attributed to the fact that, through a variation of x, the composition of nearest-neighbor atoms of N changes. For Al atoms only the second-nearest neighbors change with x. The slight peak shifts of the Al-K edge are attributed to an increase in interatomic distances.

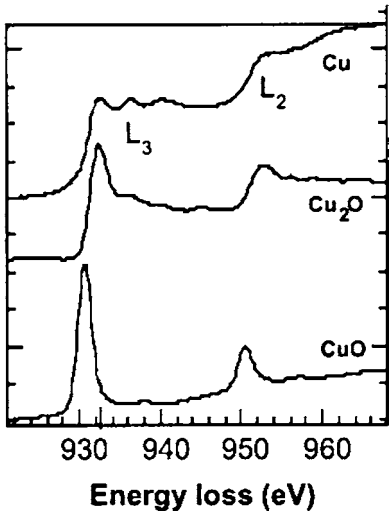

Figure 32 Cu-L edge in Cu and two Cu oxides. Reprinted with permission from Imhoff et al. (47).

RARE-EARTH ELEMENTS In lanthanides the $M_{4,5}$ edge is dominated by white lines originating from transitions $3d_{3/2} \rightarrow 4f_{5/2}$ (M_4) and $3d_{5/2} \rightarrow 4f_{7/2}$ (M_5). The M_4:M_5 intensity ratio was found to decrease with increasing 4f orbital occupancy (Figure 36) (358) and could therefore be used to determine the oxidation state (356).

Buck & Fortner (357) reported the detection of less than 200 ppm of U and Pt in nuclear waste glass by analyzing the $M_{4,5}$-edges at about 3.7 keV. A similar

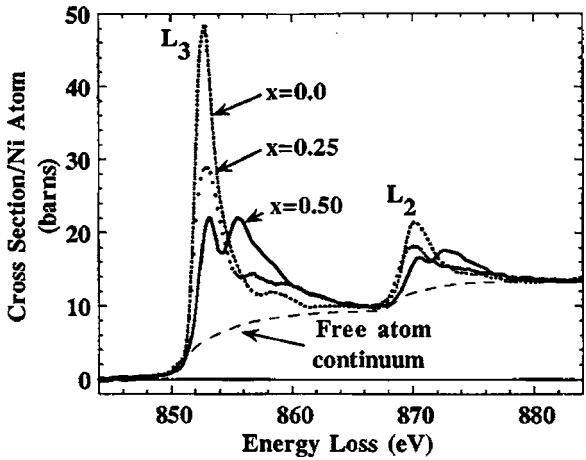

Figure 33 Ni-L edge in $Ni_{1-x}Al_x$ for different values of x. Reprinted with permission from Muller & Silcox (352).

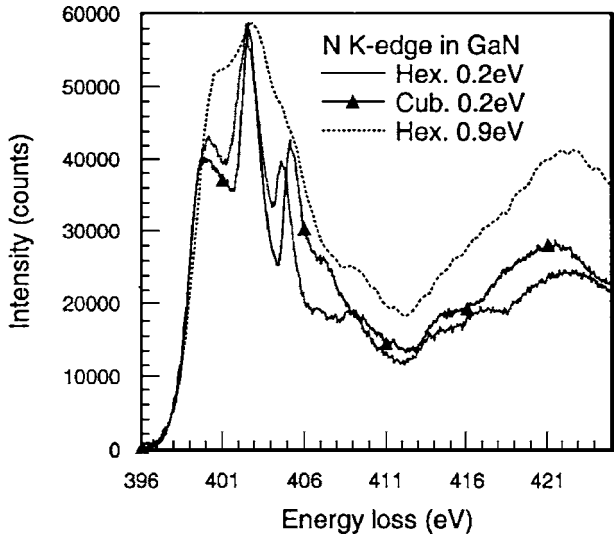

Figure 34 N-K edge in hexagonal and cubic GaN. The spectra with 0.2 eV energy resolution were obtained using an electron monochromator. Reprinted with permission from Lazar et al. (161).

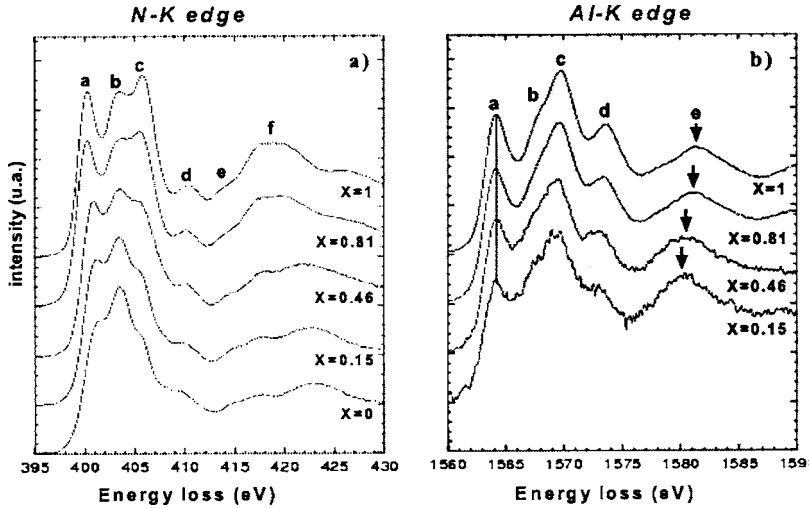

Figure 35 N-K and Al-K edges in $Al_xGa_{1-x}N$ for different values of x. Reprinted with permission from Radtke et al. (355).

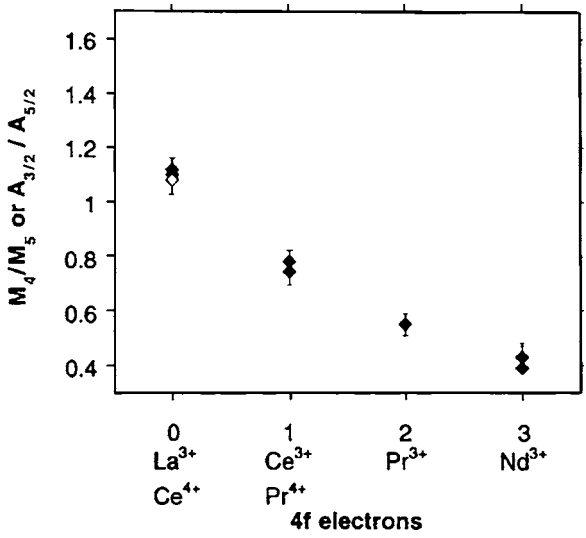

Figure 36 Intensity ratio of M_4 and M_5 white lines for different lanthanides. Reprinted with permission from Fortner et al. (358).

trend of the M_4:M_5 intensity ratio with 5f orbital occupancy was found as in the lanthanides (Figure 37) (358).

SPINELS Spinels are compounds with the composition AB_2O_4, where A and B are transition metals and O is oxygen. Depending on the site occupancy of the metal atoms, normal and inverse spinels are distinguished. In normal spinels all octahedral sites are occupied by B^{3+} ions, whereas in the inverse spinel these sites are occupied by A^{2+} and B^{3+} ions in equal proportions.

The O-K edge was studied for a series of normal spinels with $B{=}Cr^{3+}$ (chromites) by Docherty et al. (359) both experimentally (Figure 38) and by multiple scattering simulation using the FEFF8 code. They identified six peaks denoted by A, B, C, D (with a shoulder, denoted as D*), and E. From the fact that peaks A–C are not present in aluminate spinels it was concluded that these peaks are related to the vacant d-states of the Cr ions because these d-states hybridize with O 2p-states. The intensity of peak C changes with the nature of the A ion. No marked changes were observed in a variation of the A ions, both in aluminates and chromites. The FEFF calculations showed good correspondence with experimental spectra for the Mg aluminate but poor agreement for all chromates. It was suggested that this is due to the influence of magnetic interactions.

The intensity of the low-energy shoulder in the aluminates (left side of Figure 38) was found to be related to the degree of inversion, being particularly

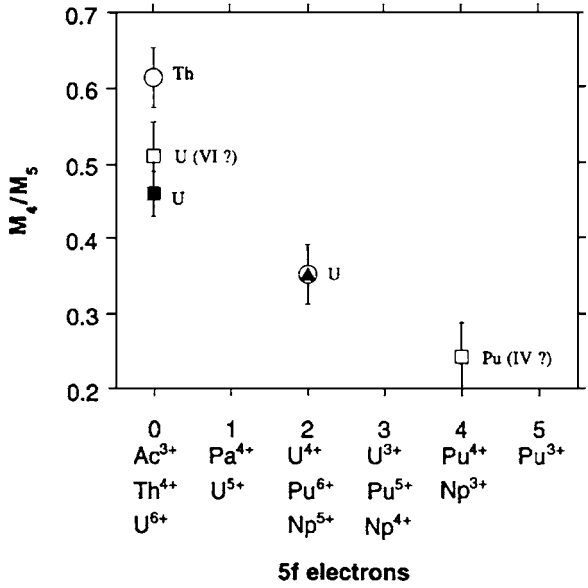

Figure 37 Intensity ratio of M_4 and M_5 white lines for different actinides. Reprinted with permission from Fortner et al. (358).

strong at full inversion (193, 360). Thus this shoulder is related to the tetrahedral nearest-neighbor coordination (361, 362).

PEROVSKITES (SEE ALSO Ti-OXIDES) Perovskites are oxides with composition ABO_3, where A and B are metal ions. Using the combination of atom-column-resolved *Z*-contrast and EELS, Klie et al. (363) studied different perovskites with [A = (La,Sr)/B = (Fe,Cr); A = Sr/B = Co; A = Sr/B = Ti]. Using EEL spectra acquired from different atom columns, they determined the valency of the transition metals and from this deduced the number of oxygen vacancies. In the case of $SrTiO_3$, they showed evidence for the accumulation of oxygen vacancies near a grain boundary.

HIGH-TEMPERATURE SUPERCONDUCTORS A prepeak of the O-K edge at about 529 eV in $La_{2-x}Sr_xCuO_{4-\delta}$ (364), $YBa_2Cu_3O_{7-\delta}$ (365), and $Bi_2Sr_2Ca_{1-x}Y_xCu_2O_8$ (366) was reported for p-doped material. This peak indicates the presence of holes on O sites. From the orientation dependence of the shape of the O-K edge, it was possible to determine the symmetry of these hole states (367–369).

METAL–CERAMIC INTERFACES Owing to the different interatomic bonds in metals and ceramics (covalent and/or ionic), atoms close to interfaces between these

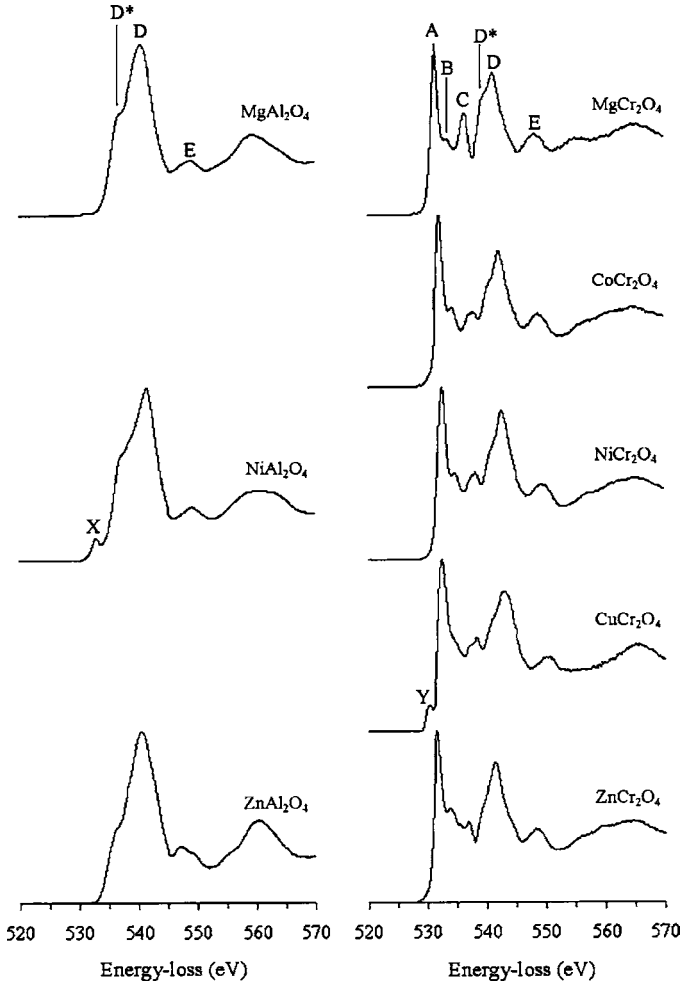

Figure 38 O-K edges of various Al- and Cr-spinels. Reprinted with permission from Docherty et al. (359).

material systems may differ in oxidation state and in coordination from the parent crystals or may even form new phases along the interfaces. Unfortunately, at present it is not possible to make predictions about the interfacial electronic and atomic structure from the basic properties of the materials. Experimentally, the most frequently used analytical technique in this field is the spatial difference technique as well as EELS line scans across the interface.

MgO–Cu Using the spatial difference method Imhoff et al. (370) found a CuO-like Cu-$L_{2,3}$ ELNES indicating transfer of charge from Cu to MgO. From EELS

line scan data, Muller et al. (371) concluded that metal-induced gap states exist in the MgO. These originate from the Cu wave function extending into the band gap of MgO.

Cu–α-Al_2O_3 Dehm et al. (372) and Scheu et al. (373) studied Cu films deposited on the basal plane of sapphire by molecular beam epitaxy (MBE) at 473 K. The spatial difference spectrum showed Cu_2O-type bonding, i.e., the Cu atoms are reduced to the Cu^{1+} state by charge transfer to the neighboring O atoms. MBE films grown at 800°C on the $(11\bar{2}0)$ plane show a mixed Al-Cu interface plane facing an oxygen layer in the sapphire substrate (374).

Nb–α-Al_2O_3 From a change of the interface-specific ELNES of the Al-L edge, Bruley et al. (375) concluded that diffusion-bonded material showed Al–Nb bonding. From the absence of this signal in MBE-grown interfaces, Nb–O bonding was deduced.

Al–α-Al_2O_3 Scheu et al. (376) found changes of both Al-L and O-K edges at the interface between Al and sapphire. Therefore it is concluded that the sapphire is O-terminated.

Cr,Ni/$SrTiO_3$ At interfaces between Ni or Cr and $SrTiO_3$ bonding between metal and oxygen atoms was detected by van Benthem et al. (377).

DISLOCATION CORES The experimental study of the ELNES in dislocation cores is particularly challenging because the dislocation has to be viewed along the dislocation line and thus appears as a one-dimensional defect. Batson (312) studied the electronic structure of dislocations in SiGe (see above). Zhang et al. (378, 379) detected a change of the Ti-L and O-K ELNES and attributed this to a distortion of the TiO_6 octahedra in the dislocation core. This distortion was accompanied by a loss of oxygen in the core region.

Arslan & Browning (380) and Xin et al. (381) obtained N-K ELNES from dislocation cores in GaN. By comparing multiple scattering calculations they concluded that in pure GaN dislocations do not induce states in the band gap.

GRAIN BOUNDARIES As in the study of interfaces, the spatial difference method is particularly powerful for the study of the electronic structure or segregation at grain boundaries (GBs) (see above). Nufer et al. (382) studied the electronic structure at the rhombohedral twin grain boundary in α-Al_2O_3. They found good correspondence between band structure calculations, EELS, and HRTEM results.

Until the 1970s, grain boundary segregation studies were the domain of Auger electron spectroscopy. The first to measure segregation by TEM were Doig & Flewitt (108). The quantitative measure of the GB excess is possible by illuminating a narrow area containing the GB and comparing the EELS or EDXS signal with that of an area remote from the GB. This is basically a spatial difference method.

It can be done most effectively in a STEM. A field-emission electron source is almost mandatory because the relative signal from the GB is higher the smaller the illuminated area. Usually a width of a few nanometers perpendicular to the boundary is used. In thick specimen areas, beam broadening can introduce errors into the analysis. This was taken into consideration by Alber et al. (112). Another approach also applicable in a TEM was described by Walther et al. (383). They measured the signal from the segregated element using different sizes of the focused electron beam. From the interpolation to zero beam size they obtain the GB excess. Using the ζ-factor method (56), Watanabe et al. obtained compositional maps of the Cr-, Ni-, and Mo-segregation at GBs in Fe (383a). A method to measure GB segregation at heterointerfaces was shown by Kooi et al. (384).

With the availability of highly stable microscopes it has become possible to probe the ELNES of almost single-atom columns on the GB or interface. Several examples are shown in (385) and references therein.

CONCLUSIONS

With the advent of new instrumentation (C_s correctors, electron monochromaters, energy filters, CCD detectors) it has now become possible to obtain chemical information with a spatial resolution well below 1 nm and an energy resolution better than 0.2 eV in analytical TEM. This unique combination makes analytical TEM an indispensable technique in materials science. The instrumental achievements have been accompanied by a steady development of data evaluation and interpretation, the aim of which is to extract the utmost information from the available experimental data. Owing to this rapid progress, the present article can at best give a snap-shot of the present state in this exciting field of research.

ACKNOWLEDGMENT

I thank Professor M. Rühle for inspiring me to write this article and for his careful comments. Critical reading of a part of the manuscript by Professor C. Elsässer and Dr. Masashi Watanabe is gratefully acknowledged.

LITERATURE CITED

1. Sorby H. 1887. On the microscopical structure of iron and steel. *J. Iron Steel Inst.* 1:255–88
2. Friedrich W, Knipping P, Laue M. 1912. *Interferenz-Erscheinungen bei Röntgenstrahlen*. Presented at Mathematisch-Physikalische Klasse der königlich bayerischen Akademie der Wissenschaften

3. Davisson C, Germer L. 1927. Diffraction of electrons by a crystal of nickel. *Phys. Rev.* 30:705–40
4. Knoll M, Ruska E. 1932. Das Elektronenmikroskop. *Zeitschrift für Physik* 78:318–39
5. Bollmann W. 1956. Interference effects in the electron microscopy of thin crystal foils. *Phys. Rev.* 103:1588–9
6. Hirsch P, Horne R, Whelan M. 1956. Direct observations of the arrangement and motion of dislocations in aluminium. *Philos. Mag.* 1:677–84
7. Martínez G, Tsuno K. 2004. Design of Wien filters with high resolution. *Ultramicroscopy* 100:105–14
8. Haider M, Rose H, Uhlemann S, Schwan E, Kabius B, Urban K. 1998. A spherical-aberration-corrected 200 kV transmission electron microscope. *Ultramicroscopy* 75:53–60
9. Krivanek OL, Dellby N, Lupini AR. 1999. Towards sub-Å electron beams. *Ultramicroscopy* 78:1–11
10. Rose H. 1990. Outline of a spherically corrected semiaplanatic medium-voltage transmission electron-microscope. *Optik* 85:19–24
11. Rose H. 1999. Prospects for realizing a sub-Å sub-eV resolution EFTEM. *Ultramicroscopy* 78:13–25
12. Haider M, Uhlemann S, Zach J. 2000. Upper limits for the residual aberrations of a high-resolution aberration-corrected STEM. *Ultramicroscopy* 81:163–75
13. Krivanek O, Nellist P, Dellby N, Murfitt M, Szilagyi Z. 2003. Towards sub-0.5 Å electron beams. *Ultramicroscopy* 96:229–37
14. Batson P. 2003. Aberration correction results in the IBM STEM instrument. *Ultramicroscopy* 96:239–49
15. Nellist P, Chisholm M, Dellby N, Krivanek O, Murfitt M, et al. 2004. Direct sub-Angstrom imaging of a crystal lattice. *Science* 305:1741
16. Urban K, Kabius B, Haider N, Rose H. 1999. A way to higher resolution: spherical-aberration correction in a 200 kV transmission electron microscope. *J. Electron Microsc.* 48:821–26
17. Egerton RF. 1996. *Electron Energy-Loss Spectroscopy in the Electron Microscope*. New York/London: Plenum. 485 pp.
18. Crewe A, Isaacson M, Johnson D. 1969. A simple scanning electron microscope. *Rev. Sci. Instrum.* 40:241–46
19. Crewe A, Isaacson M, Johnson D. 1971. High resolution electron spectrometer for use in transmission scanning electron microscopy. *Rev. Sci. Instrum.* 42:411–20
20. Reimer L. 1994. *Energy-Filtering Transmission Electron Microscopy*. Berlin/Heidelberg: Springer
21. Gubbens AJ, Krivanek OL. 1993. Applications of a post-column imaging filter in biology and materials science. *Ultramicroscopy* 51:146–59
22. Krivanek OL, Friedman SL, Gubbens AJ, Kraus B. 1995. An imaging filter for biological applications. *Ultramicroscopy* 59:267–82
23. Uhlemann S, Rose H. 1996. Acceptance of imaging energy filters. *Ultramicroscopy* 63:161–67
24. Wollmann D, Irwin K, Hilton G, Dulcie L, Newbury D, Martinis J. 1997. High-resolution, energy-dispersive microcalorimeter spectrometer for X-ray microanalysis. *J. Microsc.* 188:196–223
25. Newbury D, Wollman D, Irwin K, Hilton G, Martinis J. 1999. Lowering the limit of detection in high spatial resolution electron beam microanalysis with the microcalorimeter energy dispersive X-ray spectrometer. *Ultramicroscopy* 78:73–88
26. Zaluzec N. 2004. *XEDS systems for the next generation analytical electron microscope*. Presented at Microscopy and Microanalysis 2004, Savannah, GA
27. Goldstein J. 2002. *Scanning Electron Microscopy and X-Ray Microanalysis*. The Netherlands: Kluwer

28. Williams DB. 1995. *X-Ray Spectrometry in Electron Beam Instruments*: New York: Plenum
29. Spence J, Tafto J. 1983. ALCHEMI—a new technique for locating atoms in small crystals. *J. Microsc.* 130:147–54
30. Taftø J, Spence JCH. 1982. Atomic site determination using the channeling effect in electron-induced X-ray emission. *Ultramicroscopy* 9:243–47
31. Lenz F. 1954. Zur Streuung mittelschneller Elektronen in kleinste Winkel. *Z. Naturforsch. A* 9:185–204
32. Williams BG, Parkinson GM, Eckhardt CJ, Sparrow JMT. 1981. A new approach to the measurement of the momentum densities in solids using an electron microscope. *Chem. Phys. Lett.* 78:434–38
33. Exner A, Schattschneider P. 1996. Asymmetries in electron Compton profiles of silicon—a coherence effect. *Ultramicroscopy* 65:131–45
34. Egerton R, Wong K. 1995. Some practical consequences of the Lorentzian angular-distribution of inelastic-scattering. *Ultramicroscopy* 59:169–80
35. Bethe H. 1928. Theorie der Beugung von Elektronen an Kristallen. *Ann. Phys.* 4:55–129
36. Inokuti M. 1971. Inelastic collisions of fast charged particles with atoms and molecules—Bethe theory revisited. *Rev. Mod. Phys.* 43:297–347
37. Schattschneider P, Hébert C, Jouffrey B. 2001. Orientation dependence of ionization edges in EELS. *Ultramicroscopy* 86:343–53
38. Nelhiebel M, Luchier N, Schorsch P, Schattschneider P, Jouffrey B. 1999. The mixed dynamic form factor for atomic core-level excitations in interferometric electron-energy-loss experiments. *Philos. Mag. B* 79:941–53
39. Krause M, Oliver J. 1979. Natural width of atomic K-levels and L-levels, K-alpha X-ray-lines and several KLL Auger lines. *J. Phys. Chem. Ref. Data* 8:329–38
40. Fuggle JC, Inglesfield JE. 1992. Introduction. In *Unoccupied Electronic States*, ed. JC Fuggle, JE Inglesfield, pp. 1–23. Berlin: Springer
41. Fuggle J, Alvarado S. 1980. Core-level lifetimes as determined by X-ray photoelectron-spectroscopy measurements. *Phys. Rev. A* 22:1615–24
42. Rehr J, Albers R. 2000. Theoretical approaches to X-ray absorption fine structure. *Rev. Mod. Phys.* 72:621–54
43. Nufer S, Gemming T, Köstlmeier S, Rühle M. 2001. Validity of the dipole-selection rule for the Al-$L_{2,3}$ edge of -Al_2O_3 under channeling conditions. *Ultramicroscopy* 88:253–63
44. Grunes L, Leapman R. 1980. Optically forbidden excitations of the 3s subshell in the 3d transition-metals by inelastic-scattering of fast electrons. *Phys. Rev. B* 22:3778–83
45. Hébert-Souche C, Louf P-H, Blaha P, Nelhiebel M, Luitz J, et al. 2000. The orientation-dependent simulation of ELNES. *Ultramicroscopy* 83:9–16
46. Essex D, Nellist P, Whelan C. 1999. Limitations of the dipole approximation in calculations for the scanning transmission electron microscope. *Ultramicroscopy* 80:183–92
47. Leapman R, Fejes P, Silcox J. 1983. Orientation dependence of core edges from anisotropic materials determined by inelastic-scattering of fast electrons. *Phys. Rev. B* 28:2361–73
48. Botton G, Boothroyd CB, Stobbs WM. 1995. Momentum dependent energy loss near edge structures using a CTEM: the reliability of the methods available. *Ultramicroscopy* 59:93–107
49. Browning N, Yuan J, Brown L. 1991. Real-space determination of anisotropic electronic-structure by electron-energy loss spectroscopy. *Ultramicroscopy* 38: 291–98
50. Midgley PA. 1999. A simple new method to obtain high angular resolution ω–q patterns. *Ultramicroscopy* 76:91–96

51. Spence J, Reese G. 1986. Pendellösung radiation and coherent bremsstrahlung. *Acta Crystallogr. A* 42:577–85
52. Sigle W, Carstanjen H. 1992. Observation of coherent bremsstrahlung in quasicrystalline Al-Cu-Co-Si. *Philos. Mag. B* 66:533–40
53. Anderson I, Bentley J, Carter C. 1997. Secondary fluorescence correction formulae for X-ray microanalysis. 1. Parallel-sided thin foil, wedge, and bulk specimens. *Ultramicroscopy* 68:77–94
54. Goldstein J, Costley J, Lorimer G, Reed S. 1977. *Quantitative X-ray analysis in the electron microscope*. Presented at 10th Annu. Scanning Electron Microscopy Symp. Chicago
55. Watanabe M, Horita Z, Nemoto M. 1996. Absorption correction and thickness determination using the ζ factor in quantitative X-ray microanalysis. *Ultramicroscopy* 65:187–98
56. Watanabe M, Williams DB. 1999. *Microscopy and Microanalysis* 5:88 (Suppl. 2)
57. Cliff G, Lorimer G. 1975. Quantitative-analysis of thin specimens. *J. Microsc.* 103:203–7
58. Hofer F, Grogger W, Kothleitner G, Warbichler P. 1997. Quantitative analysis of EFTEM elemental distribution images. *Ultramicroscopy* 67:83–103
59. Crozier P. 1995. Quantitative elemental mapping of materials by energy-filtered imaging. *Ultramicroscopy* 58:157–74
60. Craven A, Gibson J, Howie A, Spalding D. 1978. Study of single-electron excitations by electron-microscopy. 1. Image-contrast from delocalized excitations. *Philos. Mag. A* 38:519–27
61. Cundy S, Metherel A, Whelan M. 1967. Contrast preserved by elastic and quasi-elastic scattering of fast electrons near Bragg beams. *Philos. Mag.* 15:623–30
62. Cundy S, Howie A, Valdrè U. 1969. Preservation of electron microscope image contrast after inelastic scattering. *Philos. Mag.* 20:147–63
63. Watanabe H. 1964. Energy selecting microscope. *Jpn. J. Appl. Phys.* 3:480–85
64. Kuwabara S, Uefuji T. 1975. Variation of electron-microscopic thickness fringes of aluminium single-crystals with energy-loss. *J. Phys. Soc. Jpn.* 38: 1090–97
65. Castaing R, Henoc P, Henry L, Natta M. 1967. Degree of coherence of electron scattering by electron-phonon interaction. *C. R. Acad. Sci. B* 265:1293–96
66. Deleted in proof
67. Reimer L, Fromm I, Rennekamp R. 1988. Operation modes of electron spectroscopic imaging and electron energy-loss spectroscopy in a transmission electron microscope. *Ultramicroscopy* 24:339–54
68. Hofer F, Warbichler P. 1996. Improved imaging of secondary phases in solids by energy-filtering TEM. *Ultramicroscopy* 63:21–25
69. Howie A. 1963. Inelastic scattering of electrons by crystals. 1. Theory of small-angle inelastic scattering. *Proc. R. Soc. London Ser. A* 271:268–87
70. Navidi-Kasmai T, Kohl H. 2000. Computation of contrasts in atomic resolution electron spectroscopic images of planar defects in crystalline specimens. *Ultramicroscopy* 81:223–33
71. Freitag B, Mader W. 1999. Element specific imaging with high lateral resolution: an experimental study on layer structures. *J. Microsc.* 194:42–57
72. Krivanek OL, Gubbens AJ, Kundmann MK, Carpenter GC. 1993. *Elemental mapping with an energy-selecting imaging filter*. Presented at 51st EMSA Meet., San Francisco
73. Johnson D. 1979. Energy loss spectrometry for biological research. In *Introduction to Analytical Electron Microscopy*, ed. J Hren, J Goldstein, D Joy, pp. 245–58. New York: Plenum
74. Moore KT, Howe JM, Elbert DC. 1999.

Analysis of diffraction contrast as a function of energy loss in energy-filtered transmission electron microscope imaging. *Ultramicroscopy* 80:203–19

75. Krivanek O, Gubbens A, Dellby N. 1991. Developments in EELS instrumentation for spectroscopy and imaging. *Microsc. Microanal. Microstruct.* 2:315–32
76. Jeanguillaume C, Colliex C. 1989. Spectrum-image: The next step in EELS digital acquisition and processing. *Ultramicroscopy* 28:252–57
77. Hunt J, Williams D. 1991. Electron energy-loss spectrum-imaging. *Ultramicroscopy* 38:47–73
78. Botton G, L'Esperance G. 1994. Development, quantitative performance and applications of a parallel electron energy-loss spectrum imaging system. *J. Microsc.* 173:9–25
79. Bouchet D, Colliex C, Flora P, Krivanek O, Mory C, Tencé M. 1990. Analytical electron-microscopy at the atomic level with parallel electron-energy loss spectroscopy. *Microsc. Microanal. Microstruct.* 1:443–54
80. Jeanguillaume C, Trebbia P, Colliex C. 1978. About use of electron energy-loss spectroscopy for chemical mapping of thin foils with spatial-resolution. *Ultramicroscopy* 3:237–42
81. Lavergne J, Martin J, Belin M. 1992. Interactive electron-energy-loss elemental mapping by the imaging-spectrum method. *Microsc. Microanal. Microstruct.* 3:517–28
82. Lavergne J, Foa C, Bongrand P, Seux D, Martin J. 1994. Application of recording and processing of energy-filtered image sequences for the elemental mapping of biological specimens—Imaging-spectrum. *J. Microsc.* 174:195–206
83. Martin J, Lavergne J, Vacher B, Inoue K. 1995. Interactive image-spectrum EELS—Application to elemental mapping of lubricant colloids. *Microsc. Microanal. Microstruct.* 6:53–63
84. Mayer J, Plitzko J. 1996. Mapping of ELNES on a nanometre scale by electron spectroscopic imaging. *J. Microsc.* 183:2–8
85. Mayer J, Eigenthaler U, Plitzko J, Dettenwanger F. 1997. Quantitative analysis of electron spectroscopic imaging series. *Micron* 28:361–70
86. Plitzko JM, Mayer J. 1999. Quantitative thin film analysis by energy filtering transmission electron microscopy. *Ultramicroscopy* 78:207–19
87. Hofer F, Kothleitner G. 1993. Quantitative microanalysis using electron-energy-loss spectrometry. 1. Li and Be in oxides. *Microsc. Microanal. Microstruct.* 4:539–60
88. Egerton R. 1974. The electron energy loss spectrum and band structure of diamond. *Philos. Mag.* 30:739–49
89. Thomas PJ, Midgley PA. 2001. Image-spectroscopy—I. The advantages of increased spectral information for compositional EFTEM analysis. *Ultramicroscopy* 88:179–94
90. Reimer L, Fromm I, Hirsch P, Plate U, Rennekamp R. 1992. Combination of EELS modes and electron spectroscopic imaging and diffraction in an energy-filtering electron-microscope. *Ultramicroscopy* 46:335–47
91. Kimoto K, Sekiguchi T, Aoyama T. 1997. Chemical shift mapping of Si L and K edges using spatially resolved EELS and energy filtering TEM. *J. Electron Microsc.* 46:369–74
92. Bentley J. 1997. *Interfacial segregation studied with modern AEM techniques*. Presented at Microscopy and Microanalysis, Cleveland, OH
93. Flaitz PL. 1999. *Characterization of a TiN/Ti/$CoSi_2$ interfacial reaction layer by spectrum line imaging*. Presented at Electron Microscopy and Analysis, Sheffield. pp. 605–8. Bristol, UK: Inst. Phys. Conf. Ser. 161
94. Walther T, Mader W. 1999. *Application of spatially resolved electron energy-loss spectroscopy to the quantitative*

analysis of semiconducting layer structures. Presented at MSM-11, Oxford. pp. 121–18. Bristol, UK: Inst. Phys. Conf. Ser. 164

95. Sekiguchi T, Kimoto K, Aoyama T, Mitsui Y. 1998. Nitrogen distribution and chemical bonding state analyses in oxynitride film by spatially resolved electron energy loss spectroscopy (EELS). *Jpn. J. Appl. Phys. Lett.* 37: L694–96
96. Walther T. 2003. Electron energy-loss spectroscopic profiling of thin film structures: 0.39 nm line resolution and 0.04 eV precision measurement of near-edge structure shifts at interfaces. *Ultramicroscopy* 96:401–11
97. Williams DB, Carter B. 1996. *Transmission Electron Microscopy*. New York: Plenum
98. Egerton R. 1993. Oscillator-strength parameterization of inner-shell cross sections. *Ultramicroscopy* 50:13–28
99. Hofer F. 1994. In *Energy-Filtering Transmission Electron Microscopy*, ed. L Reimer, pp. 225–68. Berlin: Springer
100. Knippelmeyer R, Wahlbring P, Kohl H. 1997. Relativistic ionisation cross sections for use in microanalysis. *Ultramicroscopy* 68:25–41
101. Kambe K, Lehmpfuhl G, Fujimoto F. 1974. Interpretation of electron channeling by the dynamical theory of electron diffraction. *Z. Naturforsch.* 29a:1034–44
102. Pennycook S, Jesson D. 1990. High-resolution incoherent imaging of crystals. *Phys. Rev. Lett.* 64:938–41
103. Pennycook SJ, Jesson DE. 1991. High-resolution Z-contrast imaging of crystals. *Ultramicroscopy* 37:14–38
104. Lupini AR, Pennycook S. 2003. Localization in elastic and inelastic scattering. *Ultramicroscopy* 96:313–22
105. Plamann T, Hÿtch MJ. 1999. Tests on the validity of the atomic column approximation for STEM probe propagation. *Ultramicroscopy* 78:153–61
106. Möbus G, Nufer S. 2003. Nanobeam propagation and imaging in a FEG-TEM/STEM. *Ultramicroscopy* 96:285–98
107. Dwyer C, Etheridge J. 2003. Scattering of Å-scale electron probes in silicon. *Ultramicroscopy* 96:343–60
108. Doig P, Flewitt PEJ. 1978. The influence of temper embrittlement on the stress corrosion susceptibility of Fe-3 wt.% Ni alloys. *Acta Metall.* 26:1283–91
109. Michael J, Williams D, Klein C, Ayer R. 1990. The measurement and calculation of the X-ray spatial resolution obtained in the analytical electron microscope. *J. Microsc.* 160:41–53
110. Doig P, Londsdale D, Flewitt P. 1980. The spatial resolution of X-ray microanalysis in the scanning transmission electron microscope. *Philos. Mag. A* 41: 761–75
111. Reed S. 1982. The single-scattering model and spatial-resolution in X-ray-analysis of thin foils. *Ultramicroscopy* 7:405–9
112. Alber U, Müllejans H, Rühle M. 1997. Improved quantification of grain boundary segregation by EDS in a dedicated STEM. *Ultramicroscopy* 69:105–16
113. Maslen V, Rossouw C. 1983. The inelastic scattering matrix element and its application to electron energy loss spectroscopy. *Philos. Mag.* 47:119–30
114. Rafferty B, Pennycook SJ. 1999. Towards atomic column-by-column spectroscopy. *Ultramicroscopy* 78:141–51
115. Bourdillon A, Self P, Stobbs W. 1981. Crystallographic orientation effects in energy dispersive X-ray analysis. *Philos. Mag. A* 44:1335–50
116. Pennycook S, Narayan J. 1985. Atomic location by axial-electron-channeling analysis. *Phys. Rev. Lett.* 54:1543–46
117. Pennycook SJ. 1988. Delocalization corrections for electron channeling analysis. *Ultramicroscopy* 26:239–48

118. Muller DA, Silcox J. 1995. Delocalization in inelastic scattering. *Ultramicroscopy* 59:195–213
119. Müller H, Rose H. 2003. Electron scattering. In *High-Resolution Imaging and Spectrometry of Materials*, ed. F Ernst, M Rühle, pp. 9–68. Berlin: Springer
120. van Benthem K, French R, Sigle W, Elsässer C, Rühle M. 2001. Valence electron energy loss study of Fe-doped $SrTiO_3$ and a $\Sigma 13$ boundary: electronic structure and dispersion forces. *Ultramicroscopy* 86:303–18
121. Bruley J. 1992. Detection of nitrogen at (100) platelets in a type IAA/B diamond. *Philos. Mag. Lett.* 66:47–56
122. Müllejans H, Bruley J. 1994. Improvements in detection sensitivity by spatial difference electron energy-loss spectroscopy at interfaces in ceramics. *Ultramicroscopy* 53:351–60
123. Nufer S. 2001. *Ortsaufgelöste analytische Elektronenmikroskopie an Korngrenzen in alpha-Al_2O_3*. PhD thesis. Univ. Stuttgart. 161 pp.
124. Scheu C. 2002. Electron energy-loss near-edge structure studies at the atomic level: reliability of the spatial difference technique. *J. Microsc.* 207:52–57
125. Gao M, Scheu C, Tchernychova E, Rühle M. 2003. Successful application of the spatial difference technique to electron energy-loss spectroscopy studies of Mo/$SrTiO_3$ interfaces. *J. Microsc.* 210:94–101
126. Muller DA. 1999. Why changes in bond lengths and cohesion lead to core-level shifts in metals, and consequences for the spatial difference method. *Ultramicroscopy* 78:163–74
127. Trebbia P, Bonnet N. 1990. EELS elemental mapping with unconventional methods I. Theoretical basis: image analysis with multivariate statistics and entropy concepts. *Ultramicroscopy* 34:165–78
128. Bonnet N, Simova E, Thomas X. 1991. Application of multivariate statistical-analysis to time-dependent spectroscopy. *Microsc. Microanal. Microstruct.* 2:129–42
128a. Kotula PG, Keenan MR, Michael JR. 2003. Automated analysis of SEM X-ray spectral images: a powerful new microanalysis tool. *Microsc. Microanal.* 9:1–17
129. Titchmarsh J, Dumbill S. 1996. Multivariate statistical analysis of FEG-STEM EDX spectra. *J. Microsc.* 184: 195–207
130. Titchmarsh J, Dumbill S. 1997. Multivariate statistical analysis of STEM-EDX data from radiation-induced sensitization in stainless steel. *J. Microsc.* 188:224–36
131. Titchmarsh JM. 1999. Detection of electron energy-loss edge shifts and fine structure variations at grain boundaries and interfaces. *Ultramicroscopy* 78:241–50
132. Gatts C, Duscher G, Müllejans H, Rühle M. 1995. Analyzing line scan EELS data with neural pattern recognition. *Ultramicroscopy* 59:229–39
133. Krivanek O, Kundmann M, Kimoto K. 1995. Spatial resolution in EFTEM elemental maps. *J. Microsc.* 180:277–87
134. Howie A. 1979. Image-contrast and localized signal selection techniques. *J. Microsc.* 117:11–23
135. Humphreys C, Whelan M. 1969. Inelastic scattering of fast electrons by crystals I. Single electron excitations. *Philos. Mag.* 20:165–72
136. Craven A, Colliex C. 1977. High-resolution energy filtered images in STEM. *J. Microsc. Spectrosc. Electron.* 2:511–22
137. Endoh H, Hashimoto H, Makita Y. 1994. Theoretical and observed electron microscope images of impurity atoms in thin crystals formed by L-shell ionization electrons. *Ultramicroscopy* 56:108–20
138. Wang ZL, Shapiro AJ. 1995. Energy-filtering and composition-sensitive

imaging in surface and interface studies using HREM. *Ultramicroscopy* 60: 115–35

139. Wang Z. 1997. Lattice imaging using plasmon energy-loss electrons in an energy-filtered transmission electron microscope. *Ultramicroscopy* 67:105–11
140. Krivanek O, Gubbens A, Dellby N, Meyer C. 1992. Design and 1st applications of a post-column imaging filter. *Microsc. Microanal.* 3:187–99
141. Stallknecht P, Kohl H. 1996. Computation and interpretation of contrast in crystal lattice images formed by inelastically scattered electrons in a transmission electron microscope. *Ultramicroscopy* 66:261–75
142. Kimoto K, Matsui Y. 2001. Fourier images feature of lattice fringes formed by low-loss electrons as observed using spatially-resolved EELS technique. *J. Electron Microsc.* 50:377–82
143. Kimoto K, Matsui Y. 2003. Experimental investigation of phase contrast formed by inelastically scattered electrons. *Ultramicroscopy* 96:335–42
144. Rose A. 1948. The sensitivity performance of the human eye on an absolute scale. *J. Opt. Soc. Am.* 38:196–208
145. Watanabe M, Williams DB. 1999. Atomic-level detection by X-ray microanalysis in the analytical electron microscope. *Ultramicroscopy* 78:89–101
146. Berger A, Kohl H. 1993. Optimum imaging parameters for elemental mapping in an energy filtering transmission electron-microscope. *Optik* 92:175–93
147. Overwijk M, Reefman D. 2000. Maximum-entropy deconvolution applied to electron energy-loss spectroscopy. *Micron* 31:325–31
148. Mory C, Colliex C. 1989. Elemental analysis near the single-atom detection level by processing sequences of energy-filtered images. *Ultramicroscopy* 28:339–46
149. Krivanek O, Mory C, Tencé M, Colliex C. 1991. EELS quantification near the single-atom detection level. *Microsc. Microanal. Microstruct.* 2:257–67
150. Suenaga K, Tencé M, Mory C, Colliex C, Kato H, et al. 2000. Element-selective single atom imaging. *Science* 290:2280–82
151. Leapman R. 2003. Detecting single atoms of calcium and iron in biological structures by electron energy-loss spectrum-imaging. *J. Microsc.* 210:5–15
152. Feng J, Ho R, Shao Z, Somlyo A. 1999. Parallel electron energy-loss spectroscopy free from gain variation. *Ultramicroscopy* 76:221–31
153. Menon N, Krivanek O. 2002. Synthesis of electron energy loss spectra for the quantification of detection limits. *Microsc. Microanal.* 8:203–15
154. Berger A, Mayer J, Kohl H. 1994. Detection limits in elemental distribution images produced by energy-filtering TEM—case-study of grain-boundaries in Si_3N_4. *Ultramicroscopy* 55:101–12
155. Kohl H, Berger A. 1995. The resolution limit for elemental mapping in energy-filtering transmission electron microscopy. *Ultramicroscopy* 59:191–94
156. Kothleitner G, Hofer F. 1998. Optimization of the signal to noise ratio in EFTEM elemental maps with regard to different ionization edge types. *Micron* 29:349–57
157. Terauchi M, Kuzuo R, Satoh F, Tanaka M, Tsuno K, Ohyama J. 1991. Performance of a new high-resolution electron-energy-loss spectroscopy microscope. *Microsc. Microanal. Microstruct.* 2:351–58
158. Fink J. 1989. Recent developments in energy-loss spectroscopy. *Adv. Electron. Electron Phys.* 75:121–232
159. Batson P. 1999. Advanced spatially resolved EELS in the STEM. *Ultramicroscopy* 78:33–42
160. Mitterbauer C, Kothleitner G, Grogger

W, Zandbergen H, Freitag B, et al. 2003. Electron energy-loss near-edge structures of 3d transition metal oxides recorded at high-energy resolution. *Ultramicroscopy* 96:469–80

161. Lazar S, Botton G, Wu M-Y, Tichelaar F, Zandbergen H. 2003. Materials science applications of HREELS in near edge structure analysis and low-energy loss spectroscopy. *Ultramicroscopy* 96:535–46
162. Brydson R, Scott A, Brown A. 2003. Some thoughts on source monochromation and the implications for electron energy loss spectroscopy. *Z. Metall.* 94:277–81
163. Gloter A, Douiri A, Tencé M, Colliex C. 2002. Improving energy resolution of EELS spectra: an alternative to the monochromator solution. *Ultramicroscopy* 96:385–400
164. Overwijk M, Reefman D, Batson P. 1998. *Maximum entropy deconvolution applied to EELS*. Presented 14th Int. Congress on Electron Microscopy, Cancun, Mexico
165. Yan J, Chen F, Kai J. 2002. Mapping of sp^2/sp^3 in DLC thin film by signal processed ESI series energy-loss image. *J. Electron Microsc.* 51:391–400
166. Haking A, Troester H, Richter K, Crucifix C, Spring H, Trendelenburg MF. 1999. An approach to an objective background subtraction for elemental mapping with core-edges down to 50 eV: description, evaluation and application. *Ultramicroscopy* 80:163–82
167. Egerton R, Malac M. 2002. Improved background-fitting algorithms for ionization edges in electron energy-loss spectra. *Ultramicroscopy* 92:47–56
168. Chan H, Williams D. 1985. Quantitative-analysis of lithium in Al-Li alloys by ionization-energy loss spectroscopy. *Philos. Mag. B* 52:1019–32
169. Leapman RD, Hunt JA, Buchanan RA, Andrews SB. 1993. Measurement of low calcium concentrations in cryosectioned cells by parallel-EELS mapping. *Ultramicroscopy* 49:225–34
170. Tencé M, Quartuccio M, Colliex C. 1995. PEELS compositional profiling and mapping at nanometer spatial resolution. *Ultramicroscopy* 58:42–54
171. Shuman H, Somlyo A. 1987. Electron energy loss analysis of near-trace-element concentrations of calcium. *Ultramicroscopy* 21:23–32
172. Leapman R, Hunt J. 1991. Comparison of detection limits for EELS and EDX. *Microsc. Microanal. Microstruct.* 2:231–44
173. Verbeeck J, Van Aert S. 2004. Model based quantification of EELS spectra. *Ultramicroscopy* 101:207–24
174. Chapman J, Steele J, Paterson J, Titchmarsh J. 1985. *The separation of characteristic signals from complex EELS spectra*. Presented Electron Microscopy and Analysis, Newcastle-upon-Tyne
175. Kundmann M, Krivanek O. 1991. Automated processing of parallel-detection EELS data. *Microsc. Microanal. Microstruct.* 2:245–56
176. Kothleitner G, Hofer F. 2003. Elemental occurrence maps: a starting point for quantitative EELS spectrum image processing. *Ultramicroscopy* 96:491–508
177. Cazaux J. 1995. Correlations between ionization radiation damage and charging effects in transmission electron microscopy. *Ultramicroscopy* 60:411–25
178. Berger S, Salisbury I, Milne R, Imeson D, Humphreys C. 1987. Electron energy-loss spectroscopy studies of nanometre-scale structures in alumina produced by intense electron-beam irradiation. *Philos. Mag. B* 55:341–58
179. Scheu C, Gao M, van Benthem K, Tsukimoto S, Schmidt S, et al. 2003. Advances in EELS spectroscopy by using new detector and new specimen preparation technologies. *J. Microsc.* 210:16–24
180. Egerton R, Li P, Malac M. 2004.

Radiation damage in the TEM and SEM. *Micron* 35:399–409

181. Paxton A, M vS, McKenzie M, Craven A. 2000. The near-edge structure in energy-loss spectroscopy: many-electron and magnetic effects in transition metal nitrides and carbides. *J. Phys. Condens. Matter* 12:729–50
182. Lie K, Hoier R, Brydson R. 2000. Theoretical site- and symmetry-resolved density of states and experimental EELS near-edge spectra of AlB_2 and TiB_2. *Phys. Rev. B* 61:1786–94
183. Mizoguchi T, Tanaka I, Yoshiya M, Oba F, Ogasawara K, Adachi H. 2000. Core hole effects on theoretical electron-energy-loss near-edge structure and near edge X-ray absorption fine structure of MgO. *Phys. Rev. B* 61:2180–87
184. Rez P, MacLaren J, Saldin D. 1998. Application of the layer Korringa-Kohn-Rostoker method to the calculation of near-edge structure in X-ray-absorption and electron-energy-loss spectroscopy. *Phys. Rev. B* 57:2621–27
185. Muller D, Singh D, Silcox J. 1998. Connections between the electron-energy-loss spectra, the local electronic structure, and the physical properties of a material: a study of nickel aluminum alloys. *Phys. Rev. B* 57:8181–202
186. Brydson R. 1991. Interpretation of near-edge structures in the electron energy-loss spectrum. *EMSA Bull.* 21:2:57–67
187. Rehr JJ, Albers RC. 2000. Theoretical approaches to X-ray absorption fine structure. *Rev. Mod. Phys.* 72:621–54
188. Seah M, Dench W. 1979. Quantitative electron spectroscopy of surfaces: a standard data base for electron inelastic mean free paths in solids. *Surf. Interface Anal.* 1:2–11
189. Pantelides S. 1975. Electronic excitation-energies and soft-X-ray absorption-spectra of alkali-halides. *Phys. Rev. B* 11:2391–411
190. Fujikawa T. 1983. Theory of the X-ray absorption near edge structure (XANES) at a deep $L_{2,3}$ edge studied by the short-range order multiple scattering theory. *J. Phys. Soc. Jpn.* 52:4001–7
191. Durham P, Pendry J, Hodges C. 1982. Calculation of X-ray absorption near-edge structure, XANES. *Computer Phys. Commun.* 25:193–205
192. Vvedensky D, Saldin D, Pendry J. 1986. An update of DLXANES, the calculation of X-ray absorption near-edge structure. *Computer Phys. Commun.* 40:421–40
193. Köstlmeier S, Elsässer C. 1999. Ab initio calculation of near-edge structures in electron-energy-loss spectra for metal-oxide crystals. *Phys. Rev. B* 60:14025–34
194. Tanaka I, Adachi H. 1996. Calculation of core hole excitonic features on Al L_{23}-edge X-ray-absorption spectra of alpha-Al_2O_3. *Phys. Rev. B* 54:4604–8
195. Paxton A, Craven A, Gregg J, McComb D. 2003. Bandstructure approach to near edge structure. *J. Microsc.* 210:35–44
196. Köstlmeier S. 2001. Success and limits of common final-state approximations. *Ultramicroscopy* 86:319–24
197. Elsässer C, Köstlmeier S. 2001. Density-functional modelling of core hole effects in electron energy-loss near-edge spectra. *Ultramicroscopy* 86:325–37
198. Kaiser U, Muller D, Grazul J, Chuvilin A, Kawasaki M. 2002. Direct observation of defect-mediated cluster nucleation. *Nat. Mater.* 1:102–5
199. Muller D, Schorsch T, Moccio S, Baumann F, Evans-Lutterodt K, Timp G. 1999. The electronic structure at the atomic scale of ultrathin gate oxides. *Nature* 399:758–61
200. Erni R, Heinrich H, Kostorz G. 2003. Quantitative characterisation of chemical inhomogeneities in Al-Ag using high-resolution Z-contrast STEM. *Ultramicroscopy* 94:125–33
201. Yamazaki T, Watanabe K, Kikuchi Y, Kawasaki M, Hashimoto I, Shiojiri M. 2000. Two-dimensional distribution of

As atoms doped in a Si crystal by atomic-resolution high-angle annular dark field STEM. *Phys. Rev. B* 61:13833–39

202. Schmitz G, Ewert JC, Hartung F. 1999. Chemical analysis by high-angle hollow cone illumination. *Ultramicroscopy* 77:49–63
203. Nüchter W, Sigle W. 1995. Electron channelling: a method in real-space crystallography and a comparison with the atomic location by channelling-enhanced microanalysis. *Philos. Mag. A* 71:165–86
204. Horita Z, Matsumura S, Baba T. 1995. General formulation for ALCHEMI. *Ultramicroscopy* 58:327–35
205. Oxley MP, Allen LJ. 1999. Impact parameters for ionization by high-energy electrons. *Ultramicroscopy* 80:125–31
206. Rossouw C, Turner P, White T, O'Connor A. 1989. Statistical analysis of electron channelling microanalytical data for the determination of site occupancies of impurities. *Philos. Mag. Lett.* 60:225–32
207. Ourmazd A, Baumann FH, Bode M, Kim Y. 1990. Quantitative chemical lattice imaging: theory and practice. *Ultramicroscopy* 34:237–55
208. Schwander P, Kisielowski C, Seibt M, Baumann F, Kim Y, Ourmazd A. 1993. Mapping projected potential, interfacial roughness, and composition in general crystalline solids by quantitative transmission electron-microscopy. *Phys. Rev. Lett.* 71:4150–53
209. De Jong A, Van Dyck D. 1990. Composition determination from HREM images of substitutional alloys. *Ultramicroscopy* 33:269–79
210. Thoma S, Cerva H. 1991. The influence of non-linear interference processes on the HREM contrast of AlGaAs in ⟨100⟩ projection. *Ultramicroscopy* 35: 77–97
211. Walther T, Gerthsen D, Carius R, Forster A, Urban K. 1993. Correlation between the structural and optical-properties of AlGaAs/GaAs quantum-well structures. *Inst. Phys. Conf. Ser.* 134:449–54
212. Hillebrand R, Werner P, Hofmeister H, Gösele U. 1996. A fuzzy logic approach to image analysis of HREM micrographs of III–V compounds. *Ultramicroscopy* 66:73–88
213. Kara F, Dunin-Borkowski RE, Boothroyd CB, Little JA, Stobbs WM. 1996. Fresnel contrast analysis of composition changes and space charge at grain boundaries in mullite. *Ultramicroscopy* 66:59–71
214. Möbus G, Doole R, Inkson B. 2003. Spectroscopic electron tomography. *Ultramicroscopy* 96:433–51
215. Midgley PA, Weyland M. 2003. 3D electron microscopy in the physical sciences: the development of Z-contrast and EFTEM tomography. *Ultramicroscopy* 96:413–31
216. Wang Z. 1996. Valence electron excitations and plasmon oscillations in thin films, surfaces, interfaces and small particles. *Micron* 27:265–99
217. Dorneich A, French R, Müllejans H, Loughin S, Rühle M. 1998. Quantitative analysis of valence electron energy-loss spectra of aluminium nitride. *J. Microsc.* 191:286–96
218. Müllejans H, French R. 1996. Interband electronic structure of a near-Sigma 11 grain boundary in alpha-alumina determined by spatially resolved valence electron energy-loss spectroscopy. *J. Phys. D* 29:1751–60
219. French R, Müllejans H, Jones D. 1998. Optical properties of aluminum oxide: Determined from vacuum ultraviolet and electron energy-loss spectroscopies. *J. Am. Ceram. Soc.* 81:2549–57
220. French R, Müllejans H, Jones D, Duscher G, Cannon R, Rühle M. 1998. Dispersion forces and Hamaker constants for intergranular films in silicon nitride from spatially resolved-valence electron energy loss spectrum imaging. *Acta Mater.* 46:2271–87

221. Ryen L, Wang X, Helmersson U, Olsson E. 1999. Determination of the complex dielectric function of epitaxial $SrTiO_3$ films using transmission electron energy-loss spectroscopy. *J. Appl. Phys.* 85:2828–34
222. Rafferty B, Brown L. 1998. Direct and indirect transitions in the region of the band gap using electron-energy-loss spectroscopy. *Phys. Rev. B* 58:10326–37
223. van Benthem K, Elsässer C, French R. 2001. Bulk electronic structure of $SrTiO_3$: experiment and theory. *J. Appl. Phys.* 90:6156–64
224. Raether H. 1988. *Excitation of Plasmons and Interband Transitions by Electrons*. Berlin/Heidelberg: Springer
225. von Festenberg C. 1969. Energieverlustmessungen an III/IV-Verbindungen. *Z. Phys.* 227:453–81
226. Ferrell T, Echenique P. 1985. Generation of surface excitations on dielectric spheres by an external electron-beam. *Phys. Rev. Lett.* 55:1526–29
227. Ritchie R. 1957. Plasma losses by fast electrons in thin films. *Phys. Rev.* 106:874–81
228. Otto A. 1965. Plasmaschwingungen gebundener Elektronen: Der charakteristische Energieverlust von 3,6 eV in dünnen Silberfolien. *Z. Phys.* 185:232–62
229. Economou E. 1969. Surface plasmons in thin films. *Phys. Rev.* 182:539–54
230. Howie A. 1983. Surface reactions and excitations. *Ultramicroscopy* 11:141–48
231. Garcia-Molina R, Gras-Marti A, Howie A, Ritchie R. 1985. Retardation effects in the interaction of charged particle beams with bounded condensed media. *J. Phys. C* 18:5335–45
232. Howie A, Milne R. 1985. Excitations at interfaces and small particles. *Ultramicroscopy* 18:427–34
233. Howie A, Milne R. 1984. Electron energy loss spectra and reflection images from surfaces. *J. Microsc.* 136:279–85
234. Bolton J, Chen M. 1995. Electron energy loss in multilayered slabs. *Ultramicroscopy* 60:247–63
235. Chase JB, Kliewer KL. 1970. Electron energy loss due to surface modes in a thin ionic crystal film. *Phys. Rev. B* 2:4389–400
236. Batson P. 1982. Surface-plasmon coupling in clusters of small spheres. *Phys. Rev. Lett.* 49:936–40
237. Ouyang F, Isaacson M. 1989. Accurate modeling of particle substrate coupling surface-plasmon exctation in EELS. *Ultramicroscopy* 31:345–50
238. Ouyang F, Isaacson M. 1989. Surface plasmon excitation of objects with arbitrary shape and dielectric constant. *Philos. Mag. B* 60:481–92
239. Echenique P, Howie A, Wheatley D. 1987. Excitation of dielectric spheres by external electron beams. *Philos. Mag.* 56:335–49
240. Ugarte D, Colliex C, Trebbia P. 1992. Surface-plasmon and interface-plasmon modes on small semiconducting spheres. *Phys. Rev. B* 45:4332–43
241. Echenique P, Bausells J, Rivacoba A. 1987. Energy-loss probability in electron-microscopy. *Phys. Rev. B* 35: 1521–24
242. Batson P. 1980. Damping of bulk plasmons in small aluminum spheres. *Solid State Commun.* 34:477–80
243. Chu Y, Warmack R, Ritchie R, Little J, Becker R, Ferrell T. 1984. Contribution of the surface plasmon to energy losses by electrons in a cylindrical channel. *Particle Accelerators* 16:13–17
244. De Zutter D, De Vleeschauwer D. 1986. Radiation from and force acting on a point charge moving through a cylindrical hole in a conducting medium. *J. Appl. Phys.* 59:4146–50
245. Zabala N, Rivacoba A, Echenique P. 1989. Energy-loss of electrons traveling through cylindrical holes. *Surf. Sci.* 209:465–80
246. Walsh C. 1989. Analysis of electron

energy-loss spectra from electron-beam-damaged amorphous AlF_3. *Philos. Mag. A* 59:227–46
247. Dobrzynski L, Maradudin A. 1972. Electrostatic edge modes in a dielectric wedge. *Phys. Rev. B* 6:3810–15
248. Davis LC. 1976. Electrostatic edge modes of a dielectric wedge. *Phys. Rev. B* 14:5523–25
249. Ekardt W. 1985. Size-dependent photoabsorption and photoemission of small metal particles. *Phys. Rev. B* 31:6360–70
250. Mitome M, Yamazaki Y, Takagi H, Nakagiri T. 1992. Size dependence of plasmon energy in Si clusters. *J. Appl. Phys.* 72:812–14
251. Turowski M, Kelly T. 1992. Profiling of the dielectric function across $Al/SiO_2/Si$ heterostructures with electron-energy loss spectroscopy. *Ultramicroscopy* 41: 41–54
252. Moreau P, Brun N, Walsh C, Colliex C, Howie A. 1997. Relativistic effects in electron-energy-loss-spectroscopy observations of the Si/SiO_2 interface plasmon peak. *Phys. Rev. B* 56:6774–81
253. van Benthem K, Tan G, Denoyer L, French R, Rühle M. 2004. Local optical properties, electron densities and London dispersion energies of atomically structured grain boundaries. *Phys. Rev. Lett.* 93:227201/1–4
254. Browning N, Pennycook S. 1996. Direct experimental determination of the atomic structure at internal interfaces. *J. Phys. D* 29:1779–98
255. Lo S, Kai J, Chen F, Chang L, Chen L, et al. 2002. Four-dimensional dielectric property image obtained from electron spectroscopic imaging series. *J. Electron Microsc.* 50:497–507
256. Rafferty B, Pennycook S, Brown L. 2000. Zero loss peak deconvolution for bandgap EEL spectra. *J. Electron Microsc.* 49:517–24
257. Reed BW, Sarikaya M. 2002. Background subtraction for low-loss transmission electron energy-loss spectroscopy. *Ultramicroscopy* 93:25–37
258. Reed B, Chen J, MacDonald N, Silcox J, Bertsch G. 1999. Fabrication and STEM/EELS measurements of nanometer-scale silicon tips and filaments. *Phys. Rev. B* 60:5641–52
259. Bangert U, Harvey A, Keyse R. 1997. Assessment of electron energy-loss spectroscopy below 5 eV in semiconductor materials in a VG STEM. *Ultramicroscopy* 68:173–80
260. Fowler R, Nordheim L. 1928. Electronic emission in intense electric fields. *Proc. R. Soc. A* 119:173–81
261. Alexandrou I, Papworth A, Rafferty B, Amaratunga G, Kiely C, Brown L. 2001. Calculation of the electronic structure of carbon films using electron energy loss spectroscopy. *Ultramicroscopy* 90:39–45
262. Fink J. 1992. Transmission electron energy-loss spectroscopy. In *Unoccupied Electronic States*, ed. J Fuggle, JE Inglesfield. Berlin: Springer
263. Knupfer M, Widder K, Sing M, Knauff O, Fink J. 1998. Influence of the core polarization on the dielectric properties of polyvalent metals. *Eur. Phys. J. B* 6:323–28
264. Sigle W, Krämer S, Varshney V, Zern A, Eigenthaler U, Rühle M. 2003. Plasmon energy mapping in energy-filtering transmission electron microscopy. *Ultramicroscopy* 96:565–71
265. Rosenberg R, Love P, Rehn V. 1986. Polarization-dependent C(K) near-edge X-ray-absorption fine structure of graphite. *Phys. Rev. B* 33:4034–37
266. Souche C, Jouffrey B, Nelhiebel M. 1998. Orientation sensitive EELS-analysis of boron nitride nanometric hollow spheres. *Micron* 29:419–24
267. Browning N, Yuan J, Brown L. 1993. Theoretical determination of angularly-integrated energy-loss functions for anisotropic materials. *Philos. Mag. A* 67: 261–71

268. Menon NK, Yuan J. 1998. Quantitative analysis of the effect of probe convergence on electron energy loss spectra of anisotropic materials. *Ultramicroscopy* 74:83–94

269. Daniels H, Brown A, Scott A, Nichells T, Rand B, Brydson R. 2003. Experimental and theoretical evidence for the magic angle in transmission electron energy loss spectroscopy. *Ultramicroscopy* 96:523–34

270. Hébert C, Schattschneider P, Jouffrey B. 2004. *Magic angle: an unsolved mystery*. Presented at 13th European Microscopy Congr., Antwerp

271. Berger S, McKenzie D, Martin P. 1988. EELS analysis of vacuum arc-deposited diamond-like films. *Philos. Mag. Lett.* 57:285–90

272. Pappas D, Saenger K, Bruley J, Krakow W, Cuomo J. 1992. Pulsed laser deposition of diamond-like carbon films. *J. Appl. Phys.* 71:5675–84

273. Davis C, Amaratunga G, Knowles K. 1998. Growth mechanism and cross-sectional structure of tetrahedral amorphous carbon thin films. *Phys. Rev. Lett.* 80:3280–83

274. Alexandrou I, Scheibe H, Kiely C, Papworth A, Amaratunga G, Schultrich B. 1999. Carbon films with an sp^2 network structure. *Phys. Rev. B* 60:10903–7

275. Papworth A, Kiely C, Burden A, Silva S, Amaratunga G. 2000. Electron-energy-loss spectroscopy characterization of the sp^2 bonding fraction within carbon thin films. *Phys. Rev. B* 62:12628–31

276. Ferrari A, Libassi A, Tanner B, Stolojan V, Yuan J, et al. 2000. Density, sp^3 fraction, and cross-sectional structure of amorphous carbon films determined by X-ray reflectivity and electron energy-loss spectroscopy. *Phys. Rev. B* 62:11089–103

277. Serin V, Beche E, Berjoan R, Abidate O, Dorignac D, et al. 1997. *XAES, XPS, EELS and Raman spectroscopy of polycrystalline to amorphous carbon films with various sp^3 to sp^2 bondings*. Electrochem. Soc. Proc. 5th Int. Symp. Diamond Materials, Paris, pp. 126–42

278. Zhang S, Zeng X, Xie H, Hing P. 2000. A phenomenological approach for the I_d/I_g ratio and sp^3 fraction of magnetron sputtered a-C films. *Surf. Coat. Technol.* 123:256–60

279. Muller D, Tzou Y, Raj R, Silcox J. 1993. Mapping sp^2 and sp^3 states of carbon at subnanometer spatial-resolution. *Nature* 366:725–27

280. Sigle W, Zern A, Hahn K, Eigenthaler U, Rühle M. 2001. Advances in energy-filtering transmission electron microscopy. *J. Electron Microsc.* 50: 509–15

281. Zhu Y, Egerton RF, Malac M. 2001. Concentration limits for the measurement of boron by electron energy-loss spectroscopy and electron-spectroscopic imaging. *Ultramicroscopy* 87:135–45

282. Schmid H. 1995. Phase identification in carbon and BN systems by EELS. *Microsc. Microanal. Microstruct.* 6:99–111

283. Moscovici J, Loupias G, Parent P, Tourillon G. 1996. Polarization-dependent boron and nitrogen K NEXAFS of hexagonal BN. *J. Phys. Chem. Solids* 57:1159–61

284. Tanaka I, Araki H, Yoshiya M, Mizoguchi T, Ogasawara K, Adachi H. 1999. First-principles calculations of electron-energy-loss near-edge structure and near-edge X-ray-absorption fine structure of BN polytypes using model clusters. *Phys. Rev. B* 60:4944–51

285. Terauchi M, Tanaka M, Matsumoto T, Saito Y. 1998. Electron energy-loss spectroscopy study of the electronic structure of boron nitride nanotubes. *J. Electron Microsc.* 47:319–24

286. Fischer D, Wentzcovitch R, Carr R, Continenza A, Freeman A. 1991. Graphitic interlayer states: A carbon K near-edge X-ray-absorption fine-structure study. *Phys. Rev. B* 44:1427–29

287. Fink J, Mullerheinzerling T, Pfluger J, Bubenzer A, Koidl P, Crecelius G. 1983. Structure and bonding of hydrocarbon plasma generated carbon-films—an electron-energy loss study. *Solid State Commun.* 47:687–91
288. Reed B, Sarikaya M. 2002. TEM/EELS analysis of heat-treated carbon nanotubes: experimental techniques. *J. Electron Microsc.* 51:S97–105
289. Menon NK, Yuan J. 1999. Towards atomic resolution EELS of anisotropic materials. *Ultramicroscopy* 78:185–205
290. Suenaga K, Sandré E, Colliex C, Pickard C, Kataura H, Iijima S. 2001. Electron energy-loss spectroscopy of electron states in isolated carbon nanostructures. *Phys. Rev. B* 63:165408–14
291. Kuzuo R, Terauchi M, Tanaka M. 1992. Electron energy-loss spectra of carbon nanotubes. *Jpn. J. Appl. Phys. Lett.* 31: L1484–87
292. Ajayan P, Iijima S, Ichihashi T. 1993. Electron-energy-loss spectroscopy of carbon nanometer-size tubes. *Phys. Rev. B* 47:6859–62
293. Bursill L, Stadelmann P, Peng J, Prawer S. 1994. Surface-plasmon observed for carbon nanotubes. *Phys. Rev. B* 49:2882–87
294. Saito. 1998. *Physical Properties of Carbon Nanotubes*. London: Imperial College
295. Mintmire J, White C. 1998. Universal density of states for carbon nanotubes. *Phys. Rev. Lett.* 81:2506–9
296. Pichler T, Knupfer M, Golden M, Fink J, Rinzler A, Smalley R. 1998. Localized and delocalized electronic states in single-wall carbon nanotubes. *Phys. Rev. Lett.* 80:4729–32
297. Reed B, Sarikaya M. 2001. Electronic properties of carbon nanotubes by transmission electron energy-loss spectroscopy. *Phys. Rev. B* 64:195404–13
298. Kociak M, Henrard L, Stephan O, Suenaga K, Colliex C. 2000. Plasmons in layered nanospheres and nanotubes investigated by spatially resolved electron energy-loss spectroscopy. *Phys. Rev. B* 61:13936–44
299. Suenaga K, Willaime F, Loiseau A, Colliex C. 1999. Organisation of carbon and boron nitride layers in mixed nanoparticles and nanotubes synthesised by arc discharge. *Appl. Phys. A* 68:301–8
300. Lucas A, Gensterblum G, Pireaux J, Thiry P, Caudano R, et al. 1992. Elementary excitations of C_{60} from the far infrared to the far vacuum ultraviolet studied by high-resolution electron-energy-loss spectroscopy. *Phys. Rev. B* 45:13694–702
301. Pichler T, Knupfer M, Golden M, Fink J, Cabioc'h T. 2001. Electronic structure and optical properties of concentric-shell fullerenes from electron-energy-loss spectroscopy in transmission. *Phys. Rev. B* 63:155415–19
302. Martin JM, Vacher B, Ponsonnet L, Dupuis V. 1996. Chemical bond mapping of carbon by image-spectrum EELS in the second derivative mode. *Ultramicroscopy* 65:229–38
303. Hitchcock A, Urquhart S, Rightor E. 1992. Inner-shell spectroscopy of benzaldehyde, terephthalaldehyde, ethyl benzoate, terephthaloyl chloride, and phosgene: models for core excitation of poly(ethylene terephthalate). *J. Phys. Chem.* 96:8736–50
304. Varlot K, Martin JM, Quet C, Kihn Y. 1997. Towards sub-nanometer scale EELS analysis of polymers in the TEM. *Ultramicroscopy* 68:123–33
305. Grubb D, Groves G. 1971. Rate of damage of polymer crystals in the electron microscope: dependence on temperature and beam voltage. *Philos. Mag.* 24:815–28
306. Lindner T, Sauer H, Engel W, Kambe K. 1986. Near-edge structure in electron-energy-loss spectra of MgO. *Phys. Rev. B* 33:22–24
307. Bouchet D, Colliex C. 2003. Experimental study of ELNES at grain boundaries

in alumina: intergranular radiation damage effects on Al-L_{23} and O-K edges. *Ultramicroscopy* 96:139–52

308. Hansen P, Brydson R, McComb D. 1992. p-p-like transitions at the silicon $L_{2,3}$-edges of silicates. *Microsc. Microanal. Microstruct.* 3:213–19
309. Nufer S, Gemming T, Elsässer C, Köstlmeier S, Rühle M. 2001. Core hole effect in the ELNES of alpha-Al_2O_3: experiment and theory. *Ultramicroscopy* 86:339–42
310. Batson P. 1995. Conduction band-structure in strained silicon by spatially-resolved electron-energy-loss spectroscopy. *Ultramicroscopy* 59:63–70
311. Batson P. 2000. Near-edge conduction band electronic states in SiGe alloys. *J. Electron Microsc.* 49:267–73
312. Batson P. 2000. Structural and electronic characterization of a dissociated 60° dislocation in GeSi. *Phys. Rev. B* 61:16633–41
313. Duscher G, Buczko R, Pennycook S, Pantelides S. 2001. Core hole effects on energy-loss near-edge structure. *Ultramicroscopy* 86:355–62
314. Pearson D, Fultz B, Ahn C. 1988. Measurements of 3d state occupancy in transition-metals using electron-energy loss spectrometry. *Appl. Phys. Lett.* 53: 1405–7
315. Pearson D, Ahn C, Fultz B. 1993. White lines and d-electron occupancies for the 3d and 4d transition-metals. *Phys. Rev. B* 47:8471–78
316. Pearson D, Ahn C, Fultz B. 1994. Measurements of the 3d occupancy from Cu L(2,3) electron-energy-loss spectra of rapidly quenched CuZr, CuTi, CuPd, CuPt, and CuAu. *Phys. Rev. B* 50:12969–72
317. Leapman RD, Grunes LA, Fejes PL. 1982. Study of the $L_{2,3}$ edges in the 3d transition-metals and their oxides by electron-energy-loss spectroscopy with comparisons to theory. *Phys. Rev. B* 26:614–35
318. Sparrow T, Williams B, Rao C, Thomas J. 1984. L_3/L_2 white-line intensity ratios in the electron energy-loss spectra of 3d transition-metal oxides. *Chem. Phys. Lett.* 108:547–50
319. Waddington WG, Rez P, Grant IP, Humphreys CJ. 1986. White lines in the $L_{2,3}$ electron-energy-loss and X-ray absorption spectra of 3d transition metals. *Phys. Rev. B* 34:1467–73
320. Thole B, van der Laan G. 1988. Branching ratio in X-ray absorption spectroscopy. *Phys. Rev. B* 38:3158–71
321. Pease DM, Fasihuddin A, Daniel M, Budnick JI. 2001. Method of linearizing the 3d L_3/L_2 white line ratio as a function of magnetic moment. *Ultramicroscopy* 88:1–16
322. Murakami Y, Shindo D, Otsuka K, Oikawa T. 1998. Electronic structure changes associated with a martensitic transformation in a $Ti_50Ni_{48}Fe_2$ alloy studied by electron energy-loss spectroscopy. *J. Electron Microsc.* 47:301–9
323. Krivanek OL, Paterson JH. 1990. ELNES of 3d transition-metal oxides: I. Variations across the periodic table. *Ultramicroscopy* 32:313–18
324. Paterson JH, Krivanek OL. 1990. ELNES of 3d transition-metal oxides: II. Variations with oxidation state and crystal structure. *Ultramicroscopy* 32:319–25
325. de Groot F, Grioni M, Fuggle J, Ghijsen J, Sawatzky G, Petersen H. 1989. Oxygen 1s X-ray-absorption edges of transition-metal oxides. *Phys. Rev. B* 40:5715–23
326. Craven AJ. 1995. The electron energy-loss near-edge structure (ELNES) on the N K-edges from the transition metal mononitrides with the rock-salt structure and its comparison with that on the C K-edges from the corresponding transition metal monocarbides. *J. Microsc.* 180:250–62
327. Leapman R, Newbury D. 1993. Trace

elemental analysis at nanometer spatial-resolution by parallel-detection electron-energy-loss spectroscopy. *Anal. Chem.* 65:2409–14

328. Thole B, van der Laan G, Fuggle J, Sawatzky G, Karnatak R, Esteva J. 1985. 3d X-ray-absorption lines and the $3d^9 4f^{n+1}$ multiplets of the lanthanides. *Phys. Rev. B* 32:5107–18
329. Laan GVD, Thole BT, Sawatzky GA, Goedkoop JB, Fuggle JC, et al. 1986. Experimental proof of magnetic X-ray dichroism. *Phys. Rev. B* 34:6529–31
330. Hébert C, Schattschneider P. 2003. A proposal for dichroic experiments in the electron microscope. *Ultramicroscopy* 96:463–68
331. Schattschneider P, Rubino S, Hébert C. 2004. *Observation of circular dichroism in the TEM*. Presented at Microscopy and Microanalysis, Savannah, GA, p. 836–37 (on CD)
332. Yuan J, Menon N. 1997. Magnetic linear dichroism in electron energy loss spectroscopy. *J. Appl. Phys.* 81:5087–89
333. van Aken P, Lauterbach S. 2003. Strong magnetic linear dichroism in Fe $L_{2,3}$ and 0 K electron energy-loss near-edge spectra of antiferromagnetic hematite alpha-Fe_2O_3. *Phys. Chem. Miner.* 30 (8):469–77
334. Murakami Y, Shindo D, Kikuchi M, Zuo J, Spence J. 2002. Resonance effect in ELNES from perovskite-type manganites $BiMnO_3$ and $LaMnO_3$. *J. Electron Microsc.* 51:99–103
335. Borg RJ, Dienes GJ. 1992. Quantum mechanical principles and the covalent bond. In *The Physical Chemistry of Solids*, pp. 179–227. New York: Academic
336. Brydson R, Garvie LAJ, Craven AJ, Sauer H, Hofer F, Cressey G. 1993. $L_{2,3}$ edges of tetrahedrally coordinated d_0 transition-metal oxyanions XO_4N^-. *J. Phys. Condens. Matter* 5:9379–92
337. Laan Gvd, Kirkman IW. 1992. The 2p absorption spectra of 3d transition metal compounds in tetrahedral and octahedral symmetry. *J. Phys. Condens. Matter* 4:4189–204
338. Ogasawara K, Iwata T, Koyama Y, Ishii T, Tanaka I, Adachi H. 2001. Relativistic cluster calculation of ligand-field multiplet effects on cation L-2,L-3 x-ray-absorption edges of $SrTiO_3$, NiO, and CaF_2. *Phys. Rev. B* 64:115413–15
339. van Benthem K. 2002. *Electron Microscopic Investigations of the bonding behaviour of metals on $SrTiO_3$ substrates*. PhD thesis. Univ. Stuttgart. 206 pp.
340. Brydson R, Sauer H, Engel W, Hofer F. 1992. Electron energy-loss near-edge structures at the oxygen K-edges of titanium(IV) oxygen compounds. *J. Phys. Condens. Matter* 4:3429–37
341. de Groot FMF, Faber J, Michiels JJM, Czyzyk MT, Abbate M, Fuggle JC. 1993. Oxygen 1s X-ray absorption of tetravalent titanium oxides: a comparison with single-particle calculations. *Phys. Rev. B* 48:2074–80
342. Tanaka I, Nakajima T, Kawai J, Adachi H, Gu H, Rühle M. 1997. Dopant-modified local chemical bonding at a grain boundary in $SrTiO_3$. *Philos. Mag. Letters* 75:21–27
343. Wallis DJ, Browning ND. 1997. Probing 3-d structural distortions and coordination changes at $SrTiO_3$ grain boundaries using electron energy loss spectroscopy. *J. Am. Ceram. Soc.* 80:781–85
344. Browning ND, Moltaji HO, Buban JP. 1998. Investigation of three-dimensional grain-boundary structures in oxides through multiple-scattering analysis of spatially resolved electron-energy-loss spectra. *Phys. Rev. B* 58:8289–300
345. Lin X, Wang Y, Dravid V, Michalakos P, Kung M. 1993. Valence states and hybridization in vanadium oxide systems investigated by transmission electron-energy-loss spectroscopy. *Phys. Rev. B* 47:3477–81

346. Gloter A, Serin V, Turquat C, Cesari C, Leroux C, Nihoul G. 2001. Vanadium valency and hybridization in V-doped hafnia investigated by electron energy loss spectroscopy. *Eur. Phys. J. B* 22: 179–86
347. Kurata H, Colliex C. 1993. Electron-energy-loss core-edge structures in manganese oxides. *Phys. Rev. B* 48:2102–8
348. Colliex C, Manoubi T, Ortiz C. 1991. Electron-energy-loss-spectroscopy near-edge fine structures in the iron-oxygen system. *Phys. Rev. B* 44:11402–11
349. Kurata H, Hojou K, Uozumi T. 1998. Cluster model calculations for the Fe L_2,L_3-edge fine structure of alpha-Fe_2O_3. *J. Electron Microsc.* 47:293–99
350. Kurata H, Tanaka N. 1991. Iron $L_{2,3}$ white line ratio in nm-sized gamma-iron crystallites embedded in MgO. *Microsc. Microanal. Microstruct.* 2:183–90
351. van Aken P, Liebscher B. 2002. Quantification of ferrous/ferric ratios in minerals: new evaluation schemes of Fe $L_{2,3}$ electron energy-loss near-edge spectra. *Phys. Chem. Miner.* 29:188–200
352. Muller DA SD, Silcox J. 1998. Connections between the electron-energy-loss spectra, the local electronic structure, and the physical properties of a material: a study of nickel aluminum alloys. *Phys. Rev. B* 57:8181–202
353. Potapov P, Kulkova S, Schryvers D. 2003. Study of changes in $L_{3,2}$ EELS ionization edges upon formation of Ni-based intermetallic compounds. *J. Microsc.* 210:102–9
354. Mizoguchi T, Yoshiya M, Li J, Oba F, Tanaka I, Adachi H. 2001. Electron-energy-loss near edge structures of six-fold-coordinated Zn in MgO. *Ultramicroscopy* 86:363–70
355. Radtke G, Bayle-Guillemaud P. 2004. *EELS study of near edge fine structure in Al(x)Ga(1−x)N alloys*. Presented at 13th Eur. Microscopy Congr., Antwerp, Belgium, pp. 239–40
356. Fortner J, Buck E. 1996. The chemistry of the light rare-earth elements as determined by electron energy loss spectroscopy. *Appl. Phys. Lett.* 68:3817–19
357. Buck E, Fortner J. 1997. Detecting low levels of transuranics with electron energy loss spectroscopy. *Ultramicroscopy* 67:69–75
358. Fortner JA, Buck EC, Ellison AJG, Bates JK. 1997. EELS analysis of redox in glasses for plutonium immobilization. *Ultramicroscopy* 67:77–81
359. Docherty F, Craven A, McComb D, Skakle J. 2001. ELNES investigations of the oxygen K-edge in spinels. *Ultramicroscopy* 86:273–88
360. van Benthem K, Kohl H. 2000. Methods for ELNES-quantification: characterization of the degree of inversion of Mg-Al-spinels. *Micron* 31:347–54
361. Köstlmeier S, Elsässer C, Meyer B. 1999. Ab initio analysis of electron energy loss spectra for complex oxides. *Ultramicroscopy* 80:145–51
362. Brydson R. 1996. Multiple scattering theory applied to ELNES of interfaces. *J. Phys. D* 29:1699–708
363. Klie RF, Ito Y, Stemmer S, Browning ND. 2001. Observation of oxygen vacancy ordering and segregation in Perovskite oxides. *Ultramicroscopy* 86: 289–302
364. Nücker N, Fink J, Renker B, Ewert D, Politis C, et al. 1987. Experimental electronic-structure studies of $La_{2-x}Sr_xCuO_4$. *Z. Phys. B* 67:9–14
365. Yarmoff J, Clarke D, Drube W, Karlsson U, Talebibrahimi A, Himpsel F. 1987. Valence electronic-structure of $Y_1Ba_2Cu_3O_7$. *Phys. Rev. B* 36:3967–70
366. Matsuyama H, Takahashi T, Katayamayoshida H, Kashiwakura T, Okabe Y, et al. 1989. Impurity-state-like nature

of fermi-liquid states in $Bi_2Sr_2CaCu_2O_8$ observed by photoemission and X-ray absorption. *Physica C* 160:567–70

367. Himpsel F, Chandrashekhar G, McLean A, Shafer M. 1988. Orientation of the O 2p holes in $Bi_2Sr_2Ca_1Cu_2O_8$. *Phys. Rev. B* 38:11946–48
368. Nücker N, Romberg H, Xi X, Fink J, Gegenheimer B, Zhao Z. 1989. Symmetry of holes in high-Tc superconductors. *Phys. Rev. B* 39:6619–29
369. Kuiper P, Grioni M, Sawatzky GA, Mitzi D, Kapitulnik A, et al. 1989. Symmetry of the oxygen hole states in $Bi_2Sr_2CaCu_2O_8$ investigated by XAS. *Physica C* 157:260–62
370. Imhoff D, Lauren S, Colliex C, Backhaus-Ricoult M. 1999. Determination of the characteristic interfacial electronic states of {111} Cu-MgO interfaces by ELNES. *Eur. Phys. J. AP* 5: 9–18
371. Muller D, Subramanian S, Batson P, Sass S, Silcox J. 1998. Near atomic scale studies of electronic structure at grain boundaries in Ni_3Al. *Phys. Rev. Lett.* 80:4741–44
372. Dehm G, Scheu C, Möbus G, Brydson R, Rühle M. 1997. Synthesis of analytical and high-resolution transmission electron microscopy to determine the interface structure of Cu/Al_2O_3. *Ultramicroscopy* 67:207–17
373. Scheu C, Dehm G, Rühle M, Brydson R. 1998. Electron-energy-loss spectroscopy studies of Cu-alpha-Al_2O_3 interfaces grown by molecular beam epitaxy. *Philos. Mag. A* 78:439–65
374. Scheu C, Stein W, Rühle M. 2000. Electron energy-loss near-edge structure studies of a Cu/(11–20)-Al_2O_3 interface. *Phys. Status Solidi B* 222:199–211
375. Bruley J, Brydson R, Müllejans H, Mayer J, Gutekunst G, et al. 1994. Investigations of the chemistry and bonding at niobium-sapphire interfaces. *J. Mater. Res.* 9:2574–83
376. Scheu C, Dehm G, Müllejans H, Brydson R, Rühle M. 1995. Electron-energy-loss near-edge structure of metal-alumina interfaces. *Microsc. Microanal. Microstruct.* 6:19–31
377. van Benthem K, Scheu C, Sigle W, Rühle M. 2002. Electronic structure investigations of Ni and Cr films on (100)$SrTiO_3$ substrates using electron energy-loss spectroscopy. *Z. Metall.* 93: 362–71
378. Zhang Z, Sigle W, Kurtz W, Rühle M. 2002. Electronic and atomic structure of a dissociated dislocation in $SrTiO_3$. *Phys. Rev. B* 66:214112–17
379. Zhang Z, Sigle W, Rühle M. 2002. Atomic and electronic characterization of the a[100] dislocation core in $SrTiO_3$. *Phys. Rev. B* 66:094108–18
380. Arslan I, Browning N. 2002. Intrinsic electronic structure of threading dislocations in GaN. *Phys. Rev. B* 65:075310–11
381. Xin Y, James E, Arslan I, Sivananthan S, Browning N, et al. 2000. Direct experimental observation of the local electronic structure at threading dislocations in metalorganic vapor phase epitaxy grown wurtzite GaN thin films. *Appl. Phys. Lett.* 76:466–8
382. Nufer S, Marinopoulos A, Gemming T, Elsässer C, Kurtz W, et al. 2001. Quantitative atomic-scale analysis of interface structures: transmission electron microscopy and local density functional theory. *Phys. Rev. Lett.* 86:5066–69
383. Walther T, Daneu N, Recnik A. 2004. A new method to measure small amounts of solute atoms on planar defects and application to inversion domain boundaries in doped zinc oxide. *Interface Sc.* 12:267–75

383a. Watanabe M, Williams DB. 2003. Quantification of elemental segregation to lath and grain boundaries in low-alloy steel by STEM X-ray mapping combined with the ζ-factor method. *Z. Metall.* 94:307–16

384. Kooi B, Wouters O, de Hosson J. 2001. Analysis of Gibbsian segregation at heterophase interfaces using analytical transmission electron microscopy: a novel approach. *Acta Mater.* 50:223–35

385. Browning N, Arslan I, Ito Y, James E, Klie R, et al. 2001. Application of atomic scale STEM techniques to the study of interfaces and defects in materials. *J. Electron Microsc.* 50:205–18

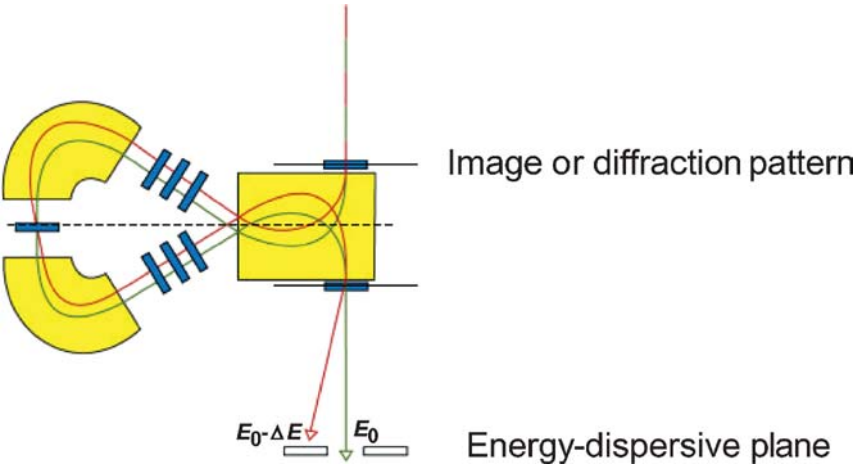

Figure 3 Electron energy filter (MANDOLINE type, Zeiss) which is incorporated within the microscope column. Electrons having suffered specific energy losses can be selected by the energy-selecting slit.

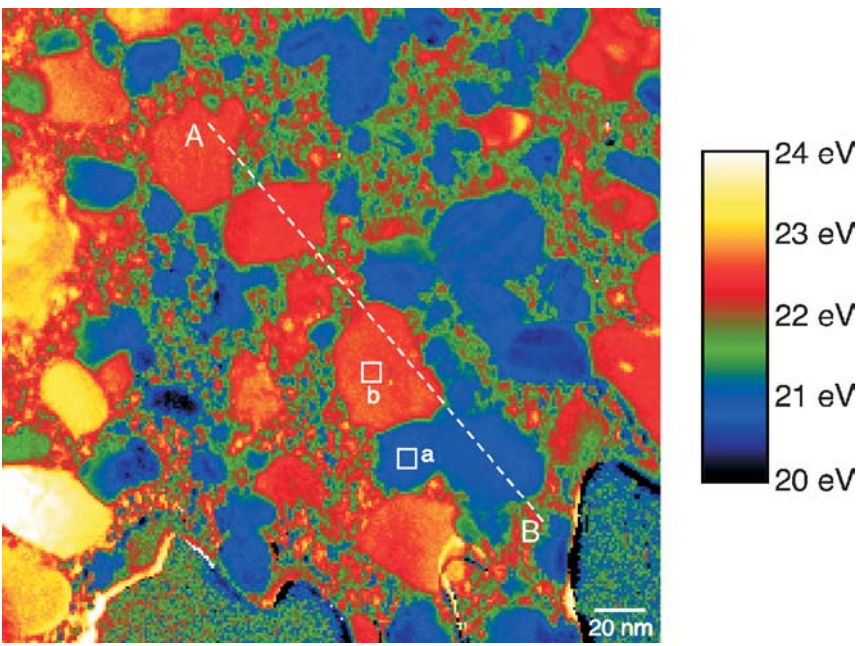

Figure 22 Map of plasmon peak energies in a Si-B-C-N ceramic containing SiC (*blue*) and Si_3N_4 (*orange*) grains. The grains can be easily distinguished owing to their different valence electron densities. Reprinted with permission from Sigle et al. (264).

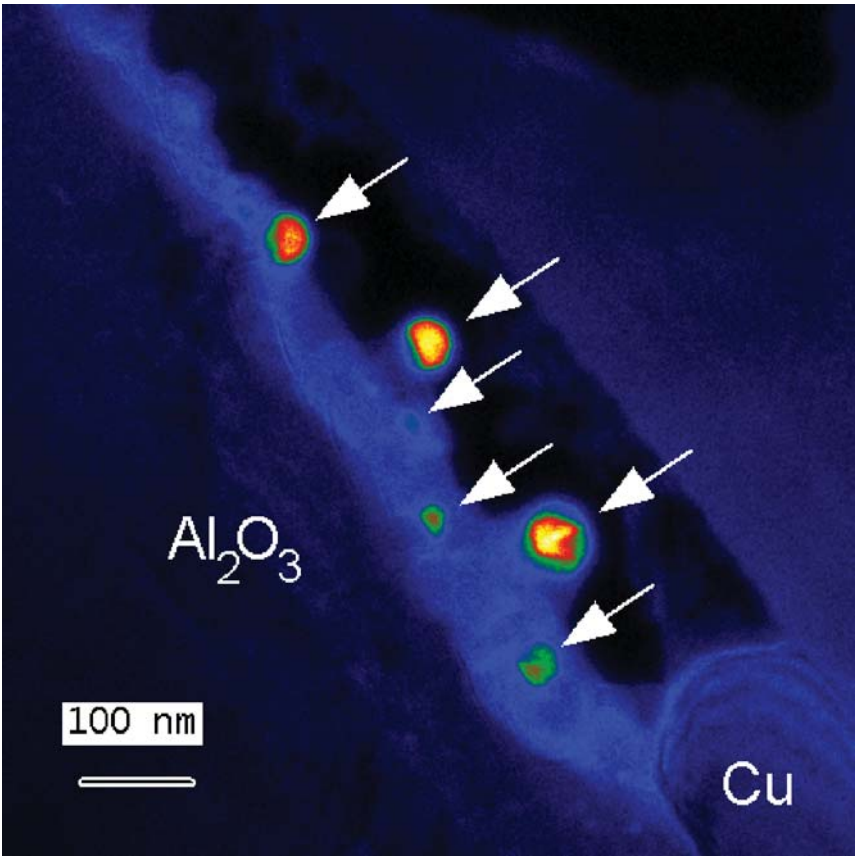

Figure 26 Image obtained from electrons that have excited a plasmon in metallic Al. The metallic particles (*red* and *yellow*) can be easily distinguished from oxidized Al (*blue*).

Annual Review of Materials Research
Volume 35, 2005

CONTENTS

MATERIALS DESIGN AND CHEMISTRY OF ENVIRONMENTALLY ACCEPTABLE CATALYSTS

THE PREPARATION AND CHARACTERIZATION OF HIGHLY EFFICIENT TITANIUM OXIDE–BASED PHOTOFUNCTIONAL MATERIALS, *Masakazu Anpo, Satoru Dohshi, Masaaki Kitano, Yun Hu, Masato Takeuchi, and Masaya Matsuoka* 1

APPLICATION OF EXAFS TO MOLTEN SALTS AND IONIC LIQUID TECHNOLOGY, *Christopher Hardacre* 29

THE PREPARATION OF SKELETAL CATALYSTS, *A.J. Smith and D.L. Trimm* 127

HETEROGENEOUS ASYMMETRIC CATALYSTS: STRATEGIES FOR ACHIEVING HIGH ENANTIOSELECTION, *Graham J. Hutchings* 143

ENGINEERED POROUS CATALYTIC MATERIALS, *Ferdi Schüth* 209

DESIGNING CATALYSTS FOR CLEAN TECHNOLOGY, GREEN CHEMISTRY, AND SUSTAINABLE DEVELOPMENT, *John Meurig Thomas and Robert Raja* 315

POROUS ALUMINOPHOSPHATES: FROM MOLECULAR SIEVES TO DESIGNED ACID CATALYSTS, *H.O. Pastore, S. Coluccia, and L. Marchese* 351

CHEMICAL DESIGN AND IN SITU CHARACTERIZATION OF ACTIVE SURFACES FOR SELECTIVE CATALYSIS, *Mizuki Tada and Yasuhiro Iwasawa* 397

METAL CATALYST DESIGN AND PREPARATION IN CONTROL OF DEACTIVATION, *Michael S. Spencer and Martyn V. Twigg* 427

ELECTRON MICROSCOPY IN THE CATALYSIS OF ALKANE OXIDATION, ENVIRONMENTAL CONTROL, AND ALTERNATIVE ENERGY SOURCES, *Pratibha L. Gai and Jose J. Calvino* 465

CURRENT INTEREST

THE DIFFUSION-MULTIPLE APPROACH TO DESIGNING ALLOYS, *Ji-Cheng (J.-C.) Zhao* 51

SPATIAL ORDER AND DIFFRACTION IN QUASICRYSTALS AND BEYOND, *Denis Gratias, Lionel Bresson, and Marianne Quiquandon* 75

INFLUENCE OF INTERFACE ANISOTROPY ON GRAIN GROWTH AND COARSENING, *Gregory S. Rohrer* 99

THE OXIDATION OF NiAl: WHAT CAN WE LEARN FROM AB INITIO CALCULATIONS? *M.W. Finnis, A.Y. Lozovoi, and A. Alavi* 167

ANALYTICAL TRANSMISSION ELECTRON MICROSCOPY, *Wilfried Sigle* 239

COMPOSITE MATERIALS FOR WIND POWER TURBINE BLADES, *Povl Brøndsted, Hans Lilholt, and Aage Lystrup* 505

MATERIALS CHARACTERIZATION IN THE ABERRATION-CORRECTED SCANNING TRANSMISSION ELECTRON MICROSCOPE, *M. Varela, A.R. Lupini, K. van Benthem, A.Y. Borisevich, M.F. Chisholm, N. Shibata, E. Abe, and S.J. Pennycook* 539

ADHESION AND DE-ADHESION MECHANISMS AT POLYMER/METAL INTERFACES: MECHANISTIC UNDERSTANDING BASED ON IN SITU STUDIES OF BURIED INTERFACES, *G. Grundmeier and M. Stratmann* 571

INDEXES

Subject Index 617

Cumulative Index of Contributing Authors, Volumes 31–35 655

Cumulative Index of Chapter Titles, Volumes 31–35 657

ERRATA

An online log of corrections to *Annual Review of Materials Research* chapters may be found at http://matsci.annualreviews.org/errata.shtml